이학박사 학위논문

광촉매 황화아연 나노구조체와 재사용 가능한 수산화철 분리막의 제조 및 응용

Fabrication and Application of Photocatalytic ZnS Nanostructures and Reusable FeOOH Membranes

2020 년 8 월

서울대학교 대학원

화학부 물리화학 전공

함수호

A ph. D. Dissertation

Fabrication and Application of Photocatalytic ZnS Nanostructures and Reusable FeOOH Membranes

By Sooho Ham

Supervisor: Professor Du-Jeon Jang

Major: Physical Chemistry

Department of Chemistry

Graduate School of Seoul National University

August 2020

Abstract of Dissertation

In this dissertation, enhancing photocatalytic activity of ZnS nanostructures and facile fabrication of reusable FeOOH membranes are mainly discussed. ZnS nanostructures have been synthesized *via* facile hydrothermal method and have been treated with additional hydrothermal reactions and photohydroxylation to enhance the photocatalytic activity of degrading organic molecules. ZnS nanostructures with S vacancies were synthesized by additional hydrothermal treatment of $ZnS(en)_{0.5}$. Also, the surfaces of ZnS nanostructures were hydroxylated *via* photohydroxylation. Gold nanoparticles have also decorated the surfaces of ZnS nanostructures through photodeposition. The S vacancies, surface –OH groups, and gold nanoparticles have enhanced the separation of photoexcited charges, leading to the increase of photocatalytic activity. Furthermore, organic-molecule separation membranes were fabricated based on FeOOH rods and track-etched polycarbonate membranes. Brief overviews of the Chapter 1-5 mentioned in this dissertation are given below.

Chapter 1 reports a general introduction of nanomaterials. Nanomaterials exhibit markedly different properties depending on the size of nanomaterials. The unique properties of nanomaterials are described in Chapter 1. As well as the properties of nanomaterials, the various synthetic methods and applications of nanomaterials are described. Especially, the applications related to water remediation are described in detail.

Chapter 2 presents the photohydroxylation of ZnS nanobelts by H_2O_2 under UV-vis

irradiation. The surfaces of ZnS nanobelts were easily hydroxylated to form Zn-OH bonds *via* the photohydroxylation processes. Under UV-vis light irradiation, H_2O_2 molecules are transformed into reactive hydroxyl radicals (·OH). Furthermore, photo-excited electrons in the conduction bands of ZnS nanobelts react with H_2O_2 to form ·OH. These reactive ·OH react with the surfaces of ZnS nanobelts to generate Zn-OH and defects. The photo-excited electron-hole pairs have been separated by the Zn-OH bonds and defects, enhancing photocatalytic activity of degrading 4-nitrophenol molecules. Overall, through the simple photohydroxylation processes, the photocatalytic activity degrading aqueous organic molecules of ZnS nanobelts were highly enhanced, proving that photohydroxylation methods are useful method to enhance the photocatalytic activities.

Chapter 3 describes the enhancement of photocatalytic activity of ZnS by modulating the concentration of S vacancies. Hollow ZnS nanoplates with controlled amount of S vacancies have been facilely fabricated *via* the hydrothermal treatment of $ZnS(en)_{0.5}$ nanoplates (en = ethylenediamine). The amount of S vacancies and the morphologies of ZnS have been controlled by modulating the hydrolysis time. The layered structure of $ZnS(en)_{0.5}$ nanoplates decomposes to yield discrete ZnS nanoparticles at two end facets with abundant S vacancies. The concentrations of S vacancies were monitored by measuring photoemission spectra at 390 nm. The S vacancies can trap photogenerated electrons to block the recombination of electron-hole pairs, enhancing photocatalytic activity of ZnS nanostructures. The photocatalytic activity of ZnS nanostructures were highly enhanced after hydrolysis, suggesting that hollow nanoplates have great applicability to photocatalysts in waste-water treatment.

Chapter 4 presents the ZnS nanobelts decorated with gold nanoparticles. Gold nanoparticles have decorated the surfaces of ZnS nanobelts *via* photodeposition methods. With photo-excited electrons in ZnS nanobelts, gold precursors are directly reduced on the surfaces of ZnS nanobelts. Because the gold nanoparticles have been fabricated in the absence of any reducing agents or surfactants, charge-separating junctions have been effectively produced. New energy levels of gold nanoparticles effectively separated electron-hole pairs. The separation mechanism of electron-hole pairs were also studied by measuring photoluminescence spectra and decay kinetics. The long-lived excited charges have promoted the generation of reactive radical species, enhancing the photocatalytic degradation efficiencies of organic molecules. Overall, through photodeposition process, charge separation junctions have been formed effectively to increase photocatalytic efficiency, suggesting that the photodeposition of gold is an effective method to increase photocatalytic activities.

Chapter 5 describes the fabrication of FeOOH separation membranes on track-etched polycarbonate membranes. FeOOH rods have been synthesized by the reaction between Fe^{2+} and OH^- ions inside the pores of polycarbonate membranes. The FeOOH particles exhibit high porosity having large surface area and pore volume. As-synthesized FeOOH-polycarbonate membranes have separated the organic dyes (4-nitrophenol, methyl blue) without requiring energies. After the separation, the FeOOH-polycarbonate membranes are cleaned *via* photo-Fenton reactions. *Via* the photo-Fenton reaction, adsorbed organic molecules were degraded easily. Thus, the FeOOH membranes can be reused for several times. Overall, FeOOH-polycarbonate separation membranes can be fabricated via simple

interfacial synthesis, suggesting that FeOOH membranes have great applicability in organic molecule separations.

Keywords: Charge separation, Hybrid nanostructures, Photocatalysts, Semiconductor nanostructures, Separation membranes

Student Number: 2014-22417

Table of Contents

List of Figures and Tables

Figure 3-7 HRTEM images (a, b, and d) and FFT patterns (c and e) of a porous ZE4 nanostructures.

Figure 3-8 HRTEM image (a) and FFT pattern (b) of a porous ZE4 nanostructures. Yellow lines indicate lattice alignments while red circles mark pore regions.

Figure 3-9 EDX elemental profiles (top) scanned along the lines of the STEM images (bottom) of a ZE4 nanostructures.

Figure 3-10 XPS spectra of indicated nanostructures

Figure 3-11 Low-magnification SEM images (left) and EDX elemental profiles (right) scanned inside the square lines of the SEM images of ZE0 (a), ZE2 (b), ZE3 (c), ZE4 (d), and ZE5 (e) nanostructures.

Table 3-2 S/Zn atomic ratios in ZE nanostructures, obtained from XPS spectra in Figure 3-9.

Figure 3-12 Extinction spectra of indicated nanostructures suspended in ethanol.

Figure 3-13 Absorption spectra of RhB solutions in the presence of light without nanocatalysts (a), with commercial ZnS (b), and with nanocatalysts of ZE0 (c), ZE1 (d), ZE2 (e), ZE3 (f), ZE4 (g), ZE5 (h), and ZE6 (i), measured at elapsed times indicated in the units of min.

Figure 3-14 First-order decay profiles (a) and degradation rate constants (b) of RhB *via* ZE nanostructures.

Table 3-3 Photocatalytic rate constants, BET surfaces areas, average pore sizes, and total pore volumes of ZE nanostructures.

Figure 3-15 TEM images of commercial ZnS. Each scale bar represents 500 nm.

Figure 3-16 N_2 adsorption-desorption isotherms (a) and pore-size distributions (b) of indicated ZE nanostructures.

FeOOH/RT-PC membrane (b), bare FeOOH/HT particles (c), and a FeOOH/HT-PC membrane (d).

Figure 5-11 Organic dyes penetration tests for 4NP, MB, MO, and MnB by FeOOH/RT (a) and FeOOH/HT (b) membranes.

Figure 5-12 Separation of 4NP/MB by FeOOH/RT (a) and FeOOH/HT (b) membranes.

Figure 5-13 Absorption spectra of the 4NP (a,c) and MB (b,d) before (black) and after (red) 1 h separation by FeOOH/RT (top) and FeOOH/HT (bottom) membranes.

Figure 5-14 UV-vis absorption spectra of bare FeOOH/RT and FeOOH/HT particles, dispersed in ethanol at a concentration of 0.1 mg/mL.

Figure 5-15 Photocatalytic degradation of 4NP (a) and MB (b) by no catalysts (blue), bare FeOOH/HT particles (green), and bare FeOOH/RT particles (red) dispersed in H_2O_2 under xenon-lamp irradiation.

Figure 5-16 DR spectra of a pristine FeOOH/RT membrane (black), a FeOOH/RT membrane after 4NP/MB separation (red), and a FeOOH/RT membrane after photo-Fenton cleaning (green).

Figure 5-17 Recycling tests for the separation of 4NP (black) and MB (red) by FeOOH/RT (a) and FeOOH/HT (b) membranes.

Figure 5-18 DR spectra of a FeOOH/RT membrane (a) and a FeOOH/HT membrane (b) after 4NP/MB separation (red) and photo-Fenton cleaning (black).

Figure 5-19 TEM images of FeOOH/RT (a,b) and FeOOH/HT (c,d) particles after 5 cycles of photo-Fenton cleaning.

Figure 5-20 FTIR spectra of FeOOH/RT (black) and FeOOH/HT (red) particles after 5 cycles of photo-Fenton cleaning.

Figure 5-21 The absorption spectra of 4NP (a) and MB (b) during adsorption to

FeOOH/RT particles. Times for adsorption are presented inside in the unit of min.

Figure 5-22 Time-dependent q_t of 4NP and MB in the presence of FeOOH/RT particles.

Figure 5-23 Intraparticle diffusion model (a), pseudo-first-order (b), and pseudo-second-order adsorption kinetics of MB by FeOOH/RT particles.

Table 5-1 Kinetic and intra-particle diffusion parameters for the adsorption of MB by FeOOH/RT particles.

Figure 5-24 N_2 adsorption-desorption isotherms (a) and pore-size distribution profiles (b) of FeOOH/RT (black) and FeOOH/HT (red) particles.

Table 5-2 BET surfaces areas, average pore sizes, and total pore volumes of FeOOH/RT and FeOOH/HT particles.

Figure 5-25 Schematics for the interfacial synthesis (A) and the separation and photo-Fenton cleaning (B) of a FeOOH-PC membrane.

Chapter 1. General Introduction

1.1 Properties of nanomaterials

Nanosized and nanostructured materials

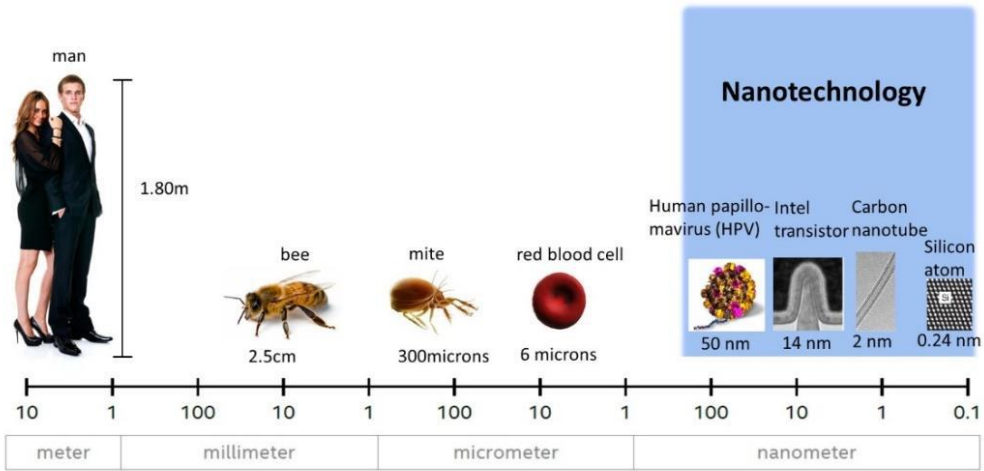

Figure 1-1 Scale of dimensions from meter down to nanometer. Reproduced from Ref. 1.

The nanosized materials (nanomaterials) refer the materials, whose size are in nano (10^{-9}) meter scale.[1] The nanomaterials are composed of various materials like semiconductor, metal, carbon, polymer and etc. Compared to the bulk sized materials nanomaterials present unique physical and optical properties. Furthermore, while the properties of bulk materials hardly depend on the diameter or morphology of the materials, nanomaterials show different electronic or optical properties depending on their size or morphology. Thus, by adjusting the size or morphology of nanomaterials, the synthesis of nanomaterials with desired properties is possible. Because of the unique

properties of nanomaterials, the nanomaterials have been applied to the various fields of energy, environment, and biology. Therefore, the nanomaterials are considered as wonder materials for many researchers. There are typically two main factors that determine the properties of nanomaterials: quantum-confinement effect and surface effect.

Quantum-confinement effect

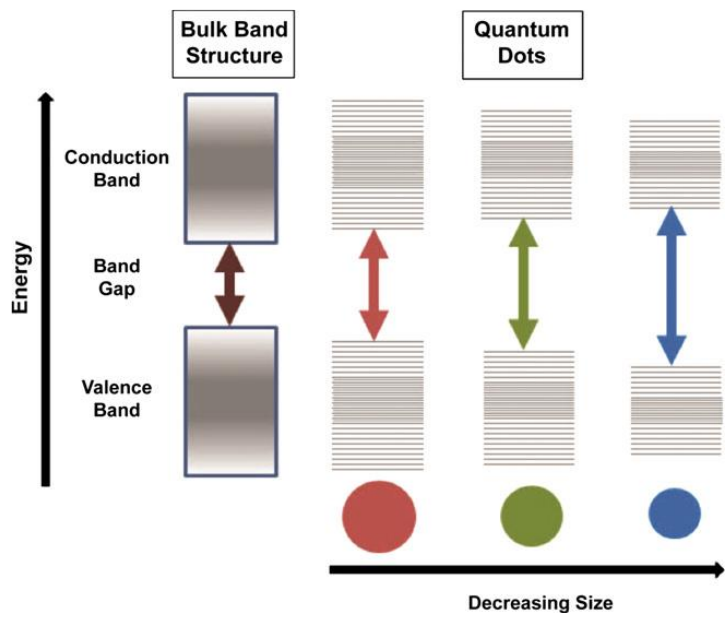

Figure 1-2 The quantum confinement effect on energy levels of semiconductor. Reproduced from Ref 2.

Nanomaterials exhibit different electronic and optical properties compared to bulk materials with same composition. In intermediate size range between molecular and bulk matter, continuous energy band of bulk matter becomes discrete as the orbital overlap

decreases. As the size of nanomaterial decreases, the number of atoms consisting nanomaterials decreases, leading to the decrease of orbital overlap. Because of the decrease of orbital overlap, energy gap between conduction band and valence band increases. Thus, the band-gap energies increases as the size of nanomaterials decreases (Figure 1-2). Also, the energies of conduction band and valence band change; the conduction band level becomes more negative and the valence band level becomes more positive as the size of nanomaterials decreases. The transformation of continuous energy band structures in macroscopic semiconductors to discrete energy structures in nano-sized semiconductors is called as quantum confinement effect. Quantum confinement effect can be observed when a material has similar diameter as the de Broglie wavelength of the electron wave function. As the length of confining quantum well decreases and reach a certain limit of exciton Bohr radius, the energy spectrum becomes discrete, exhibiting different electronic and optical properties along the diameter of materials.

Surface effect

Due to the small diameter of nanomaterials, the number of atoms on the surfaces of materials increases.[3] For the spherical materials with radius of **r**, the surface area of the material shows linear relationship with $\mathbf{r^2}$, while volume of the material has linear relationship with $\mathbf{r^3}$. As a result, the surface-to-volume ratios have linear relationship with **r**. Thus, nanomaterials present high surface-to-volume ratios because of the small diameter of nanomaterials. Typically, nanomaterials with low dimension (1D or 2D)

have higher surface-to-volume ratios than bulk materials. Furthermore, nanomaterials with hierarchical or porous structures show particularly large surface area. With the large surface area of nanomaterials, more atoms are located on the surfaces of nanomaterials. The atoms at the surfaces have relatively smaller coordination number than the atoms inside the nanomaterials. The atoms with low coordination number present low stability and high reactivity, enabling various reactions, which was impossible for bulk materials.

1.2 Fabrication of nanomaterials

With various properties, nanomaterials have played an important role in nanotechnology such as energy, environment, health, medicine, and so on. As mentioned above, nanomaterials have various properties depending on their size and morphology. Therefore, it is very important to develop a method for synthesizing nanomaterials with specific sizes and morphologies. It also needed to synthesize nanomaterials with 1D, 2D, 3D and anisotropic structures (Figure 1-3).[4] Additionally, the synthesis of nanomaterials with junction, hybrid structures and composition is desired.

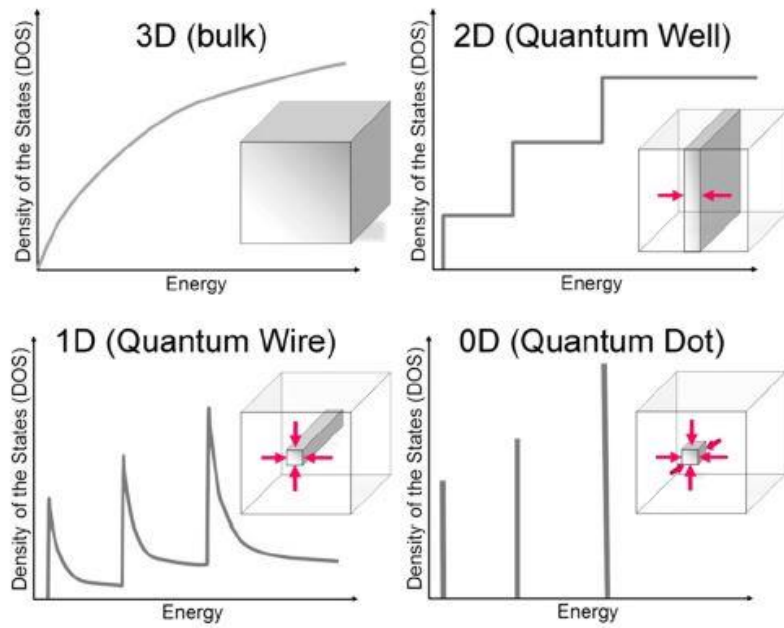

Figure 1-3 Electronic DOS for a bulk 3D crystalline material, a 2D QW, a 1D NW or NT, and a 0D QD. The insets report a cartoon showing the corresponding spatial confinement: confinement directions are defined by arrows. Reproduced from Ref 4.

The synthesis of nanostructures is divided into two steps; nucleation and continuous growth of nucleus or seeds (Figure 1-4).[5] The shapes and sizes of nanomaterials are affected by several factors during the nucleation and growth steps. Initial crystal facets of seeds is critical factor for morphology and crystal structure of nanomaterials because the monomers of nanomaterials aggregates on the seeds following the crystal structures of the seeds. After the seed formation, several parameters determine the final size, morphology, and crystal structure of nanomaterials; capping agents, intrinsic surface energy of specific facets, which determine the thermodynamics and kinetics of growth.[6]

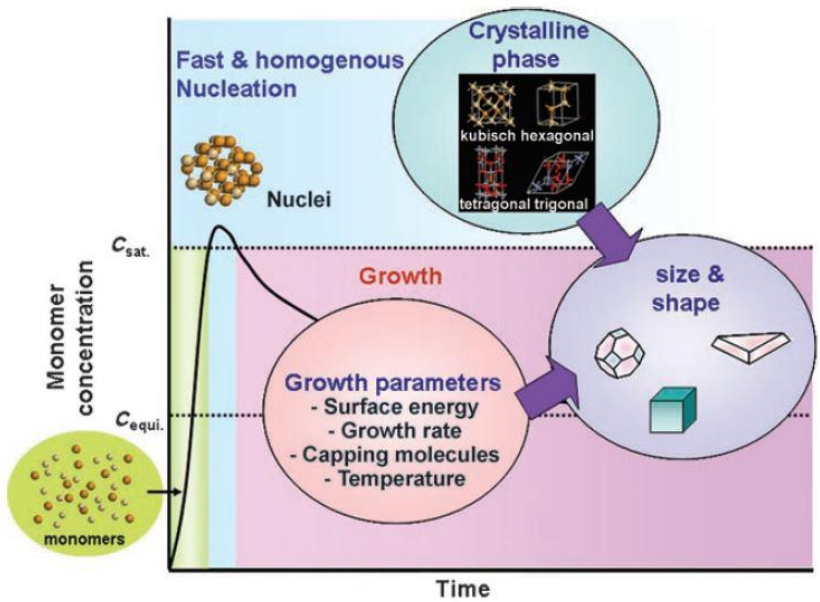

Figure 1-4 Crystal-growth diagram. When the monomer concentration reaches a supersaturation level, seed nucleation occurs and then monomer continuously aggregates onto the seeds, which results in the gradual decrease of monomer concentration. During these nucleation and growth stages, the control of growth parameters and crystalline phase is critical in determining the final size and shape of nanocrystals. C_{sat} = saturation concentration, C_{equi} = equilibrium concentration. Reproduced from Ref. 5.

Hydrothermal/Solvothermal synthesis

Hydrothermal and solvothermal synthesis are techniques of synthesizing nanomaterials in high temperature of aqueous and organic solvents, respectively.[7] Because the reactions proceeds in a closed rector under high temperature, which is higher than the boiling point of reaction solvents, the crystallization occurs at high

pressure and temperature. As the temperature and pressure increase, monomers of nanomaterials aggregates on thermodynamically stable sites of seeds, leading to the formation of high crystalline nanomaterials. By adjusting the reaction temperature or solvent composition, it is possible to synthesize nanomaterials having various structures. While solvothermal methods are usually adopted to synthesize non-oxide nanomaterials, hydrothermal methods are used to synthesized oxide or hydroxide nanomaterials.

Sol-gel

The sol-gel method is one of most preferred synthetic methods of nanomaterials because of its simplicity. In a typical process, "**sol**" (a colloidal) solution is formed in the beginning of synthesis. Then, the **sol** is gradually transformed into "**gel**" (discrete particle or polymer) through condensation or polymerization. Ultrafine particles, nanofilms, and porous membranes can be fabricated through this process.[8] Usually, metal oxides like SiO_2 or TiO_2 are synthesized facilely by the sol-gel methods.

Co-precipitation

The co-precipitation method refers to a reaction mixing two or more water-soluble salts, which react to form water-soluble salts.8 As the sol-gel method, co-precipitation method is widely used to synthesize nanomaterials because of convenience of synthetic steps; nanoparticles can be fabricated by simple mixing of aqueous salts. Usually, metal oxide or hydroxide nanoparticles are synthesized

easily via the co-precipitation methods. For example, iron oxide nanoparticles can be fabricated easily by mixing $FeCl_2$ or $FeCl_3$ solutions with Na_2CO_3 solutions.[9] As the reaction temperature increases, the crystallinity of nanoparticles increases. The sizes or morphologies of nanoparticles can be controlled by the reaction conditions like pH, capping agents, ratio of salts, and reaction temperature.

Photo-mediated synthesis

The nanomaterials can be fabricated by light irradiation. One on the representative methods for synthesizing nanoparticles using light is photodeposition.[10] The photodeposition methods are usually applied to fabricated nanoparticles onto the photo-sensitive materials. When photo-sensitive materials absorbed light, excited electron-hole pairs are generated. The excited electrons can reduce metal ions ($HAuCl_4$, $AgNO_3$, $FeCl_3$, etc.) to form metal nanoparticles. Also, photo-excited holes can oxides metal precursors to form teal oxide nanoparticles. Because the nanoparticles are photodeposited onto the surfaces of photo-sensitive materials, photodeposition methods are usually applied to form heterojunction or hybrid nanostructures.

In addition to the above mentioned synthetic methods, there are various kinds of synthetic methods such as chemical vapor deposition (CVD),[11] sputtering,[12] and so on. The properties of nanomaterials are determined by the composition, size, morphology, crystal structures. Because the size, morphology, crystal structures are differed by the synthetic methods, to fabricate nanomaterials with desired

properties, the nanomaterials must be synthesized through an appropriate synthetic methods.

1.3 Application of nanomaterials

Nanomaterials have been applied to various fields of energy, biology, optics and environment, due to unique optical and electronic properties of nanomaterials.

(1) Electronics: The specific nanoparticles such as quantum dots presented very bright luminescence with high quantum efficiencies. Also, due to the small size of nanoparticles, the size of light emitting device could be reduced. As mentioned above, the optical and electronic properties of nanoparticles depend on the size of nanoparticle. By controlling the sizes of nanoparticles, the luminescence wavelength could be controlled.[13] Like the fields of display, nanoparticles have also been applied to the battery. By using nanoparticles in batteries, the capacitance of batteries are increased, while size and weight are decreased, facilitating the progress of portable electronic devices.[14] It was also possible to manufacture a small-sized optical sensor by using the point that the UV-vis absorption spectra of semiconductor nanoparticles varies depending on the sizes of nanoparticles.[15]

(2) Biology and Medicine: The nanoparticles show specific absorption and emission spectra along the surrounding environment.[16] Using this properties, nanoparticles can detect specific organic molecules. For example, carbon quantum dots with gold nanoparticles have different emission intensities depending on the presence of

surrounding enzymes and H_2O_2.[17] Also, Due to the small size of nanoparticles, nanoparticles can be injected through the blood vessel, delivering medicines or specific molecules to targeted cells.[18] Furthermore, nanoparticles itself can act as imaging probes or medicine to diagnose or cure the diseases.

(3) Energy and Environment: The nanoparticles have been applied to solar cells because of high photo-sensitivity and electric conductivity. Also, due to high surface area and large catalytic sites, nanoparticles have presented high catalytic activity in fuel cells, organic reaction, and water remediation. The detail of water remediation processes by nanoparticles are described in Chapter 1.4.

1.4 Water remediation with nanoparticles

The importance of fresh water is increasing worldwide. However, available water sources are limited; only the 2.5% of total water in earth is fresh water (97.5% of water is from saline sources like ocean) and only 1.2% of 2.5% fresh water is present on the surfaces of earth. Thus, 0.03% of total water is available in earth.[19] Furthermore, industrial water pollution is a major problem, reducing the amount of available water.[20] Also, water pollutants are naturally generated; the weathering of rocks containing arsenic derive heavy-metal pollution. Due to the various pollutants in water, there are strict rules of drinking waters about the concentration of micro-organism, organics, heavy metal, and disinfectant. Because the supply of fresh water is restricted, purifying the contaminated water into clean water is very important. Conventional water purification methods can eliminate the pollutants in water via sedimentation and

oxidation. However, the conventional purification methods require energies and should conduct multiple steps. To purify polluted water by eco-friend method, purification methods using nanomaterials have been researched widely.[21]

Advanced oxidation process

Advanced oxidation process (AOP) means the degradation process of water pollutants mediated by reactive oxygen radicals (ROS), mainly by hydroxyl radicals (·OH).[22] Through the AOP, aqueous organic pollutants and micro-organisms can be degraded. Particularly, ROS, generated during AOP, can effectively degrade the non-degradable materials such as aromatics and pesticides, volatile organic compounds (VOCs), and etc. The representative reactions of AOP are Fenton, photo-Fenton, and photocatalytic reactions.

Photocatalysis. Photocatalysis means the reaction which is facilitated by light irradiation.[23] Among various types of photocatalytic reactions, photocatalytic water purification refers to a reaction that decomposes contaminants in water using radicals. Semiconductor or metal nanoparticles are mainly used for the photocatalytic reactions. Semiconductor and metal nanoparticles generate excited electron-hole pairs when absorbed the photon, whose energy is larger than the band-gap energy of nanoparticles. The excited electrons in conduction bands reduce oxygen molecules (O_2) to form superoxide radicals ($\cdot O_2^-$). Also, excited holes in valence bands oxides hydroxyl ions

(OH^-) to form hydroxyl radicals (·OH). Furthermore, other radical species like HO_2^- are also formed. To enhance the photocatalytic activity of nanomaterials, the following conditions are required; low band-gap to absorb visible light, fast generation of photoexcited electron-hole pairs, long lifetime of excited electron-hole pairs.

Fenton reaction. Fenton reactions are the organic pollutants degradation reaction induced by hydroxyl radicals. For Fenton reaction, Fe^{2+} ions react with H_2O_2, forming Fe^{3+} and ·OH. The Fe^{3+} is then reduced to Fe^{2+} by another H_2O_2 molecules, generating HO_2·.

$$Fe^{2+} + H_2O_2 \rightarrow Fe^{3+} + HO\cdot + OH^- \quad (1)$$

$$Fe^{3+} + H_2O_2 \rightarrow Fe^{2+} + HOO\cdot + H^+ \quad (2)$$

$$2H_2O_2 \rightarrow HO\cdot + HOO\cdot + H_2O \quad (3)$$

The overall reaction mechanisms of the Fenton reaction are presented above.[24] The radicals formed during the reaction degrade organic pollutants. Thus, Fenton reactions have been applied to purify the water. However, Fenton reactions using Fe(II) ions generate iron sludge during the reactions.

Photo-Fenton reaction. Photo-Fenton reaction degrade organic pollutants by radicals, which are formed by the reactions between H_2O_2 and Fe ions under light irradiation. Fe complex absorb UV light and then react with H_2O_2 to generate hydroxyl radicals.[25] Hydrogen peroxide molecules can absorb UV light and are degraded into HO·. However, because the H_2O_2 molecules weakly absorb UV light, the generation rate of HO· is too slow. Thus, H_2O_2 cannot be applied to AOPs alone. The iron complexes or hydroxides

play an important role to facilitate the generate HO·.[26]

$$Fe^{2+} + H_2O_2 \rightarrow Fe^{3+} + OH^- + HO\cdot \quad (4)$$

$$Fe^{3+} + H_2O + h\nu \rightarrow Fe^{2+} + H^+ + HO\cdot \quad (5)$$

Adsorption

Adsorption has been commonly employed as a water-remediation step to remove organic and inorganic pollutants like organic dyes and heavy metals. Efficiency of traditional adsorbents is limited by the surface area or active sites, selectivity, and adsorption kinetics. However, nanoadsorbents have presented enhanced adsorption capacity due to the high surface area and numerous active sites. With the different synthetic methods and post-synthetic modification, the properties of active sites and pores could be adjusted, enhancing the adsorption capacity or selectivity. Most extensively applied adsorbents are carbon-derived adsorbents. Carbon-based adsorbents are suitable for the adsorption of dyes, phenol derivatives, and heavy metals.[27] Furthermore, metal chalcogenide such as metal oxide and sulfide are applied as adsorbents.[28] Nano-adsorbents can be readily applied into existing water treatments of slurry reactions or adsorbents. As in powder form, nanoadsorbents in slurry reaction can be highly efficient because of high surface area and selectivity. However, after the adsorption processes, nanoadsorbents have to be retrieved from the purified solution. Thus, nanoadsorbents are usually applied as the form of pellet, bead, and so on.

Separation membrane

Separation membrane means a membrane capable of separating organic or inorganic molecules in a gas or liquid phase.[29,30] The properties of the separation membrane depend on the composition or the synthetic method of the membrane, thereby allowing certain materials to selectively permeate through the membrane. Through the selective permeability, separation membranes that separate hydrocarbons, heavy metals, and organic pollutants have been synthesized. The separation membrane does not generate contaminants in the separation processes, and there is no need to remove the separation membrane after the separation process is over; adsorbents or photocatalysts have to be separated from the solution after water remediation processes through centrifugation, magnetic separation and so on. Accordingly, since the energy consumption is very low during and after the separation, it is possible to separate the molecules in eco-friendly manners. In addition, since separation membranes do not require high temperature as in distillation, it is possible to separate organic or biological samples from the mixture. In the liquid phase ultrafiltration and nanofiltration methods using pressure are typically used, and reverse osmosis and dialysis methods, which separate using concentration difference and material size, are also being studied in various fields. After the separation, the membranes can be easily reused by washing the separation membrane with a solvent or removing the adsorbed materials using a photocatalytic reaction. Polymers and metal-organic frameworks (MOFs) that are easy to control the size and characteristics of pores have been mainly used for membrane synthesis. Furthermore, metal or semiconductor based membranes have been researched widely.

1.5 References

[1] A. M. Ionescu, *Connections QJ*, **2016**, 15, 31.

[2] J. McKittrick, L. E. Shea-Rohwer, *J. Am. Chem. Soc.*, **2014**, 97, 1327.

[3] E. Roduner, *Chem. Soc. Rev.*, **2006**, 35, 583.

[4] L. Mino, G. Agostini, E. Borfecchia, D. Gianolio, A. Piovano, E. Gallo, C. Lamberti, *J. Phys. D: Appl. Phys.*, **2013**, 46, 423001.

[5] Y.-W. Jun, J.-S. Choi, J. Cheon, *Angew. Chem. Int. Ed.*, **2006**, 45, 3414.

[6] S.-M. Lee, S.-N. Cho, J. Cheon, *Adv. Mater.*, **2003**, 15, 441.

[7] J. Li, Q. Wu, J. Wu, Synthesis of Nanoparticles via Solvothermal and Hydrothermal Methods. In: Aliofkhazraei M. (eds), Handbook of Nanoparticles, *Springer*, **2015**.

[8] L. A. Kolahalam, I. V. Kasi Viswanath, B. S. Diwakar, B. Govindh, V. Reddy, Y. L. N. Murthy, *Materials Today: Proceedings*, **2019**, 18, 2182.

[9] A. P. LaGrow, M. O. Besenhard, A. Hodzic, A. Sergides, L. K. Bogart, A. Gavriilidis, N. T. K. Thanh, *Nanoscale*, **2019**, 11, 6620.

[10] K. Wenderich, G. Mul, *Chem. Rev.*, **2016**, 116, 14587.

[11] S. Bhaviripudi, E. Mile, S. A. Steiner III, A. T. Zare, M. S. Dresselhaus, A. M. Belcher, J. Kong, *J. Am. Chem. Soc.*, **2007**, 129, 1516.

[12] R. Ayyub, R. Chandra, P. Taneja, A. K. Sharma, R. Pinto, *Appl. Phys. A*, **2001**, 73, 67.

[13] M. K. Choi, J. Yang, T. Hyeon, D.-H. Kim, *NPJ Flex. Electron.*, **2018**, 2, 10.

[14] N. Nitta, F. Wu, J. T. Lee, G. Yushin, *Mater. Today*, **2015**, 18, 252.

[15] J.-R. Choi, D.-M. Shin, H. Song, D. Lee, K. Kim, *Nano Convergence*, **2016**, 3, 30.

[16] Z. Farka, T. Juřík, D. Kovář, L. Trnková, P. Skládal, *Chem. Rev.*, **2017**, 117, 9973.

[17] D. Choi, S. Ham, D.-J. Jang, *Mater. Res. Bull.*, **2019**, 120, 110578.

[18] G. Chen, I. Roy, C. Yang, P. N. Prasad, *Chem. Rev.*, **2016**, 116, 2826.

[19] P. H. Gleick, Water in Crisis: A Guide to the World's Fresh Water Resources, *New York: Oxford University Press*, **1993**, Chapter 1.

[20] S. J. Tesh, T. B. Scott, *Adv. Mater.*, **2014**, 26, 6056.

[21] A. Mishra, J. Clark, Green Materials for Sustainable Water Remediation and Treatment, *RSC*, **2013**, Chapter 1.

[22] Y. Deng, R. Zhao, *Curr. Pollution Rep.*, **2015**, 1, 167.

[23] M. N. Chong, B. Jin, C. W. K. Chow, C. Saint, *Water Res.*, **2010**, 44, 2997.

[24] M.-H. Zhang, H. Dong, L. Zhao, D.-X. Wang, D. Meng, *Sci. Total Environ.*, **2019**, 670, 110.

[25] R. G. Zepp, *Environ. Sci. Technol.*, **1992**, 26, 313.

[26] R. Bauer, G. Waldner, H. Fallmann, S. Hager, M. Klare, T. Krutzler, S. Malato, P. Maletzky, *Catal. Today*, **1999**, 53, 131.

[27] E. Santoso, R. Ediati, Y. Kusumawati, H. Bahruji, D. O. Sulistiono, D. Prasetyoko, *Mater. Today, Chem.*, **2020**, 16, 100233.

[28] L. Wang, C. Shi, L. Wang, L. Pan, X. Zhang, J.-J. Zou, *Nanoscale*, **2020**, 12, 4790.

[29] P. Pandey, R. S. Chauhan, *Prog. Polym. Sci.*, **2001**, 26, 853.

[30] S. Qui, M. Xue, G. Zhu, *Chem. Soc. Rev.*, **2014**, 43, 6116.

Chapter 2. Facile Photohydroxylation of ZnS Nanobelts for Enhanced Photocatalytic Activity†

† This is reproduced from Sooho Ham and Du-Jeon Jang, *J. Environ. Chem. Eng.*, **2018,** 6, 228-235. ⓒ 2018 Elsevier Inc.

2.1. Abstract

The photocatalytic performances of ZnS photocatalysts have been extensively enhanced by treating ZnS nanobelts for 10 min with hydrogen peroxide under Xe-lamp irradiation. The photocatalytic degradation reaction of 4-nitrophenol *via* photohydroxylated ZnS nanobelts takes place faster six times than that *via* pristine ZnS nanobelts, demonstrating that the simple and facile photohydroxylation process increases the photocatalytic activity of ZnS nanobelts extensively. Photoluminescence spectra and kinetic profiles have suggested that surface hydroxyl groups as well as surface defects increase the separation rate of photogenerated charges, enhancing the photocatalytic activity of 4-nitrophenol degradation. Radical species tests have indicated that the photocatalytic performance of ZnS nanobelts is mainly contributed by hydroxyl radicals generated by the photooxidation of surface-adsorbed hydroxyl groups. Because hydroxyl groups are adsorbed on the surfaces of photocatalysts, diffusion is not necessary when hydroxyl radicals are formed by photoexcited holes. Thus, the photocatalytic degradation of 4-nitrophenol *via* ZnS nanobelts follows the zero-order kinetics. The generation of hydroxyl radicals is promoted by the retarded recombination of photoexcited charges, leading to the enhancement of the photocatalytic activity of ZnS nanobelts. Overall, a simple and facile photohydroxylation process increases the photocatalytic performances of ZnS photocatalysts enormously *via* forming reactive hydroxyl radicals, which are readily generated by the photooxidation of surface-adsorbed hydroxyl groups. Overall, our facile and eco-friendly photohydroxylation method is suggested to have great potential for industrial applications.

2.2. Introduction

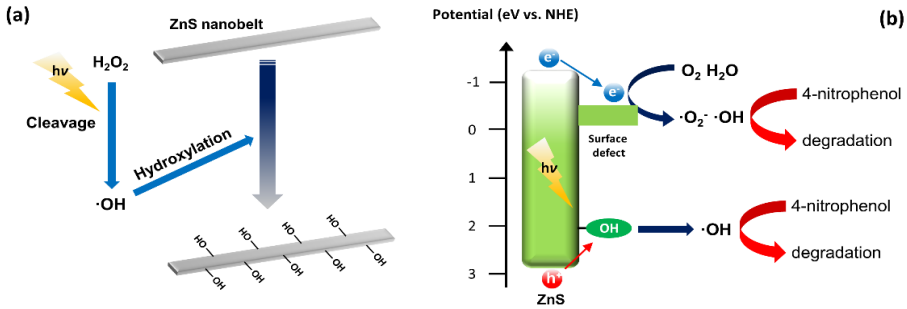

Figure 2-1 Schematic for the surface photohydroxylation of a ZnS nanobelt (a) and the photocatalytic degradation of 4-nitrophenol *via* a photohydroxylated ZnS nanobelt (b).

Recently, the presence of pollutants in water has increased concern about environmental and health problems.[1-4] It is hard for organic pollutants of phenol derivatives to be degraded because of their stability and solubility in water. Among them, 4-nitrophenol produced during pharmaceutical and chemical processes is one of the most common phenol derivatives. Advanced oxidation processes (AOP) such as photo-Fenton and electro-Fenton reactions have been widely used to eliminate water-dissolved 4-nitrophenol.[5-7] However, these reactions are known to cause secondary pollution by chemicals added during the degradation processes. Thus, degradation methods of 4-nitrophenol through eco-friendly manners have been studied intensively.[8-10] Among them, photocatalysis, which degrades organic pollutants *via* highly reactive radicals such as ·OH and $·O_2^-$

generated by photoexcited electrons and holes on the surface of semiconductors, have gained extensive interests.[11]

ZnS, one of chalcogenide semiconductors, has been studied extensively as photocatalyst materials owing to the proper energy levels of the conduction and valence bands and the rapid generation of excited electrons and holes by photoexcitation.[12] However, because of the wide band gap (3.77 eV for hexagonal wurtzite ZnS), the semiconductor of ZnS responses only to UV light. Furthermore, the recombination of excited electrons and holes is too fast in ZnS. These issues restrict ZnS to be applied as photocatalyst materials.[13,14] To solve these disadvantages, heterojunctions have been formed between ZnS and other materials such as different semiconductors and noble metals.[14-16] These heterojunctions have been known to increase the photocatalytic efficiency of ZnS by facilitating the separation of excited charges and by enhancing visible-light responses. However, to form these heterojunctions, additional precursors and reactions are needed, decreasing the usability of ZnS as photocatalysts.

Surface-existing hydroxyl groups have been known to form reactive hydroxyl radicals (·OH) by scavenging excited holes, enhancing photocatalytic properties.[17] Thus, by treating ZnS nanobelts with H_2O_2 under light irradiation, we have hydroxylated the surfaces of ZnS nanobelts (Figure 2-1a). The direct cleavage of H_2O_2 by UV light forms reactive hydroxyl radicals (·OH). Also, $\cdot O_2^-$ generated through the reduction of oxygen molecules by photoexcited electrons reacts with H_2O_2 to form hydroxyl radicals, and excited electrons in conduction bands reduce H_2O_2 to form hydroxyl radicals.[18,19] These reactive hydroxyl radicals hydroxylate the surfaces of ZnS nanobelts.[20] In addition, the

photohydroxylation process produces surface defects, which also facilitate the separation of excited charges to enhance the photocatalytic performances of ZnS nanobelts.[21] Thus, the facile photochemical treatment seems to be a proper method to block the recombination of excited charges *via* forming surface hydroxyl groups and defects, enhancing the photocatalytic efficiencies of ZnS nanobelts with no further addition of metal precursors. As-produced photohydroxylated ZnS nanobelts have shown much higher catalytic activity in the degradation of 4-nitrophenol than pristine ZnS nanobelts, due to enhanced charge separation by surface hydroxyl groups and surface defects (Figure 2-1b).

2.3. Experimental

2.3.1. Chemicals

While commercial ZnS particles (99.99%, 10 μm) and zinc chloride (s, >98%) were purchased from Sigma-Aldrich, ethylene diamine (l, 99%), hydrazine monohydrate (l, >98%), p-benzoquinone (s, >98%), sodium sulfite (s, 98%), and 4-nitrophenol (s, 99%) were obtained from Alfa-Aesar. Hydrogen peroxide (aq, 30%), sulfur (s, >97%), isopropyl alcohol (IPA, l, >99.5%), and ethanol (l, >99.0%) were acquired from Daejung Chemicals. Ultrapure deionized water (>15 MΩ cm) from an ELGA PURELAB Option-S system was used throughout the experiments.

2.3.2. Synthesis of photocatalysts

ZnS nanobelts were synthesized following a previously reported method.[22] For the photochemical surface hydroxylation of ZnS nanobelts, 100 mg of ZnS nanobelts was dispersed in 30 mL of water by sonication for 5 min and transferred into a quartz reaction vessel. Then, a specific amount of 30% H_2O_2(aq) was added to the aqueous colloid of ZnS nanobelts to make the molar ratio of H_2O_2 to ZnS be **R**. By adding additional water, the total volume of the mixture was kept as 40 mL for every synthetic batch. The reaction mixture was irradiated with a 300 W Xe lamp for a specific period (**t** in the unit of min). As-formed surface-hydroxylated ZnS nanobelts of $OH_{\mathbf{R(t)}}$ ZnS nanobelts were washed several times with water and ethanol and dried in a vacuum oven at 40 °C for 6 h.

2.3.3. Characterization

X-ray diffraction (XRD) patterns were obtained using a Bruker New D8 advance diffractometer with Cu K_α radiation (0.15418 nm) while X-ray photoelectron spectroscopy (XPS) was conducted using a ThermoVG Scientific SIGMA PROBE spectrometer having a 100 W Al anode. The transmission electron microscopy (TEM) morphologies of as-formed $OH_{R(t)}$ ZnS nanobelts were characterized with a Hitachi H-7600 microscope, and high-resolution TEM (HRTEM) images and energy-dispersive x-ray (EDX) maps were obtained through a JEOL JEM-2100F microscope. While diffuse-reflectance was measured with a StellaNet US/EPP 2000C spectrometer, photoluminescence spectra were obtained using an Ocean Optics USB2000+ detector with excitation of 266 nm pulses from a 6 ns Quantel Brilliant Nd:YAG laser. Photoluminescence decay kinetic profiles were measured employing a mode-locked Quantel Pizzicato Nd:YAG laser of 25 ps and a

Hamamatsu C2830 streak camera of 10 ps attached with a Princeton Instruments RTE128H CCD detector.

2.3.4. Photocatalytic performances

The photocatalytic efficiencies of as-produced $OH_{R(t)}$ ZnS nanobelts were measured by monitoring the photocatalytic degradation of 4-nitrophenol after addition of sodium sulfite. In a typical process, 40 mL of an aqueous solution containing 50 μM of 4-nitrophenol, an excess amount (0.15 g) of sodium sulfite, and 5.0 mg of a photocatalyst was prepared *via* sonicating the solution for 5 min. The solution was kept in dark for 1 h with stirring to establish the adsorption-desorption equilibrium of 4-nitrophenol on the surfaces of the photocatalyst, transferred into a quartz reaction vessel, and irradiated with a 300 W Xe lamp under magnetic stirring. An aliquot of 2.0 mL was taken from the solution at every 10 min and centrifuged at 13000 rpm for 10 min to obtain a supernatant. The UV-vis absorption spectrum of the supernatant was measured with a Scinco S-3100 spectrophotometer to check the concentration of remaining 4-nitrophenol. The concentration of 4-nitrophenol was calculated from the maximum absorbance of the absorption spectrum around 400 nm. By plotting the concentration of remaining 4-nitrophenol along with the reaction time, the rate constant of 4-nitrophenol degradation was calculated for each sample. Reactive oxygen radical species generated by the irradiation of the photocatalyst were investigated by radical scavenging tests; isopropyl alcohol and p-benzoquinone, widely known radical scavengers, were added to check photocatalytic efficiencies by photogenerated ·OH and $\cdot O_2^-$, respectively. To test the

recyclability of as-prepared $OH_{R(t)}$ ZnS nanobelts, the photocatalyst remaining after each cycle was centrifuged and re-dispersed in 40 mL of an aqueous solution containing 50 μM of 4-nitrophenol and 0.15 g of sodium sulfite. The photocatalytic activity of the recycled photocatalyst was measured again under the same conditions of the above mentioned process.

2.4. Results and discussion

2.4.1. Structural properties

The morphologies and structures of pristine ZnS nanobelts and $OH_{R(10)}$ ZnS nanobelts have been monitored through TEM analysis (Figure 2-2). As-produced pristine ZnS nanobelts represent smooth nanobelt morphologies with an average width of 50 nm and an average length of 1.5 μm (Figure 2-2a), while photochemically treated $OH_{R(10)}$ ZnS nanobelts portray coarse surfaces (Figure 2-2b-d). Although the surfaces of $OH_{R(10)}$ ZnS nanobelts were roughened after photohydroxylation processes, the intrinsic morphologies of nanobelts were maintained when R was 10 or 20. Hydroxyl radicals, generated by the cleavage of H_2O_2 under UV light, have hydroxylated ZnS nanobelts to make the surfaces of ZnS nanobelts harsh. For a given irradiation time of 10 min, the generation of hydroxyl radical has been increased with the increment of the R value, the molar ratio of H_2O_2 to ZnS during the photohydroxylation of ZnS nanobelts. The facilitated generation of hydroxyl radicals has caused more severe hydroxylation to ZnS nanobelts, leading to the more roughened surfaces of ZnS nanobelts.

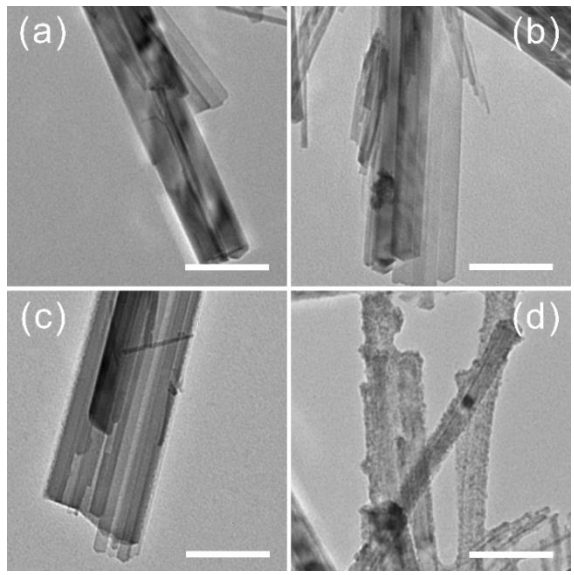

Figure 2-2 TEM images of pristine ZnS nanobelts (a), $OH_{10(10)}$ ZnS nanobelts (b), $OH_{20(10)}$ ZnS nanobelts (c), and $OH_{80(10)}$ ZnS nanobelts (d). Each scale bar represents 100 nm.

The detailed surfaces of a pristine ZnS nanobelt and an $OH_{10(10)}$ ZnS nanobelt have been characterized through HRTEM analysis. A pristine ZnS nanobelt has showed the high crystallinity of wurtzite ZnS. The observed lattice spacing value of 0.330 nm for the pristine ZnS nanobelt agrees reasonably well with the standard spacing of 0.331 nm between the (100) planes of wurtzite ZnS (Figure 2-3a). Meanwhile, the HRTEM image of an $OH_{10(10)}$ ZnS nanobelt displays additional amorphous surfaces (Figure 2-3b). Due to the high reactivity of hydroxyl radicals, surface defects have also been produced during the photohydroxylation process of the ZnS nanobelt. Because the surface vacancy defects have been formed by the leakage of S^{2-} and Zn^{2+} ions, the crystallinity of the ZnS nanobelt has been decreased, as represented in Figure 2-3b.

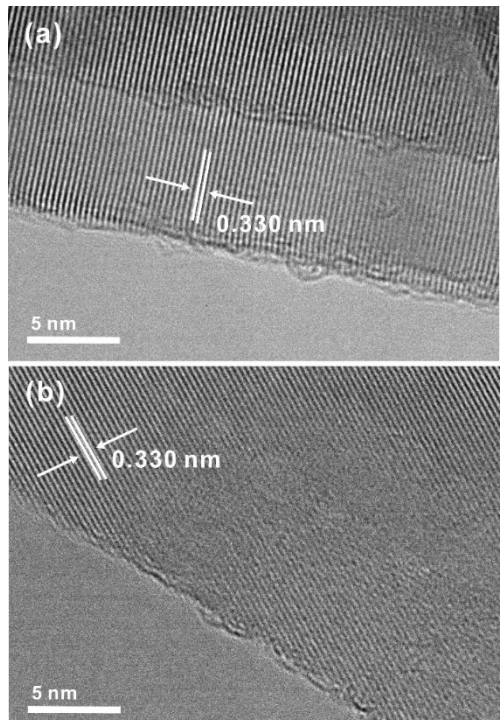

Figure 2-3 HRTEM images of a pristine ZnS nanobelt (a) and an $OH_{10(10)}$ ZnS nanobelt (b).

A TEM image and EDX elemental mapping data of a surface-hydroxylated $OH_{10(10)}$ ZnS nanobelt are presented in Figure 2-4. The EDX maps have been taken from the designated nanorod of Figure 2-4a. The distributions of Zn and S elements in the EDX data of Figure 2-4b,c suggest that the morphology of the ZnS nanobelt, prepared well by a hydrothermal method, has been maintained adequately during the photochemical treatment. In addition, the oxygen EDX map of Figure 2-4d shows that oxygen atoms are well distributed on the ZnS nanobelt, demonstrating that the surfaces of the ZnS nanobelt have been hydroxylated suitably by the photochemical treatment.

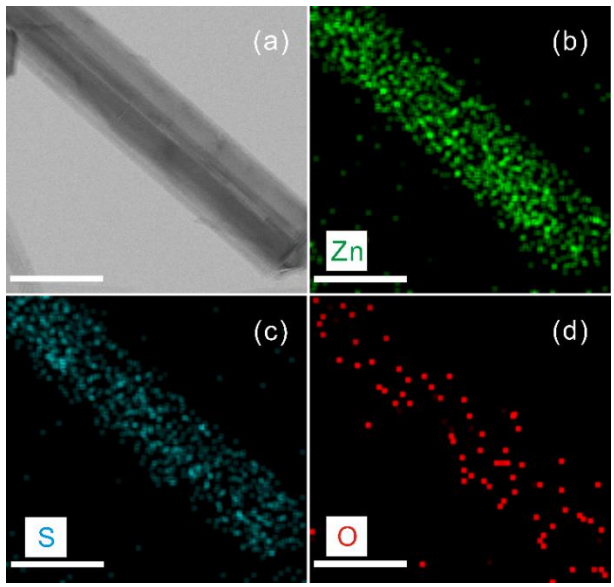

Figure 2-4 TEM image of an $OH_{10(10)}$ ZnS nanobelt (a) and EDX elemental maps of Zn (b), S (c), and O (d). Each scale bar represents 50 nm.

The XRD spectra of pristine ZnS and $OH_{R(10)}$ ZnS nanobelts, whose R values range from 5 to 40, are presented in Figure 2-5. All the diffraction peaks can be matched well with the respective reference ones of wurtzite ZnS (JCPDS card no. 36-1450), suggesting that crystals of ZnO or $Zn(OH)_2$ have not been produced during the photochemical treatment of ZnS nanobelts. In addition, the positions of individual peaks have not been shifted after the photochemical treatment, indicating that photochemically treated $OH_{R(10)}$ ZnS nanobelts maintain the crystallinity of wurtzite ZnS. The mean crystal sizes of pristine ZnS nanobelts and $OH_{R(10)}$ ZnS nanobelts have been calculated by using the Scherrer's equation (Table 2-1). The mean crystallite sizes of $OH_{R(10)}$ ZnS nanobelts are almost the same as the average crystallite size of pristine ZnS nanobelts, revealing that the crystallinity of wurtzite

ZnS nanobelts has been well maintained during the photochemical treatment although ZnS nanobelts have been hydroxylated by reactive hydroxyl radicals generated under UV irradiation.

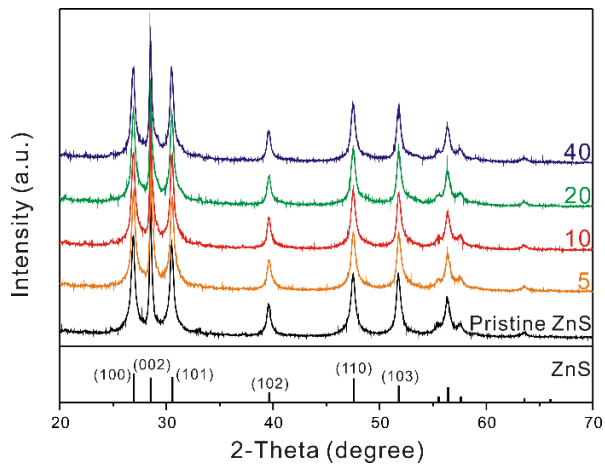

Figure 2-5 XRD spectra of pristine ZnS nanobelts and $OH_{R(10)}$ ZnS nanobelts, whose R values are indicated inside.

Table 2-1

The mean crystallite sizes of pristine ZnS nanobelts and $OH_{R(10)}$ ZnS nanobelts calculated using the Scherrer's equation.

Sample	Crystallite size (nm)
Pristine ZnS	24.7
$OH_{5(10)}$ ZnS	24.9
$OH_{10(10)}$ ZnS	24.8
$OH_{20(10)}$ ZnS	24.9
$OH_{40(10)}$ ZnS	24.4

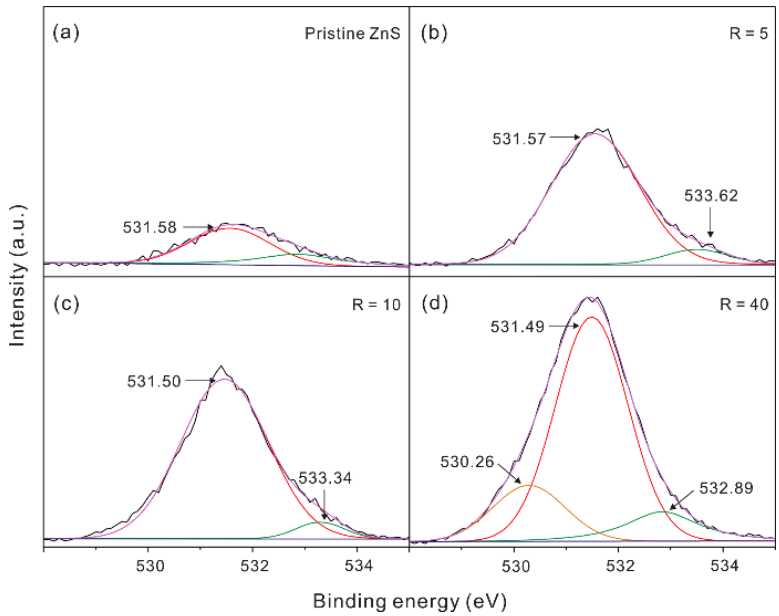

Figure 2-6 O 1s XPS spectra of pristine ZnS nanobelts (a) and $OH_{R(10)}$ ZnS nanobelts (b-d), whose R values are indicated inside.

XPS spectra have been measured to monitor changes in the surface states of ZnS nanobelts before and after the photochemical treatment. Each XPS spectrum of O 1s can be deconvoluted into two (Figure 2-6a-c) or three Gaussian bands (Figure 2-6d). The peak energies of 531.58 and 532.80 eV in the O 1s XPS spectrum of pristine ZnS nanobelts in Figure 2-6a can be attributed to the binding energies of a chemically adsorbed hydroxyl group and surface-adsorbed oxygen, respectively.[14,23,24] For the O 1s XPS spectra of $OH_{R(10)}$ ZnS nanobelts presented in Figure 2-6b-d, the peak with a binding energy between 531.49 and 531.57 eV increases extensively in intensity with the increase of the R value. It is known that the binding energy of an oxygen atom forming a Zn-OH bond corresponds to ~531.5 eV,[25-27] suggesting that hydroxylation has been proceeded on the surfaces of ZnS

nanobelts. For $OH_{40(10)}$ ZnS nanobelts, which have been prepared with an excess amount of hydrogen peroxide, a new peak attributable to metal-oxide bonds can be observed at 530.26 eV. This new peak reveals that the excess amount of hydrogen peroxide has oxidized the surfaces of the ZnS nanobelts to form Zn-O bonds.[24,27] The total oxygen atom content arising from adsorbed hydroxyl groups and surface-adsorbed oxygen, calculated from the peak intensities of Figure 2-6a, has been estimated as 3.74 wt% for pristine ZnS nanobelts. Meanwhile, the weight percentages of the oxygen element forming Zn-OH bonds after the photochemical treatment have been found as 10.57 (Figure 2-6b), 12.60 (Figure 2-6c), and 14.54 (Figure 2-6d) when R values are 5, 10, and 40, respectively, indicating that photochemical hydroxylation has taken place extensively and increasingly with the R value. In addition, Figure 2-7 indicates that the binding energies of both Zn $2p_{3/2}$ (at ~1022 eV) and S $2p_{3/2}$ peaks (at ~161 eV) increase with the increase of the R value. During the hydroxylation process, O, whose electronegativity (3.44) is higher than that of S (2.58) or Zn (1.65), has decorated the surfaces of ZnS nanobelts. Thus, the electron densities of S and Zn atoms have been decreased, leading to the decrease of electron repulsion in Zn and S atoms. The decrease of electron repulsion has resulted in the higher binding energies of electrons in the respective atoms, explaining the result of Figure 2-7.[14]

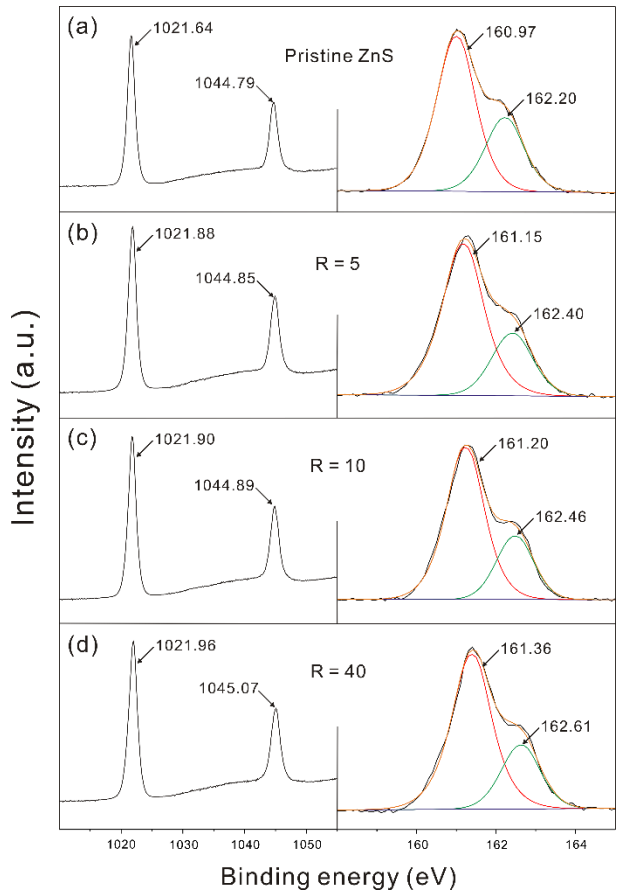

Figure 2-7 Zn 2p (left) and S 2p (right) XPS spectra of pristine ZnS nanobelts (a) and $OH_{R(10)}$ ZnS nanobelts (b-d), whose R values are indicated inside.

2.4.2. Optical properties

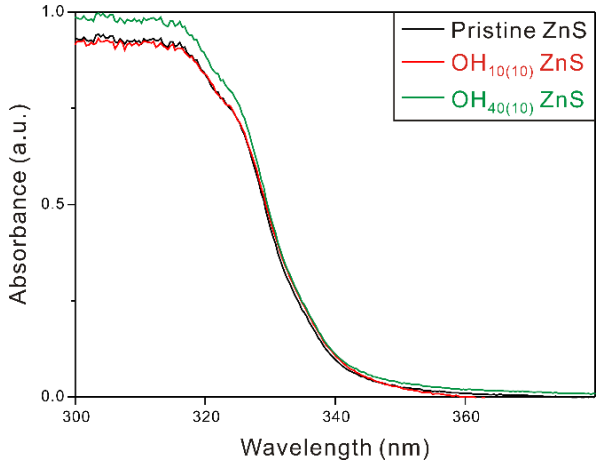

Figure 2-8 Diffuse-reflectance spectra of pristine ZnS nanobelts and $OH_{R(10)}$ ZnS nanobelts.

Table 2-2

Band-gap energies (eV) calculated from diffuse-reflectance spectra using Kubelka-Munk plots.

Sample	Band gap (eV)
Pristine ZnS	3.72
$OH_{5(10)}$ ZnS	3.72
$OH_{10(10)}$ ZnS	3.70
$OH_{20(10)}$ ZnS	3.69
$OH_{40(10)}$ ZnS	3.69

The diffuse-reflectance spectrum of pristine ZnS nanobelts presented in Figure 2-8 displays the typical UV-vis absorption band of wurtzite ZnS below 340 nm. The diffuse-reflectance spectra of $OH_{R(10)}$ ZnS nanobelts are nearly the same as that of pristine ZnS

nanobelts, suggesting that the UV-vis absorption spectrum of ZnS nanobelts has hardly been affected by the photochemical treatment. By using Kubelka-Munk plots,[15] the band-gap energies of individual samples have been calculated (Table 2-2). The band-gap energy of pristine ZnS nanobelts was estimated as 3.72 eV, which agrees suitably with the reference band-gap energy of bulk wurtzite ZnS (3.77 eV).[15] The band-gap energies of $OH_{R(10)}$ ZnS nanobelts are slightly smaller than that of pristine ZnS nanobelts and decrease with the increase of the R value. This is due to the energy levels of surface defects, which have been newly produced between the conduction band and the valence band of wurtzite ZnS during the photochemical treatment.

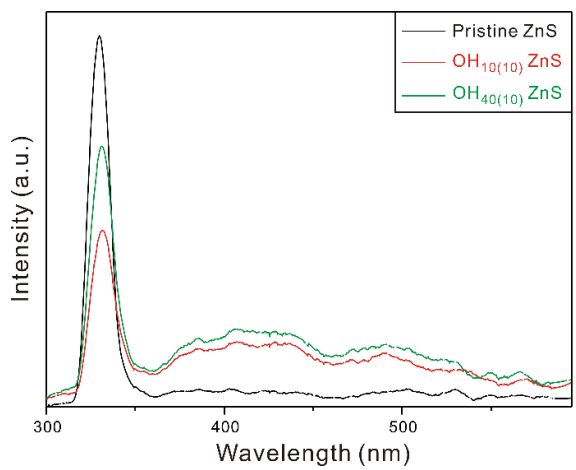

Figure 2-9 Photoluminescence spectra of pristine ZnS nanobelts and $OH_{R(10)}$ ZnS nanobelts dispersed in ethanol, with excitation at 266 nm.

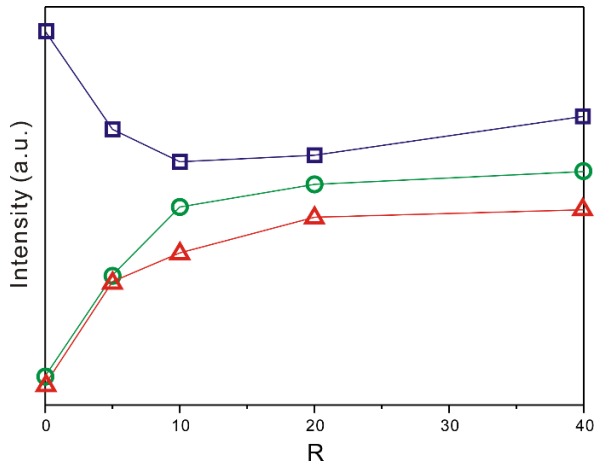

Figure 2-10 R-dependent photoluminescence intensity of $OH_{R(10)}$ ZnS nanobelts at 330 (blue), 430 (green), and 490 nm (red). All samples were dispersed in ethanol and excited with 266 nm.

To understand the degrees of charge separation in ZnS nanobelts before and after photohydroxylation, the photoluminescence (PL) spectra of pristine and $OH_{R(10)}$ ZnS nanobelts have been measured (Figure 2-9). Whereas pristine ZnS nanobelts show only an intense band-edge emission peak around 330 nm, $OH_{R(10)}$ ZnS nanobelts show two new defect-emission bands around 430 and 490 nm in addition to the band-edge emission peak with reduced intensity. Surface hydroxyl groups have been known to separate photogenerated charges by scavenging excited holes to form hydroxyl radicals.[17,28] This phenomenon hinders the recombination of excited electrons and holes, leading to the decrease of band-edge PL. The defect-emission bands of $OH_{R(10)}$ ZnS nanobelts around 430 and 490 nm can be attributed to the surface-defect states of sulfur vacancies and zinc vacancies, respectively.[21,29] The recombination of excited charges at surface-defect states

is much slower than that at band-edge states. Thus, surface-defect states also contribute to charge separation, leading to the enhancement of photocatalytic activity (see section 2.4.3).[21] Figure 2-10 show the R-dependent PL intensity variation of $OH_{R(10)}$ ZnS nanobelts at three selected wavelengths. Until R becomes 10, band-edge emission at 330 nm decreases and defect emission at 430 and 490 nm increases with the increase of R; in the early stage of hydroxylation, hydroxyl groups adsorbed to the surfaces of ZnS nanobelts produce surface defects, leading to charge separation that decreases band-edge emission and simultaneously increases defect emission with the increase of R. After R exceeds 10, band-edge emission at 330 nm increases with the increase of R; at high R values, excess hydroxylation takes place *via* forming $Zn(OH)_2$ nanoparticles on the surfaces of ZnS nanobelts. $Zn(OH)_2$ in bulk is known to have a wide band-gap of 5.1 eV.[30] Because amorphous $Zn(OH)_2$ has been formed during the photohydroxylation process, the band gap of surface-formed $Zn(OH)_2$ is wider than that of ZnS. Thus, surface-formed $Zn(OH)_2$ nanoparticles generate type-I heterojunctions with ZnS nanobelts, blocking further charge separation and facilitating the recombination of charges, leading to the increase of charge recombination and the decrease of photocatalytic activity (see section 2.4.3).

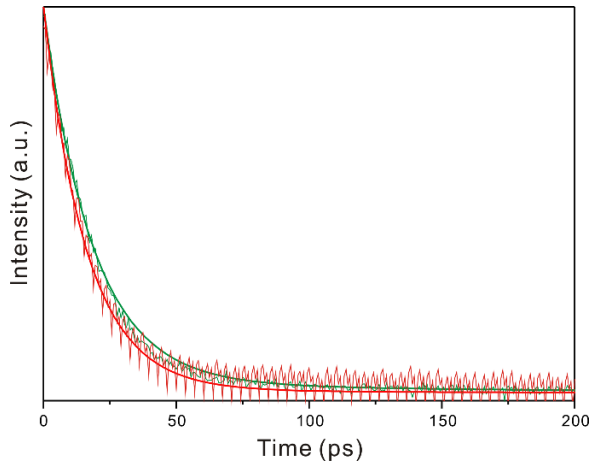

Figure 2-11 Photoluminescence decay kinetic profiles of pristine ZnS (green) and $OH_{10(10)}$ ZnS nanobelts (red) monitored at 325 ± 20 nm. Samples dispersed in ethanol were excited with 266 nm pulses. Solid lines are best-fitted curves.

Table 2-3

Emission decay kinetic constants of pristine ZnS nanobelts and $OH_{10(10)}$ ZnS nanobelts.

Sample	Decay time (ps)	Mean lifetime (ps)
Pristine ZnS	19 (97%) + 150 (3%)[a]	23
$OH_{10(10)}$ ZnS	16 (99%) + 100 (1%)	17

[a] Initial amplitude percentage of each component.

For further understanding of charge separation in ZnS nanobelts, the PL decay profiles of band-edge emissions around 330 nm have been measured (Figure 2-11). The respective PL decay profiles of pristine and $OH_{10(10)}$ ZnS nanobelts can be fitted with two exponential decay components and the results are presented in Table 2-3. The fast decay component of 19 ps and the slow one of 150 ps in pristine ZnS nanobelts correspond to the intrinsic

recombination of excited charges and the radiative decay of surface-trapped charges, respectively.[14] Figure 2-11 and Table 2-3 indicate that the decay times of both components for $OH_{R(10)}$ ZnS nanobelts are shorter than the respective decay times for pristine ZnS nanobelts, suggesting that additional charge separation has been taken place. Considering the mean PL lifetime of 23 ps for pristine ZnS nanobelts and the mean lifetime of 17 ps for $OH_{10(10)}$ ZnS nanobelts, we can calculate using Eq. (1)[33] that the charge-separation rate (k_{ET}) occurred additionally by surface-formed hydroxyl groups and surface defects in $OH_{10(10)}$ ZnS nanobelts is $(65\ ps)^{-1}$.

$$k_{ET} = [\tau_0(OH_{10(10)}\ ZnS)]^{-1} - [\tau_0(ZnS)]^{-1} \quad (1)$$

In other words, charge separation has been facilitated by the photochemical treatment on the time scale of 65 ps, revealing that the recombination of excited charges in ZnS nanobelts has been hindered by surface hydroxyl groups and surface defects. The decrement of charge recombination has enhanced the generation possibility of hydroxyl radicals, leading to the enhancement of photocatalytic efficiencies (see section 2.4.3). Meanwhile, it has not been possible for us to observe the decay kinetic profile of defect emission around 430 or 490 nm with our picosecond spectrometer system because the decay rate of defect emission is too slow to be measured in a picosecond time domain.[34]

2.4.3. Photocatalytic activities

The photocatalytic degradation reactions of 4-nitrophenol have been monitored under Xe-lamp irradiation (Table 2-4, Figure 2-12,13). The reaction kinetic profiles of Figure 2-

12 follow the zero-order kinetics in which the degradation rate remains invariant regardless of the remaining concentration of 4-nitrophenol. It is known that the zero-order reaction occurs only on the surface of a photocatalyst, independently with the diffusion of dye molecules.[31] Thus, our observed zero-order kinetic profiles reveal that the photocatalytic reactions of 4-nitrophenol *via* pristine nanobelts and $OH_{R(10)}$ ZnS nanobelts occur only on the surfaces of the photocatalysts. It has been found that $OH_{10(10)}$ ZnS nanobelts show the highest photocatalytic activity; the photocatalytic efficiency of $OH_{R(10)}$ ZnS nanobelts even decreases with R at high R values. We suggest that surface $Zn(OH)_2$ nanoparticles and excess surface defects generated during the photochemical reaction at high R value act as charge-recombination sites, thus resulting in the decrease of photocatalytic activity, as predicted by photoluminescence results.[32] The photocatalytic efficiency increases with the decrease of photoluminescence intensity, revealing that charge separation is the main factor to enhance the photocatalytic activity. Figure 2-12b and Table 2-4 reveal that the photocatalytic activity of $OH_{10(10)}$ ZnS nanobelts is higher 8.2 and 5.6 times than the respective activities of commercial ZnS particles and pristine ZnS nanobelts. This has demonstrated that the simple facile photohydroxylation of ZnS nanobelts enhances the photocatalytic activity of ZnS photocatalysts largely.

Table 2-4

Photocatalytic degradation rate constants of 4-nitrophenol *via* $OH_{R(t)}$ ZnS nanobelts.

Photocatalyst	Rate constant (μM min^{-1})
No catalyst	0.02
Commercial ZnS	0.13
Pristine ZnS	0.19
$OH_{0(10)}$ ZnS	0.23
$OH_{5(10)}$ ZnS	1.05
$OH_{10(0)}$ ZnS	0.85
$OH_{10(5)}$ ZnS	1.05
$OH_{10(10)}$ ZnS[a]	1.10
$OH_{10(20)}$ ZnS	1.15
$OH_{20(10)}$ ZnS	0.80
$OH_{40(10)}$ ZnS	0.75
$OH_{80(10)}$ ZnS	0.60

[a] The degradation rate constant of 4-nitrophenol *via* $OH_{10(10)}$ ZnS nanobelts under no light is 0.01 μM min^{-1}.

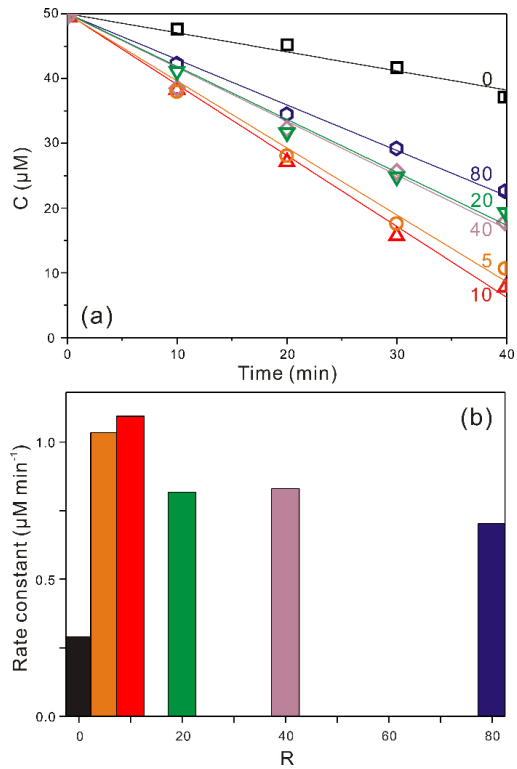

Figure 2-12 Zero-order plots (a) and rate constants (b) for the catalytic degradation of 4-nitrophenol *via* $OH_{R(10)}$ ZnS nanobelts, whose R values are indicated inside, under xenon-lamp irradiation.

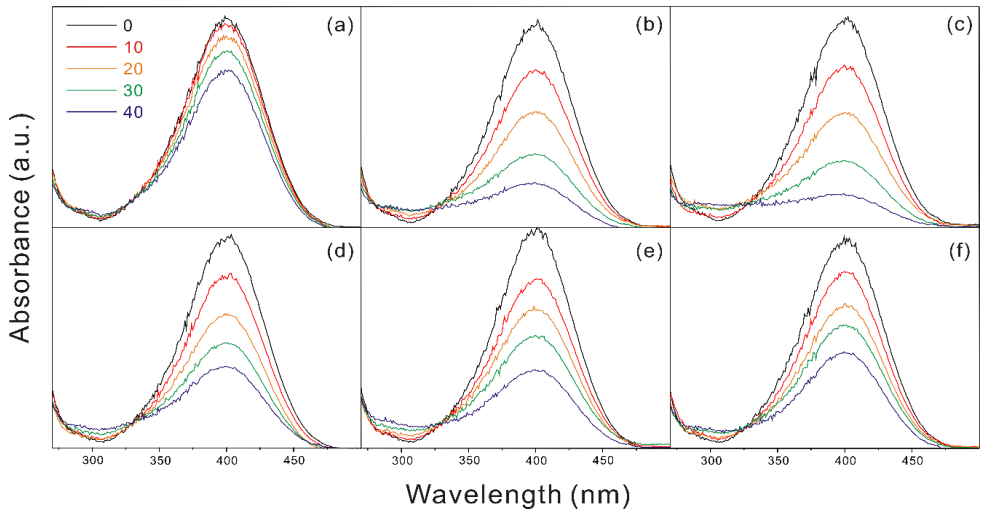

Figure 2-13 Absorption spectra of aqueous 4-nitrophenol solutions under Xe-lamp irradiation in the presence of pristine ZnS nanobelts (a) and $OH_{R(10)}$ ZnS nanobelts with R values of 5 (b), 10 (c), 20 (d), 40 (e), and 80 (f), measured at elapsed times indicated in the units of min.

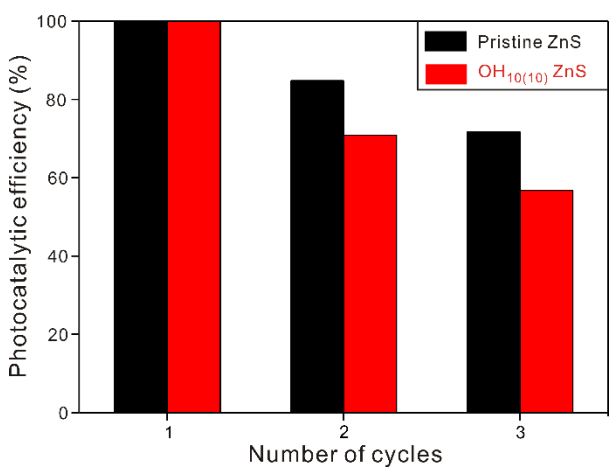

Figure 2-14 Recycling tests of pristine ZnS nanobelts (black) and $OH_{10(10)}$ ZnS nanobelts (red).

Additionally, we have tested the stability of as-formed $OH_{10(10)}$ ZnS nanobelts (Figure 2-14). The photocatalytic activities of pristine ZnS nanobelts and $OH_{10(10)}$ ZnS nanobelts have been decreased by 28% and 43%, respectively, after two recycling experiments, suggesting that the photochemical reaction has even worsened the stability of ZnS nanobelts in reality. However, it is noteworthy that the actual photocatalytic activity of $OH_{10(10)}$ ZnS nanobelts after two recycling experiments is still higher 4.4 times than that of pristine ZnS nanobelts.

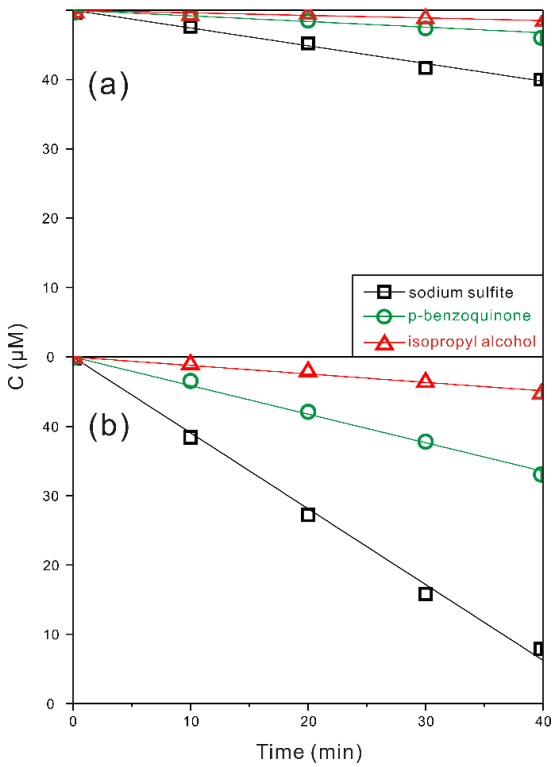

Figure 2-15 Photocatalytic degradation profiles of 4-nitrophenol *via* pristine ZnS nanobelts (a) and $OH_{10(10)}$ ZnS nanobelts (b) under indicated scavengers.

To figure out the photocatalytic mechanism of as-formed photocatalysts, radical species

tests have been conducted for pristine ZnS nanobelts and optimized $OH_{10(10)}$ ZnS nanobelts (Figure 2-15). The respective photocatalytic activities of pristine ZnS nanobelts and $OH_{10(10)}$ ZnS nanobelts under addition of radical scavengers (isopropyl alcohol (IPA) to monitor ·OH and p-benzoquinone (BQ) to monitor $\cdot O_2^-$) have been evaluated.[14] Photocatalytic degradation efficiencies of 4-nitrophenol *via* pristine ZnS nanobelts have been decreased by 85.5% and 68.3% when IPA and BQ, respectively, were added, suggesting that the photocatalytic performance of pristine ZnS nanobelts is mainly contributed by hydroxyl radicals generated by photoexcitation. Furthermore, the photocatalytic activity of $OH_{10(10)}$ ZnS nanobelts has been decreased by 88.8% and 62.3% when IPA and BQ, respectively, were added. This also demonstrates that the photocatalytic efficiency of $OH_{10(10)}$ ZnS nanobelts is mainly contributed by hydroxyl radicals. Thus, Figure 2-15 reveals that the photocatalytic degradation mechanism of 4-nitrophenol *via* ZnS nanobelts is not affected by the photohydroxylation process. ZnS is known as an n-type semiconductor, whose Fermi level is closer to the conduction band than the valence band. Thus, both the conduction band and the valence band bend toward a negative direction at surfaces in an aqueous phase, resulting in effective hole transfer to surfaces of ZnS nanobelts. Because the redox potentials of forming hydroxyl radicals by oxidizing surface hydroxyl groups and aqueous hydroxyl ions are about 1.6 and 2.5 eV vs. NHE, respectively,[35] the generation of hydroxyl radicals by excited holes on surfaces of ZnS is not blocked. Furthermore, because hydroxyl groups are adsorbed on the surfaces of photocatalysts, diffusion is not necessary when hydroxyl radicals are formed by photoexcited holes. Thus, photocatalytic reactions of 4-nitrophenol *via* ZnS nanobelts

follow the zero-order kinetics as shown in Figure 2-12. While sodium sulfite can act as hole scavengers,[36] excited holes oxidize hydroxyl groups to form hydroxyl radicals. Because hydroxyl groups are chemically adsorbed on the surfaces of ZnS nanobelts after the photohydroxylation process, the generation of hydroxyl radicals by photoexcited holes is not hindered by sodium sulfite dissolved in water. In summary, the radical species that plays the main role in the photocatalytic degradation of 4-nitrophenol *via* ZnS nanobelts is hydroxyl radicals, which are generated by the oxidation of surface-adsorbed hydroxyl groups and the reduction of surface-adsorbed oxygen molecules, as presented in Figure 2-1; the simple and facile hydroxylation of ZnS nanobelts facilitate the photocatalytic degradation of 4-nitrophenol by ZnS photocatalysts extensively *via* forming hydroxyl radicals effectively.

2.5. Conclusion

We have hydroxylated the surfaces of ZnS nanobelts by treating ZnS nanobelts with hydrogen peroxide under Xe-lamp irradiation. The photocatalytic degradation reaction of 4-nitrophenol *via* photohydroxylated ZnS nanobelts takes place faster six times than that *via* pristine ZnS nanobelts, demonstrating that the simple and facile photohydroxylation enhances the photocatalytic performances of ZnS nanobelts on a large scale. PL kinetic profiles and PL spectra suggest that surface hydroxyl groups as well as surface defects increase the separation rate of photogenerated charges with a rate constant of $(65\ ps)^{-1}$,

enhancing the photocatalytic activity of 4-nitrophenol degradation. The photocatalytic performances of ZnS nanobelts are mainly contributed by hydroxyl radicals generated by the photooxidation of surface-adsorbed hydroxyl groups. The generation of these radicals is promoted by the retarded recombination of photoexcited charges, leading to the enhancement of the photocatalytic activity of ZnS nanobelts. The photocatalytic reactions follow the zero-order kinetics because hydroxyl radicals are produced by the oxidation of surface-adsorbed hydroxyl groups. Overall, a simple and facile photohydroxylation process enhances the photocatalytic activity of ZnS photocatalysts *via* forming reactive hydroxyl radicals, which are generated by the photooxidation of surface-adsorbed hydroxyl groups.

2.6. Acknowledgements

This work was financially supported by the National Research Foundation of Korea (research grants: 2015-051798 and 2017-006153).

2.7. References

[1] C.-C. Wang, J.-R. Li, X.-L. Lv, Y.-Q. Zhang, G. Guo, *Energy Environ. Sci.*, **2014**, 7, 2831.

[2] M. S. El-Shahawi, A. Hamza, A. S. Bashammakh, W. T. Al-Saggaf, *Talanta*, **2010**, 80, 1587.

[3] S. J. Tesh, T. B. Scott, *Adv. Mater.*, **2014**, 26, 6056.

[4] M. F. Abid, G. M. Alwan, L. A. Abdul-Ridha, *Arab. J. Sci. Eng.*, **2016**, 41, 2659.

[5] B. Zhao, G. Mele, I. Pio, J. Li, L. Palmisano, G. Vasapollo, *J. Hazard. Mater.*, **2010**, 176, 569.

[6] H. Zhang, C. Fei, D. Zhang, F. Tang, *J. Hazard. Mater.*, **2007**, 145, 227.

[7] Y. Y. Chu, Y. Qian, W. J. Wang, X. L. Deng, *J. Hazard. Mater.*, **2012**, 199-200, 179.

[8] J. Li, C.-Y. Liu, Y. Liu, *J. Mater. Chem.*, **2012**, 22, 8426.

[9] W. Zhang, X. Xiao, T. An, Z. Song, J. Fu, G. Sheng, M. Cui, *J. Chem. Technol. Biotechnol.*, **2003**, 78, 788.

[10] G. Palmisano, V. Loddo, H. H. E. Nazer, S. Yurdakal, C. Augugliaro, R. Ciriminna, M. Pagliaro, *Chem. Eng. J.*, **2009**, 155, 339.

[11] S. Ahmed, M. G. Rasul, W. N. Martens, R. Brown, M. A. Hashib, *Desalination*, 2010, **261**, 3.

[12] J.-S. Hu, L.-L. Ren, Y.-G. Guo, H.-P. Liang, A.-M. Cao, L.-J. Wan, C.-L. Bai, *Angew. Chem. Int. Ed.*, **2005**, 44, 1269.

[13] H. Yin, Y. Wada, T. Kitamura, S. Yanagida, *Environ. Sci. Technol.*, **2001**, 35, 227.

[14] J. Lee, Y. Kim, J. K. Kim, S. Kim, D.-H. Min, D.-J. Jang, *Appl. Catal. B: Environ.*, **2017**, 205, 433.

[15] S. Ham, Y. Kim, M. J. Park, B. H. Hong, D.-J. Jang, *RSC Adv.*, **2016**, 6, 24115.

[16] J. Zhang, Y. Wang, J. Zhang, Z. Lin, F. Huang, J. Yu, *ACS Appl. Mater. Interfaces*, **2013**, 5, 1031.

[17] J. Wang, X. Liu, R. Li, P. Qiao, L. Xiao, J. Fan, *Catal. Commun.*, **2012**, 19, 96.

[18] N. M. Mahmoodi, M. Arami, N. Y. Limaee, N. S. Tabrizi, *Chem. Eng. J.*, **2005**, 112, 191.

[19] C. M. So, M. Y. Cheng, J. C. Yu, P. K. Wong, *Chemosphere*, **2002**, 46, 905.

[20] J. Aguilera-Sigalat, A. Fox-Charles, D. Bradshaw, *Chem. Commun.*, **2014**, 50, 15453.

[21] X. Wang, J. Shi, Z. Feng, M. Li, C. Li, *Phys. Chem. Phys. Chem.*, **2011**, 13, 4715.

[22] Y. Kim, S. J. Kim. S.-P. Cho, B. H. Hong, D.-J. Jang, *Sci. Rep.*, **2015**, 5, 12345.

[23] D. Chen, W. Shen, S. Wu, C. Chen, X. Luo, L. Guo, *Nanoscale*, **2016**, 8, 7172.

[24] P. Guo, J. Jiang, S. Shen, L. Guo, *Int. J. Hydrogen Energy*, **2013**, 38, 13097.

[25] T. Zhou, Z, Cao, P. Zhang, H. Ma, Z. Gao, H. Wang, Y. Lu, J. He, Y. Zhao, *Sci. Rep.*, **2017**, 7, 46154.

[26] H. Li, S. Jiao, J. Ren, H. Li, S. Gao, J. Wang, D. Wang, Q. Yu, Y. Zhang, L. Li, *Phys. Chem. Chem. Phys.*, **2016**, 18, 4144.

[27] R. Al-Gaashani, S. Radiman, A. R. Daud, N. Tabet, Y. Al-Douri, *Ceram. Int.*, **2013**, 39, 2283.

[28] P. Du, A. Bueno-López, M. Verbaas, A. R. Almeida, M. Makkee, J. A. Moulijn, G. Mul, *J. Catal.*, **2008**, 260, 75.

[29] Y. Kim, D.-J. Jang, *RSC Adv.*, **2013**, 3, 16945.

[30] E. A. Kozlova, D. V. Markovskaya, S. V. Cherepanova, A. A. Saraev, E. Y. Gerasimov, T. V. Perevalov, V. V. Kaichev, V. N. Parmon, *Inter. J. Hydrogen Energy*, **2014**, 39, 18758.

[31] J. Ungelenk, C. Feldmann, *Appl. Catal. B: Environ.*, **2012**, 127, 11.

[32] D. Jiang, L. Cao, G. Su, H. Qu, D. Sun, *Appl. Surf. Sci.*, **2007**, 253, 9330.

[33] D. Choi, J.-Y. Pyo, D.-J. Jang, *Nanoscale Res. Lett.*, **2017**, 12, 1.

[34] Y. Kim, J.-Y. Kim, D.-J. Jang, *J. Phys. Chem. C*, **2012**, 116, 10296.

[35] L. V. Trandafilović, D. J. Jovanović, X. Zhang, S. Ptansińska, M. D. Dramićanin, *Appl. Catal. B: Environ.*, **2017**, 203, 740.

[36] M. J. Berr, A. Vaneski, C. Mauser, S. Fischbach, A. S. Susha, A. L. Rogach, F. Jäckel, J. Feldmann, *Small*, **2012**, 8, 291.

Chapter 3. Facile Fabrication of Porous ZnS Nanostructures with Controlled Amount of S Vacancies for Enhanced Photocatalytic Performances†

† This is reproduced from Jaewon Lee, Sooho Ham, Dayeon Choi, and Du-Jeon Jang, *Nanoscale*, **2018,** 10, 14254-14263.

3.1. Abstract

ZnS nanostructures of barbell-shaped porous and hollow nanoplates with controlled amount of S vacancies have been facilely fabricated *via* the hydrothermal treatment of $ZnS(en)_{0.5}$ (en = ethylenediamine) nanoplates. The amount of S vacancies as well as the morphologies of ZnS nanostructures has been controlled by adjusting the hydrolysis time; the layered structure of $ZnS(en)_{0.5}$ nanoplates decomposes to yield discrete ZnS nanoparticles at two end facets of template nanoplates, producing barbell-shaped porous and hollow ZnS nanoplates with abundant S vacancies finally. The photocatalytic activity of ZnS nanostructures prepared *via* hydrolysis for 4 h is 8.2 time larger than that of commercial ZnS. The photocatalytic activity of ZnS nanostructures increases with the increase of emission at 390 nm arising from sulfur vacancies, suggesting that the high photocatalytic efficiency of ZnS nanostructures results mainly from the rich amount of sulfur vacancies. Surface defects such as sulfur vacancies can trap photogenerated electrons to block the recombination of charges, enhancing the photocatalytic efficiency of as-prepared ZnS nanostructures. It has been also found that both ·OH and $\cdot O_2^-$ act as major reactive species in the photocatalytic decomposition of rhodamine B *via* our prepared ZnS nanostructures. Barbell-shaped porous and hollow ZnS nanoplates are suggested to have great applicability to photocatalysts in waste-water treatment.

3.2. Introduction

Semiconductor nanomaterials having two-dimensional (2D) structures, such as nanoplates and nanosheets, have attracted significant attentions due to their unique properties in electrochemical and optoelectronic applications.[1,2] Although 2D nanostructures have been applied less frequently than one-dimensional nanostructures, they can be employed adequately as photocatalysts because of their peculiar structural features such as nanoscale thickness and predominantly exposed specific crystal facets.[3-5,8] Single-crystalline porous nanostructures possess further structural advantages such as a large pore volume, a high surface area, and less grain boundaries, providing large active sites as well as rapid charge-transport abilities for surface catalytic reactions.[1-3,9] However, in spite of theses structural benefits, high cost and complicated preparation processes have been considered as drawbacks to overcome. Alternatively, the thermal decomposition of organic-inorganic hybrid precursor templates can be an efficient way to generate pores when water or other volatile molecules leave from the solid composite precursor templates;[10-13] composites hybrid precursors based on II-VI semiconductors, MQ(L)n (M = Zn, Cd; Q = Se, Te, S; L = amine derivatives; n = 1 or 0.5), have been produced facilely *via* solvothermal solvent-coordination molecular-template methods.[13-16] Furthermore, the MQ(L)n hybrid nanocomposites exhibit a strong quantum-confinement effect due to perfectly periodic crystal structures composed of atomic sheets.[15-19]

The transformation of MQ(L)n nanocomposites into MQ nanostructures *via* solvent-assisted thermal treatment or high-temperature annealing inevitably causes crystal defects

due to an atom rearrangement process, and subsequently evolves void and porous structures to maintain thermodynamical stabilities.[13,20] Crystal defects such as points, lines, and volume defects can have positive effects on photocatalytic activity.[3-5] It has been reported that the amount of surface defects such as vacancies and interstitials of atoms is important to the photocatalytic efficiency.[20-24] Surface defects not only offer adsorption sites, where charges transfer to adsorbed molecules, but also produce new midterm states (namely, defect states or defect energy levels) in the band gap, facilitating the separation of photogenerated charge carriers; on the contrary, in the case of excessive defects, defects sites can operate as recombination sites of charge carriers, leading to the decrease of the photocatalytic efficiency.[6,7,25-30] Thus, controlling the amount of surface defects has been considered importantly to enhance photocatalytic performances.

Recently, ZnS nanostructures having a wide band gap (~3.8 eV) have been extensively investigated for applications in photocatalysis because they rapidly produce photogenerated charge carriers having considerably negative potential.[22,23,27,31-36] In addition, the wurtzite structure of ZnS exhibits ±(0001) polar surfaces; the ±(0001) surfaces are terminated with positively charged Zn ions and negatively charged S ions, inducing spontaneous polarization across the ZnS nanostructure from the S-terminated plane to the Zn-terminated plane; the polarization electric field promotes further the separation of photogenerated electrons and holes, facilitating charge carriers to move to the surfaces of ZnS materials.[35,36]

In this work, we are reporting that $ZnS(en)_{0.5}$ (en = ethylenediamine) nanoplates employed as sacrificial precursor templates have been successfully transformed into ZnS

nanostructures of barbell-shaped porous and hollow nanoplates *via* facile hydrothermal treatment (Figure 3-1). Furthermore, we have controlled not only the morphologies but also sulfur vacancies of ZnS nanostructures by varying the hydrothermal treatment time. It has been found that the defect amount, surface area, and pore volume of ZnS nanostructures are largest, resulting in the highest photocatalytic activity, when $ZnS(en)_{0.5}$ nanoplates were hydrolyzed for 4 h. The photocatalytic activity of ZnS nanostructures increases with the increase of emission at 390 nm arising from sulfur vacancies, suggesting that the high photocatalytic efficiency of ZnS nanostructures results mainly from the rich amount of sulfur vacancies. We consider that this work offers a novel approach for the fabrication of effective photocatalysts *via* engineering the intrinsic defects of nanostructures.

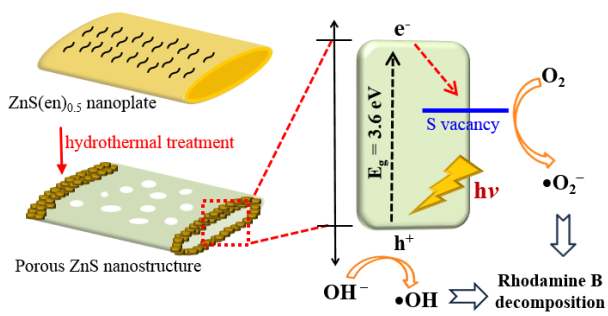

Figure 3-1 Schematic for the photodegradation mechanism of rhodamine B over a ZE nanostructures.

3.3. Experimental

3.3.1. Materials

All chemicals were employed without further purification: $ZnCl_2$ (>98%), ZnS (99.99%), and terephthalic acid (TA, 98%) from Sigma-Aldrich; p-benzoquinone (BQ, >98%), $N_2H_4 \cdot H_2O$ (98%), ammonium oxalate (AO, 99%), and ethylenediamine (en, 99%) from Alfa Aesar; isopropyl alcohol (IPA, >99.5%), sulfur (>99.0%), ethanol (>99.0%), NaOH (>97%), and ethylene glycol (EG, >99.0%) from Daejung Chemicals; rhodamine B (RhB) from Wako Pure Chemical. Water (>15 MΩ cm) purified with an Elga PURELAB system was utilized throughout the experiments.

3.3.2. Preparation of $ZnS(en)_{0.5}$ nanoplates and ZnS nanostructures

In typical preparation of inorganic-organic hybrid precursor $ZnS(en)_{0.5}$ nanoplates, 2.0 mmol of $ZnCl_2$, 2.0 mmol of sulfur, 20 mL of ethylenediamine, and 10 mL of $N_2H_4 \cdot H_2O$ were mixed by stirring for 30 min.[37] Then, the mixture solution was added to an autoclave having a capacity of 50 mL. The autoclave was placed for 9 h inside an oven at 180 °C. Produced $ZnS(en)_{0.5}$ nanoplates were centrifuged, washed with water and ethanol, and dried for 6 h in a vacuum oven at 60 °C.

Barbell-shaped porous ZnS nanostructures were prepared by placing an autoclave containing 40 mg of precursor $ZnS(en)_{0.5}$ nanoplates and 30 mL of water at 120 °C for a specific time. Then, the produced resultant product was washed with water and ethanol to

eliminate the residual impurities and dried at 60 °C in a vacuum oven for 6 h. Note that ZnS nanostructures fabricated by hydrolyzing ZnS nanostructures for x h will be designated as ZEx: for example, ZnS nanostructures fabricated by hydrolysis for 4 h will be called as ZE4.

3.3.3. Characterization

Transmission electron microscopy (TEM) images were measured with a Hitachi H-7600 microscope, whereas high-resolution X-ray diffraction (HRXRD) patterns were measured with a Bruker D8 DISCOVER diffractometer employing Cu K_α radiation (0.15418 nm). Scanning electron microscopy (SEM) images and energy-dispersive X-ray (EDX) elemental profiles were recorded with a MERLIN Compact microscope. Fast Fourier transformation (FFT) patterns and high-resolution TEM (HRTEM) images were obtained using a Tecnai F20 microscope, and EDX spectra were obtained employing a JEOL JEM-2100F microscope. Thermo gravimetric analysis (TGA) was carried out with a TA Instruments Q-5000 IR analyzer, while Fourier-transformed infrared (FTIR) spectra were taken with a Thermo Scientific Nicolet 6700 spectrometer. X-ray photoelectron spectroscopy (XPS) was conducted utilizing a KRATOS AXIS-HSi spectrometer with a 150 W Mg anode. Binding energies were calibrated by employing the 1s peak of contaminated carbon at 284.5 eV. N_2 adsorption–desorption isotherms were measured by operating a Nova 2200e Quantachrome instrument. Photoluminescence (PL) spectra were obtained by employing an Ocean Optics USB2000+ detector with 266 nm excitation pulses from a 6 ns Q-switched Quantel Brilliant Nd:YAG laser.

3.3.4. Photocatalytic properties

The photocatalytic activity of as-obtained ZnS nanostructures were examined by observing the photodegradation of RhB under light irradiation. 5.0 mg of the nanocatalysts was placed into a tubular quartz reactor containing 30 mL of a 10 µM RhB aqueous solution. The mixture was agitated for 1 h in the dark to establish an equilibrium of adsorption-desorption and then was exposed entirely to the light beam of a 300 W Xe lamp under ambient conditions. An aliquot was taken out from the reactor at a scheduled time and centrifuged (12000 rpm for 10 min) to remove any sediment. The concentration of remnant RhB in the aliquot was measured by monitoring a UV/vis absorption spectrum with a Scinco S-3100 spectrometer. The quantification of hydroxyl radicals (·OH) generated on the surfaces of nanocatalysts was obtained by measuring the PL of 2-hydroxyterephthalic acid (TAOH) generated by the reaction of •OH with TA; 0.5 mg of nanocatalysts was placed into a 30 mL aqueous solution of 2 mM NaOH and 0.5 mM TA in the same reactor.[9] The experimental process was nearly the same as that in the observation of photocatalytic efficiencies except that RhB was replaced by NaOH and TA. The PL spectra of TAOH at 420 nm were obtained with excitation at 315 nm utilizing a JASCO FP-8300 fluorescence spectrometer.

3.4. Results and discussion

3.4.1. Structural analysis

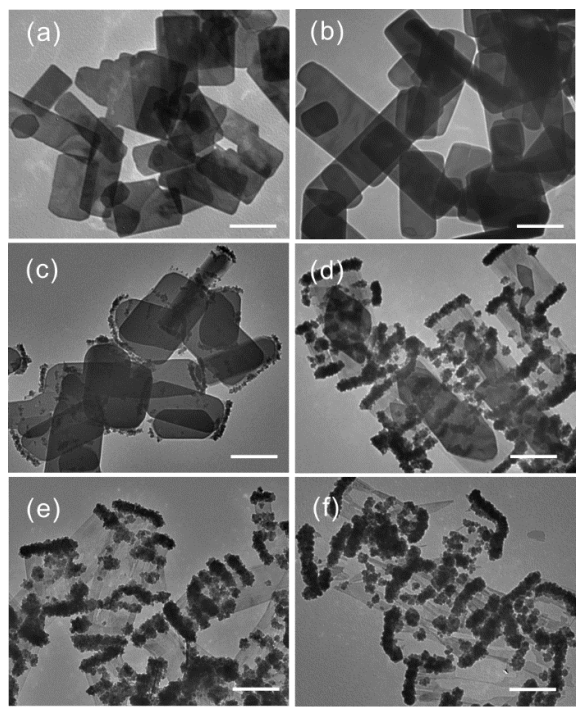

Figure 3-2 TEM images of ZE0 (a), ZE1 (b), ZE2 (c), ZE3 (d), and ZE5 (f). Each scale bar indicates 500 nm.

In order to investigate the morphology transformation of orthorhombic $ZnS(en)_{0.5}$ nanoplates consisting of organic-inorganic layers during the hydrothermal treatment, TEM images have been observed as a function of the hydrolysis time (Figure 3-2); as the reaction time increases from 0 to 5 h, ethylenediamine molecules intercalated at ZnS interlayer spaces are released progressively, producing barbell-shaped porous wurtzite ZnS

nanostructures in the treatment time of 4 h (see below).[11,13] Figure 3-2 indicates that highly dark regions arising from ZnS nanoparticles produced at the ends of template nanoplates start to appear from the hydrolysis time of 2 h. After the treatment time of 4 h, there are no dark regions, due to $ZnS(en)_{0.5}$, in the central domains of produced ZnS nanostructures, implying ethylenediamine molecules have been completely removed by the hydrolysis reaction; ZnS nanoparticles produced *via* hydrolysis have been heavily aggregated at two ends of generated porous ZnS nanoplates, producing barbell-shaped porous and hollow ZnS nanoplates finally (see below).[38-40]

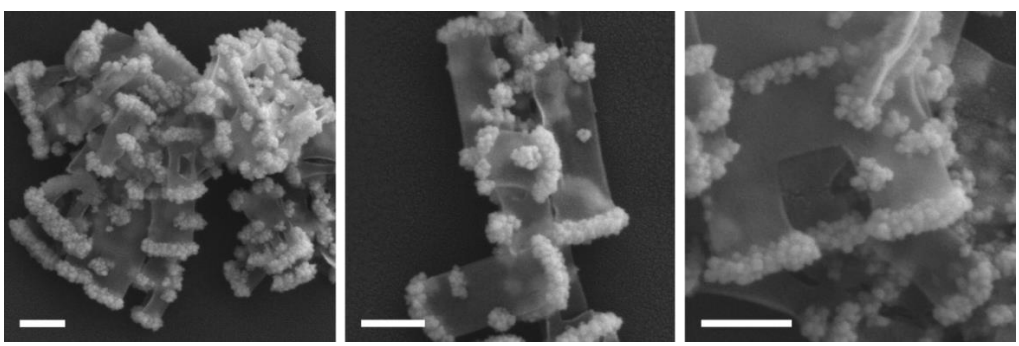

Figure 3-3 SEM images of ZE4 nanostructures. Each scale bar represents 200 nm.

In addition, as shown in Figure 3-3, SEM images support the above mentioned descriptions well. The layered structure of $ZnS(en)_{0.5}$ nanoplates decomposes to reconstruct surfaces during the high-temperature treatment process, yielding discrete nanoparticles at two end facets of template nanoplates to reduce the surface energy and to increase the stability.[3,11,12,18] In the synthetic mechanism of $ZnS(en)_{0.5}$ nanoplates, the stability of each facet is different; wurtzite ZnS nanostructures often grow along the (001)

direction, because atoms in this direction have a stronger bond force than atoms at other positions and assembly along the (001) direction can reduce the interface energy.[38] Thus, when fragmented ZnS nanoparticles begin to aggregate on $ZnS(en)_{0.5}$ templates, ZnS nanoparticles aggregate at two end facets of nanoplates, forming barbell-shaped porous ZnS nanostructures. Furthermore, aggregated ZnS nanoparticles derived from the fragmentation of $ZnS(en)_{0.5}$ nanoplates have been found to contain defects richly (see below). It should be also noted that hydrothermally produced ZnS nanostructures retain the nearly original plate-like morphologies of precursor $ZnS(en)_{0.5}$ nanotemplates with the original lengths of 800±80 nm and the initial widths of 400±30 nm. After the treatment time of 5 h, the porous nanowalls of barbell-shaped porous and hollow ZnS nanostructures have been broken partially and aggregated to obtain the thermodynamical stability *via* reducing surface areas.[41,42] In order to investigate a role of water in hydrothermal treatment, we have also prepared ZE nanostructure in solutions containing EG (Figure 3-4). While the hydrolysis reaction has not occurred in pure EG, it has taken place slowly in a 1:1 water:EG mixture, clearly demonstrating that water plays an important role in the hydrolysis of $ZnS(en)_{0.5}$ nanoplates.

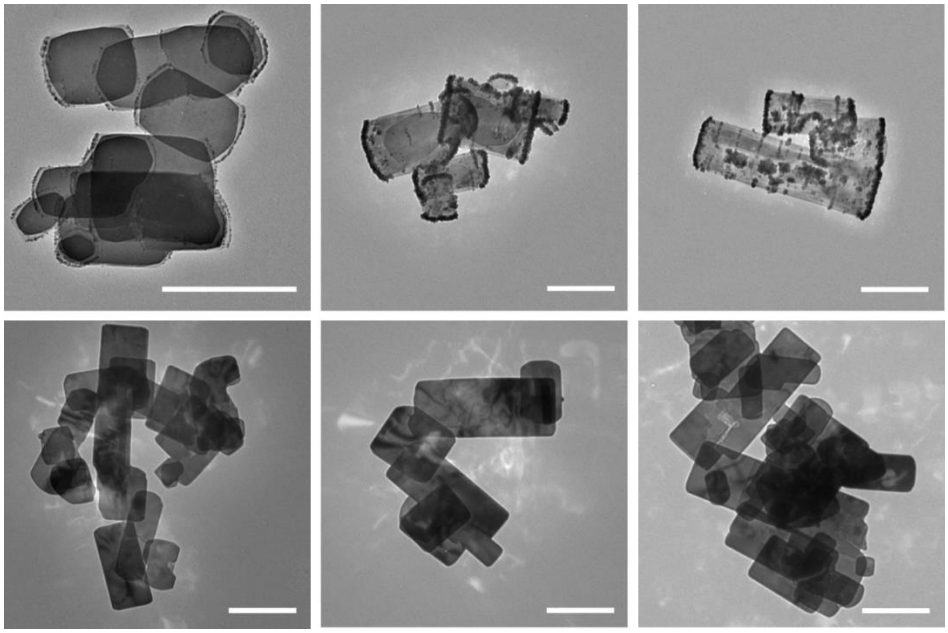

Figure 3-4 TEM images of ZE2 (left), ZE4 (middle), and ZE5 (right) prepared *via* hydrothermal treatment in a 1:1 water:EG mixture (top) and pure EG (bottom). Each scale bar represents 500 nm.

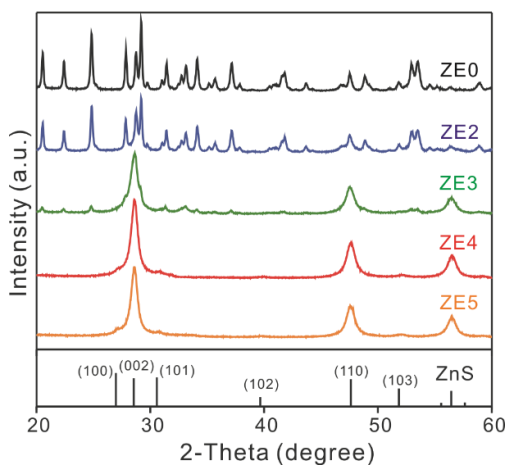

Figure 3-5 HRXRD patterns of indicated nanostructures. The standard diffraction lines of wurtzite ZnS.

Table 3-1

Crystallite sizes and elemental compositions of ZE nanostructures

Sample	Crystallite size[a] (nm)	Element (atomic %)		S vacancy (atomic %)[b]
		Zn	S	
ZE0	32.6	52	48	8
ZE2	29.4	55	45	18
ZE3	12.9	57	43	25
ZE4	11.0	59	41	31
ZE5	10.1	56	44	21

[a] Calculated from the (110) diffractions of XRD patterns. [b] Calculated from (1-S/Zn)100.

The HRXRD patterns of Figure 3-5 present well the structural evolution of $ZnS(en)_{0.5}$ nanoplates with the increase of the hydrolysis time. The respective diffraction patterns of ZE nanostructures fabricated by the hydrolysis of $ZnS(en)_{0.5}$ for 0 and 2 h coincide well with the reported structure of orthorhombic $ZnS(en)_{0.5}$.[4,8,15,39] The diffraction pattern of ZE3 nanostructures accords almost with the standard structure of hexagonal wurtzite ZnS (JCPDS no.36-1450) although it still contains some impurity peaks. Meanwhile, the respective diffraction patterns of ZE4 and ZE5 clearly display the wurtzite ZnS structure without showing any impurity peaks, demonstrating that orthorhombic $ZnS(en)_{0.5}$ nanoplates have been converted completely into wurtzite ZnS nanostructures *via* hydrothermal treatment at 120 °C for ≥4 h.[14,15,17,18] In addition, with the increase of the reaction time until 4 h, the peak intensity of the ZnS (002) planes increases gradually owing to the improvement of crystallinity by the thermal annealing effect.[3,12] In contrast, above the treatment time of 4 h, the peak intensity decreases with the time because ZE nanostructures collapse gradually into smaller nanoparticles. The diffraction peaks of ZE

nanostructures become broader with the increase of the hydrolysis time. The average crystallite sizes of ZE nanostructures calculated from the (110) peak widths *via* employing the Scherrer's equation have been presented in Table 3-1. Whereas average crystallite size of $ZnS(en)_{0.5}$ nanoplates is 32.6 nm, that of ZE4 nanostructures is as small as 11.0 nm.[4,13] This also supports the above described structural evolution during the hydrothermal conversion of $ZnS(en)_{0.5}$ nanoplates into barbell-shaped porous ZnS nanostructures.

In order to confirm the amount of ethylenediamine molecules in ZE nanostructures, FTIR spectra have been measured (Figure 3-6). The symmetric and the asymmetric stretching vibrations of $–NH_2$ peaks (3116 and 3236 cm^{-1}, respectively), as well as the scissoring and the wagging vibrations of $–NH_2$ peaks (1600 and 1030 cm^{-1}, respectively), have been found to decrease progressively as the hydrothermal treatment time proceeds; the FTIR spectrum of ZE4 nanostructures do not show any peaks attributable to ethylenediamine molecules.[8,14,43] Thus, the FTIR spectra of Figure 3-6 also support that $ZnS(en)_{0.5}$ nanoplates transform completely into ZnS nanostructures in the hydrolysis time of 4 h. Furthermore, TGA curves of Figure 3-6b describe well that the weight loss at 300-500 °C is owing to the thermal decomposition of ethylenediamine molecules from ZE nanostructures. Thus, the TGA curves of Figure 3-6b also confirm that the hydrolysis of $ZnS(en)_{0.5}$ nanostructures for 4 h produces chemically well-defined ZnS nanostructures. It is noteworthy that the weight loss of 22.9% in the temperature range of 300-500 °C in ZE0 nanostructures is very similar to the theoretically calculated percentage (23.6%) of ethylenediamine in $ZnS(en)_{0.5}$.[5,8] Overall, all the outcomes of Figure 3-6 agree well with the results discussed with the TEM images of Figure 3-2 and the HRXRD patterns of

Figure 3-5, demonstrating that orthorhombic $ZnS(en)_{0.5}$ nanoplates transform completely into wurtzite ZnS nanostructures as the reaction proceeds at 120 °C for ≥4 h.

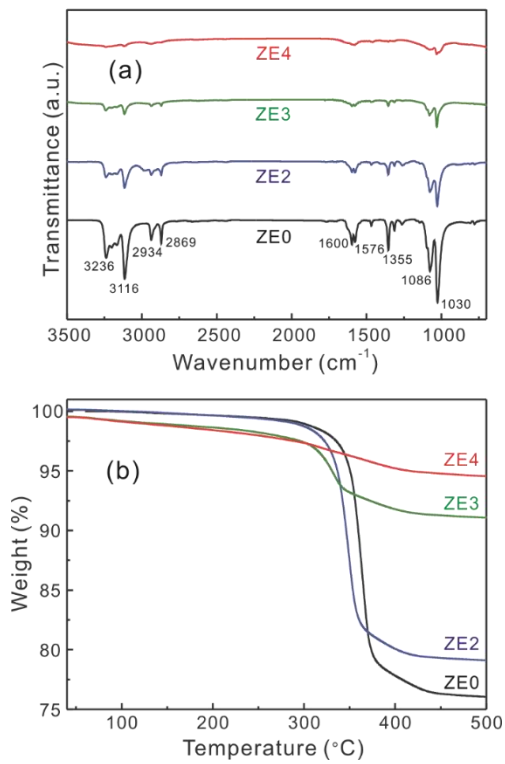

Figure 3-6 FTIR spectra (a) and TGA curves (b) of indicated ZE nanostructures.

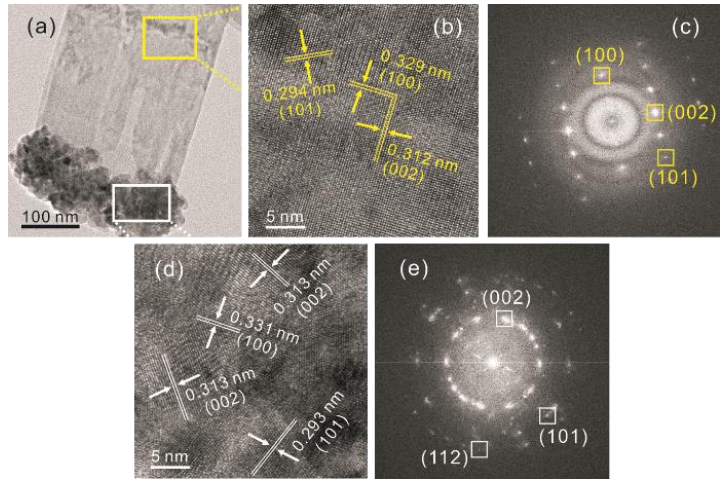

Figure 3-7 HRTEM images (a, b, and d) and FFT patterns (c and e) of a porous ZE4 nanostructures.

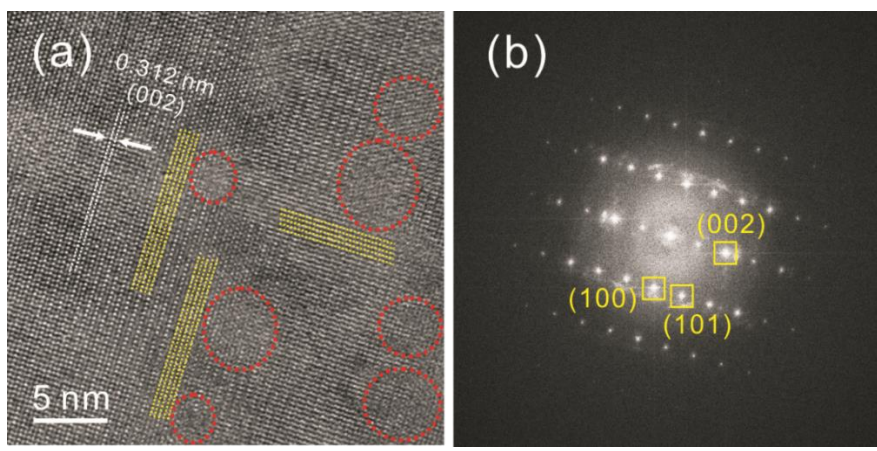

Figure 3-8 HRTEM image (a) and FFT pattern (b) of a porous ZE4 nanostructures. Yellow lines indicate lattice alignments while red circles mark pore regions.

The HRTEM images of Figure 3-7a presents a portion of a barbell-shaped porous and hollow ZnS nanoplate; ZnS nanoparticles are heavily agglomerated at the end facets of a porous ZnS nanostructure. The HRTEM image of Figure 3-7b displays that the lattice

spacings of 0.312 and 0.329 nm in the enlarged selected area of a ZE4 nanostructure match reasonably well with the respective standard spacings 0.313 and 0.331 nm of the (002) and the (100) planes of hexagonal ZnS, revealing that the selected region of the nanostructure possesses a good single-crystalline structure without having any obvious defects such as dislocations or stacking faults in the central region of a ZnS nanostructure.[9,37] The corresponding FFT pattern of Figure 3-7c supports the above-stated defects-free structure because streaky or stretched spots ascribable to defect sites are not observable.[37] Meanwhile, the void domains presented with red marks in Figure 3-8 have been also observed partially in the central region of a ZnS nanostructure. It has been reported that owing to the imbalance of atomic in-and-out diffusion rates during hydrothermal treatment, point defects such as sulfur vacancies exist significantly near planar defects, finally resulting in volume defects of voids to be thermodynamically stable.[13] Furthermore, due to the self-healing process of planar defects during the hydrolysis reaction, planar defects such as stacking faults and twin boundaries eventually vanish to generate highly crystalline ZE4 nanostructures.[13,38] Voids can provide numerous new active edges which can speed up not only mass transfer but also charge migration. High crystallinity is beneficial for fast charge transport by shortening the migration length of charge carriers to surface-adsorbed reactants and surface defects to induce the photocatalytic reaction.[44-46] However, the enlarged HRTEM image of Figure 3-7d designates that small ZnS nanoparticles are aggregated at an end facet of the ZE4 nanostructure; the lattice spacings of 0.313 and 0.331 nm in Figure 3-7d agree well with the standard spacings of the (002) and the (100) planes of hexagonal ZnS, respectively. Defects or grain boundaries are detected throughout the

HRTEM image of Figure 3-7d, suggesting that lattice deformation resulting from lattice mismatches between orthorhombic $ZnS(en)_{0.5}$ and hexagonal wurtzite ZnS nanostructures has taken place during the hydrolysis process.[13,27,47] The ring FFT pattern of Figure 3-7e observed in a region of aggregated small ZnS nanoparticles also implies that polycrystalline structures having numerous defect sites have been produced *via* the hydrothermal treatment reaction. These defects-induced crystal nanostructures can generate trap sites, which can prevent the recombination of photogenerated charge carriers to transfer charges carriers toward adsorbed dyes, resulting in the increase of photocatalytic performances as well.[3,4,21-23,29,30]

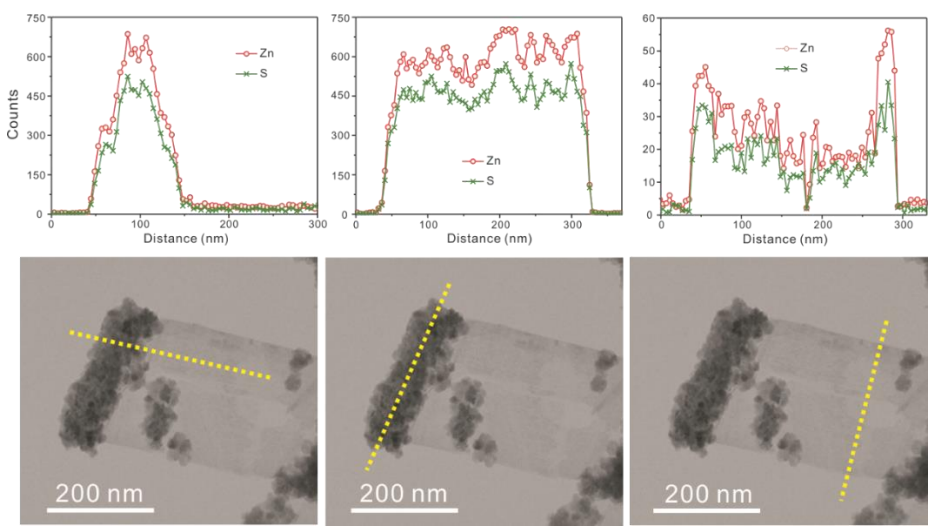

Figure 3-9 EDX elemental profiles (top) scanned along the lines of the STEM images (bottom) of a ZE4 nanostructures.

Line-scanned EDX elemental profiles have been employed to examine the specific compositions and structures of a ZE4 nanostructure. The left profiles and image of Figure

3-9 indicate that the ZnS intensity of the dark region is stronger ~40 times than that of the bright region. This suggests that the ZE4 nanostructure has a barbell shape. Meanwhile, both the central flat and the right parabolic profiles of Figure 3-8 hint that the ZE nanostructure is porous and tubular. Considering Figure 3-9 together with Figure 3-2 and 3-7, we can conclude that the ZE4 nanostructure is a barbell-shaped porous and hollow nanoplate, which has been produced by the removal of ethylenediamine molecules during the hydrolysis process of a $ZnS(en)_{0.5}$ nanoplate. The atomic counts of Zn are quite more than those of S in the ZE4 nanostructure, indicating that sulfur vacancies are rich in the porous and hollow ZE4 nanoplate.

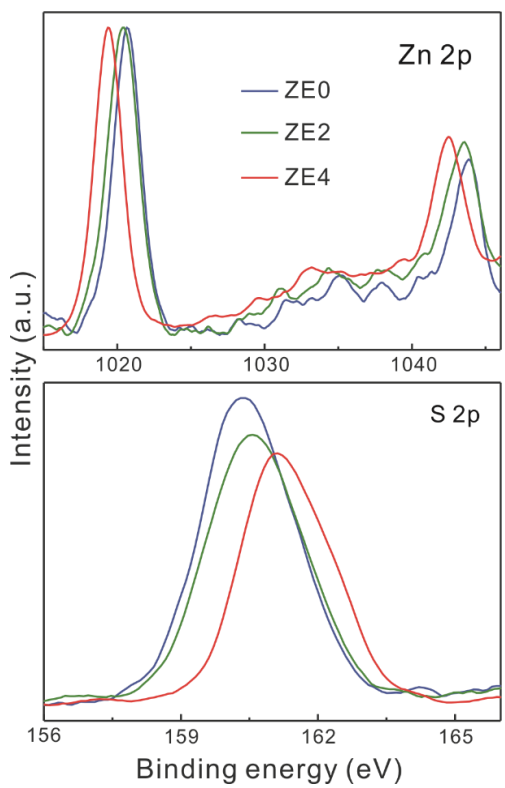

Figure 3-10 XPS spectra of indicated nanostructures

The XPS spectra of ZE samples in Figure 3-10 display that the binding energy (BE) of Zn 2p moves to a lower energy gradually with the hydrolysis time whereas the BE of S 2p shifts to a higher energy. As a result of the hydrothermal treatment of $ZnS(en)_{0.5}$ nanoplates, intercalated ethylenediamine molecules are released from Zn atoms as well as from S atoms. Then, N atoms neighboring to Zn atoms are replaced by S atoms. Because the electronegativity value of S (2.5) is smaller than that of N (3.0),[13] the BE of Zn 2p decreases with the hydrolysis. On the other hand, the BE of S 2p increases because neutral N or C atoms neighboring to S atoms are replaced by Zn^{2+} cations. It is noteworthy that the shift of 110 meV between the Zn 2p BEs of ZE2 and ZE4 is 5.8 times larger than the shift of 19 meV between the Zn 2p BEs of ZE0 and ZE2. It is considered that the small Zn 2p value of ZE4 arises from the generation of S vacancies as well as from the release of N atoms since it is well known that adjacent anion vacancies decrease the BEs of metal ions.[4,22,24] Thus, this supports that defects such as S vacancies are rich in barbell-shaped porous ZnS nanostructures. It can be clearly observed that the peak intensity of S 2p decreases with the hydrolysis time, also indicating that the amount of sulfur vacancies increases with the degree of the hydrothermal treatment.

The EDX results of Figure 3-11 and Table 3-2 indicate well that the atomic ratio of S to Zn decreases gradually as the hydrolysis time increases, implying that the amount of sulfur vacancies increases because sulfur ions diffuse out faster than zinc ions during the hydrothermal process of $ZnS(en)_{0.5}$ nanoplates and because S atoms near crystal defects diffuse faster.[13] It is noteworthy that the atomic percentage of S vacancies is highest (31%) when the hydrolysis is proceeded for 4 h. Interestingly, the relative sulfur atomic ratio of

ZE2 to ZE0, calculated from EDX elemental profiles in Figure 3-11, is 0.88 while the ratio of ZE4 to ZE0 is 0.76. Table 3-2 indicates that these results are almost in accordance with the values obtained from the XPS spectra of Figure 3-10. It has been reported that during the thermal treatment, the formation of sulfur vacancies can take place spontaneously since the formation energy of sulfur vacancies is lower than the formation energies of other vacancies.[48] Considering XPS results, we have already suggested that the generation of sulfur vacancies results from the phase-transformation process of orthorhombic $ZnS(en)_{0.5}$ nanoplates into wurtzite ZnS nanostructures.[27] We suppose that generated sulfur vacancies can be filled with trapped electrons, hydroxide ions, or oxide ions to balance the overall charge of nanostructures.[23]

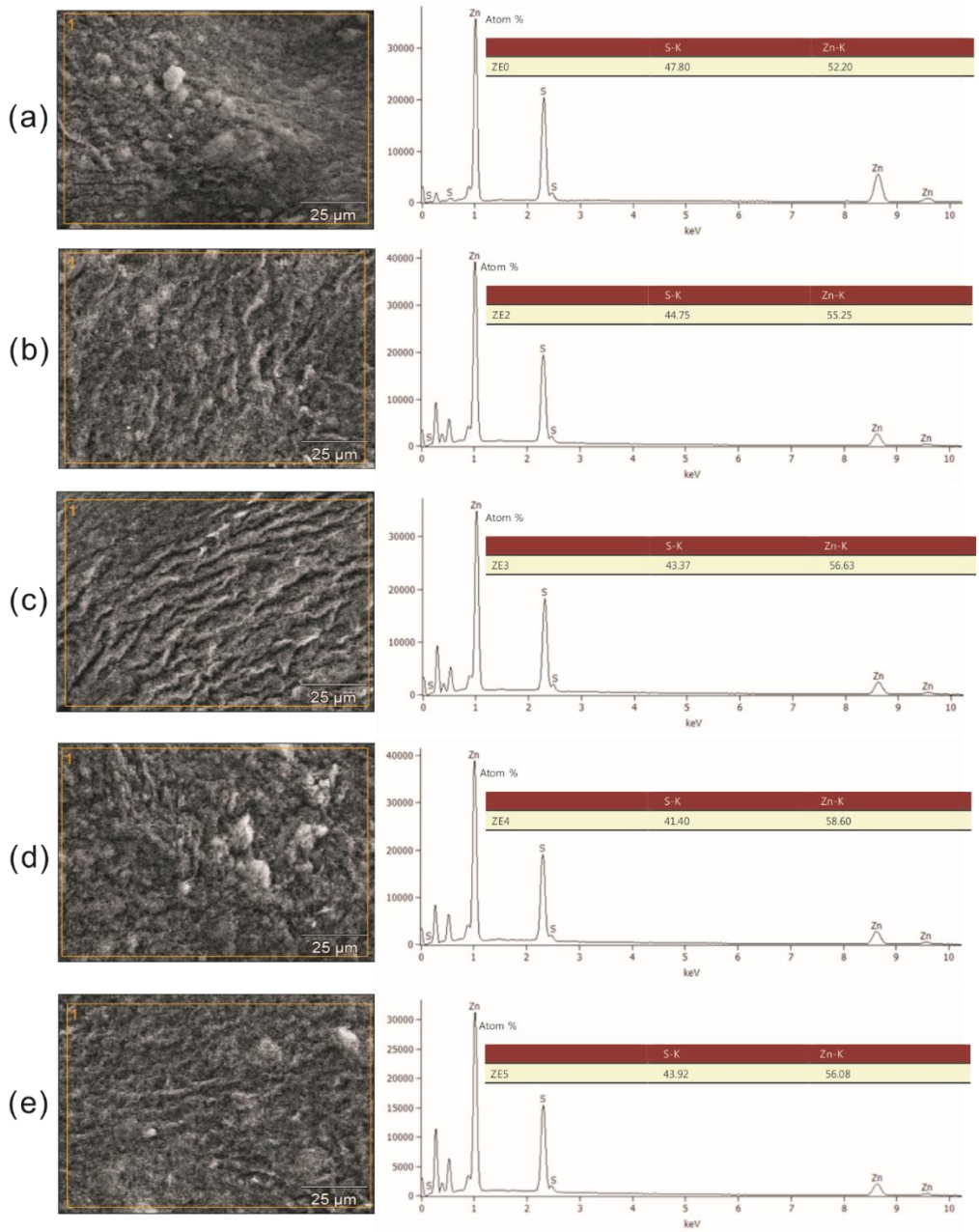

Figure 3-11 Low-magnification SEM images (left) and EDX elemental profiles (right) scanned inside the square lines of the SEM images of ZE0 (a), ZE2 (b), ZE3 (c), ZE4 (d), and ZE5 (e) nanostructures.

Table 3-2

S/Zn atomic ratios in ZE nanostructures, obtained from XPS spectra in Figure 3-10.

Sample	S/Zn atomic ratio
	S
ZE0	1.00
ZE2	0.88
ZE4	0.80

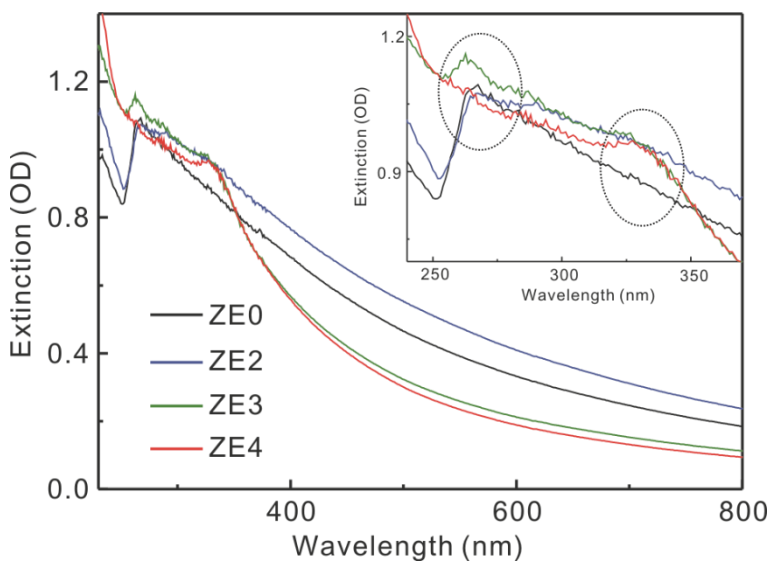

Figure 3-12 Extinction spectra of indicated nanostructures suspended in ethanol.

The UV-vis extinction spectra of ZE nanostructures prepared for different hydrothermal-treatment times have been measured (Figure 3-12). ZE nanostructures fabricated for 0, 2, and 3 h show a distinct extinction peak at 270 nm, which is ascribed to the electronic transition of the hybrid metal-ligand complex having the quantum-confinement effect of

stacked layers. In addition, a long tail is observable extensively in the extinction spectra due to the scattering of nanoplates containing ethylenediamine molecules.[5,17,18] Meanwhile, as the ethylenediamine molecules are released from $ZnS(en)_{0.5}$ nanoplates, ZE2, ZE3, and ZE4 nanostructures exhibit a new extinction peak at 328 nm, which is in accordance with the band-gap peak of bulk wurtzite ZnS.[20,39] Furthermore, the 270 nm peak is absent and the long tail is weak for ZE4 nanostructures, revealing that the ethylenediamine molecules of precursor $ZnS(en)_{0.5}$ nanoplates have been removed completely and that orthorhombic $ZnS(en)_{0.5}$ nanoplates have been transformed certainly into wurtzite ZnS nanostructures.

3.4.2. Photocatalytic activities

The photocatalytic performances of ZE nanostructures have been estimated by monitoring the absorbance changes of RhB as a function of time. The photocatalytic activities of no nanocatalysts and commercial ZnS have been also evaluated under the same circumstances for comparison. Figure 3-13 displays that the absorption of RhB at 554 nm decreases progressively with the increase of the light-irradiation time, revealing that the photocatalytic degradation of RhB takes place. In addition, the absorption maximum shifts to the blue as well, implying that the photodecomposition of RhB occurs *via* competitive processes. The one process is the destruction of the conjugated chromophore, reducing absorption at 554 nm, and the other one is the stepwise N-deethylation reaction, removing the N-ethyl groups gradually from RhB.[9,54]

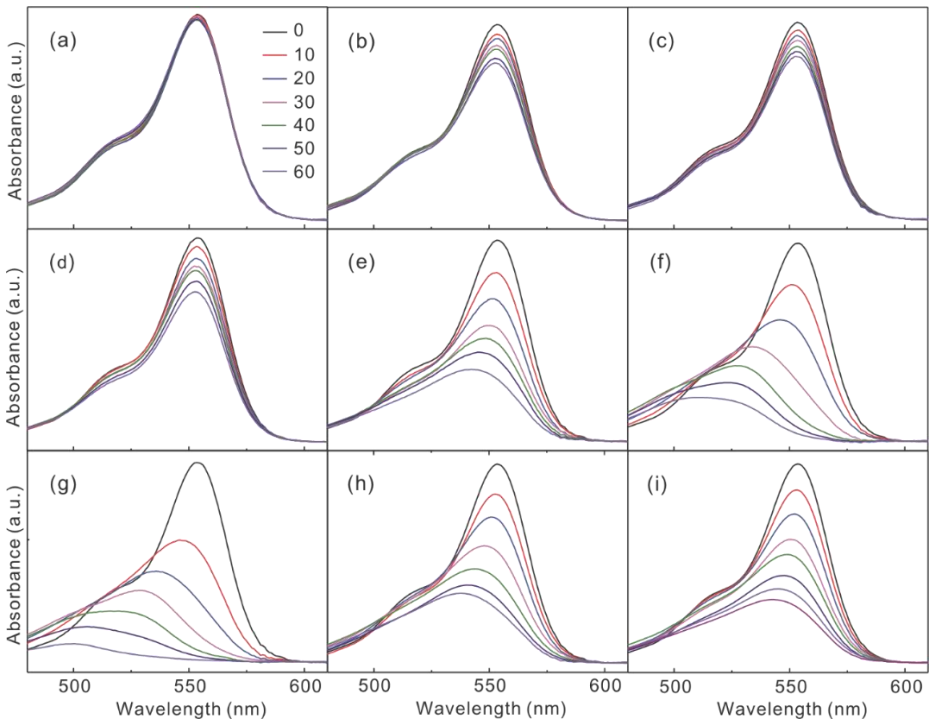

Figure 3-13 Absorption spectra of RhB solutions in the presence of light without nanocatalysts (a), with commercial ZnS (b), and with nanocatalysts of ZE0 (c), ZE1 (d), ZE2 (e), ZE3 (f), ZE4 (g), ZE5 (h), and ZE6 (i), measured at elapsed times indicated in the units of min.

As presented in Figure 3-14 and Table 3-3, the photocatalytic activity of ZE4 nanostructures has been found to be considerably higher than that of any other ZE nanostructures. The activity of ZE4 nanostructures is 11 times higher than that of $ZnS(en)_{0.5}$ nanoplates and even 8.2 times larger than that of commercial ZnS. Please note that the TEM images of commercial ZnS are also presented in Figure 3-15. The kinetic constants have been obtained by plotting pseudo-first-order kinetic profiles of $\ln (A/A_0) = -k\,t$, where t is the time and k is the photocatalytic rate constant.[3] Figure 3-14b shows that

the photocatalytic efficiency of ZE nanostructures increases with the hydrolysis time until the time reaches 4 h. The hydrothermal treatment releases the ethylenediamine molecules of precursor $ZnS(en)_{0.5}$ nanoplates to increase the surface areas, pore volumes, and surface defects of ZE nanostructures, enhancing their photocatalytic activity. The low photocatalytic activity of ZE nanostructures having ethylenediamine molecules is in accordance with a previous result;[8] the number of available photoexcitation charge carriers is smaller in $ZnS(en)_{0.5}$ nanoplates than in ZnS nanostructures without having ethylenediamine molecules since the absorption edge is blue-shifted largely by the quantum confinement effect of the layered organic-inorganic nanostructures.[5,15] Meanwhile, as the hydrolysis time increases over 4 h, their photocatalytic activity rather diminishes because the structures and morphologies collapse to aggregate ZnS nanoparticles, reducing the defects, surface areas, and pore volumes of ZE nanostructures.

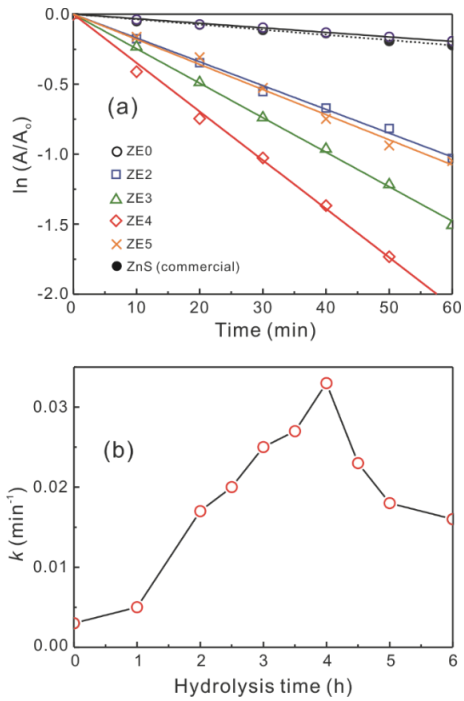

Figure 3-14 First-order decay profiles (a) and degradation rate constants (b) of RhB *via* ZE nanostructures.

Table 3-3

Photocatalytic rate constants, BET surfaces areas, average pore sizes, and total pore volumes of ZE nanostructures.

Sample	k (min^{-1})	BET surface area (m^2/g)	Average pore size (nm)	Total pore volume (cm^3/g)
ZE0	0.003	17.0	34.2	0.08
ZE2	0.017	34.4	33.2	0.26
ZE4	0.033	73.1	31.4	0.41
ZE6	0.016	49.8	30.2	0.22
Commercial ZnS[a]	0.004			
No catalysts	0.001			

[a] The rate constants *via* commercial TiO_2 and SnO_2 are 0.080 and 0.020 min^{-1}, respectively.

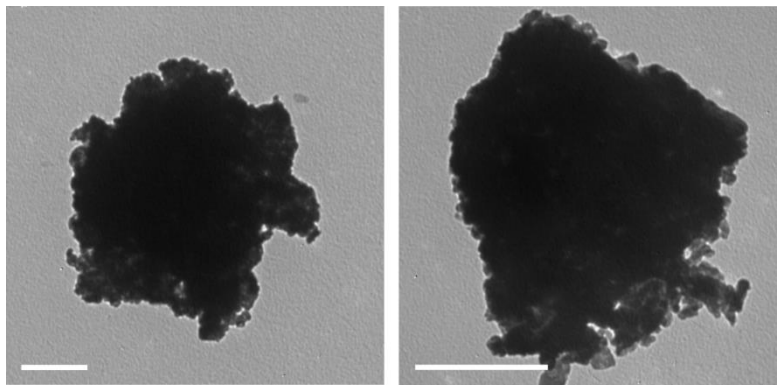

Figure 3-15 TEM images of commercial ZnS. Each scale bar represents 500 nm.

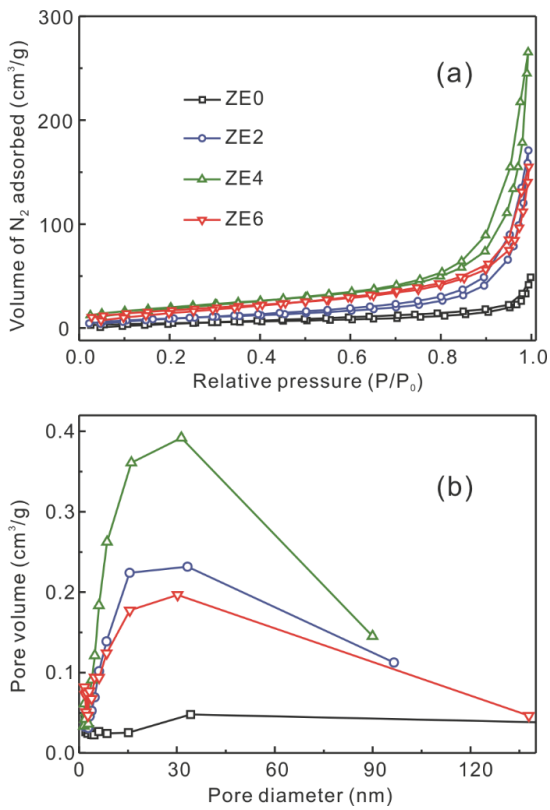

Figure 3-16 N_2 adsorption-desorption isotherms (a) and pore-size distributions (b) of indicated ZE nanostructures.

In general, the high photocatalytic performances of nanocatalysts can be associated with high surface areas, large pore volumes, and porous structures, which provide active sites for photocatalytic reactions.[1-5,41] Thus, we have examined nitrogen adsorption-desorption isotherms and the corresponding results are shown in Figure 3-16. Our obtained ZE nanostructures display type-IV isotherms involving type-H3 hysteresis loops in accordance with the IUPAC classification, suggesting that as-prepared ZE nanostructures are mesoporous.[9,10] The Brunauer–Emmett–Teller (BET) surface areas, pore sizes, and total pore volumes of ZE nanostructures are listed in Table 3-3. The surface areas and total pore volumes of ZE4 nanostructures are higher than the respective ones of any other ZE nanostructures, offering a larger dye-adsorption capacity and a greater charge-production ability to ZE4 nanostructures. Overall, we consider that large surface areas and high pore volumes are important as well for the high photocatalytic efficiency of ZE nanostructures.

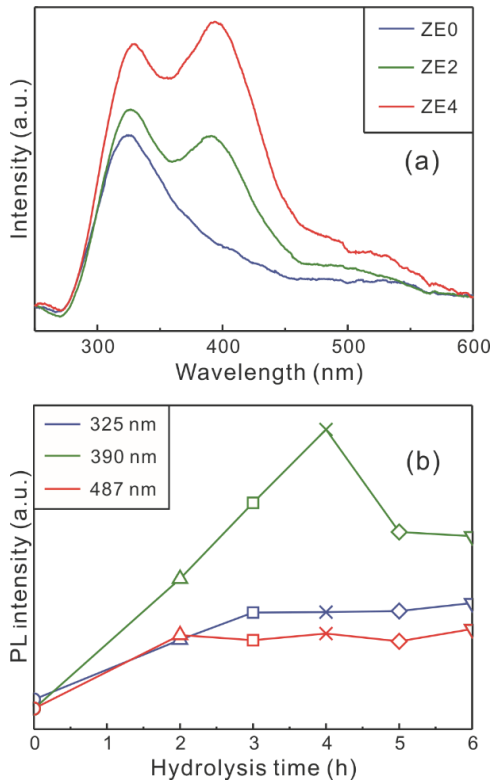

Figure 3-17 PL spectra of indicated ZE-nanostructures in ethanol (a) and relative intensity of PL at indicated wavelengths (b). Excitation: 266 nm pulse laser.

PL spectra can be utilized not only to investigate the recombination, transfer, and separation of photogenerated charge carriers but also to detect surface defects such as ion vacancies and interstitials.[2,3,20-23] Figure 3-17a reveals that the PL of ZE nanostructures increases and shifts to the red with the hydrolysis time, supporting well that ethylenediamine molecules intercalated in ZnS layers are released steadily to transform into hexagonal ZnS nanostructures.[13,19,38] Each PL spectrum of ZE nanostructures can be deconvoluted into three Gaussian curves (Figure 3-18); the UV band at 320-330 nm is attributed to band-edge or excitonic emission; the central band at 390-400 nm is ascribed

to sulfur vacancies or interstitial sulfur-lattice defects; the visible band at 480-490 nm is referred to zinc vacancies.[9,19,49,50]

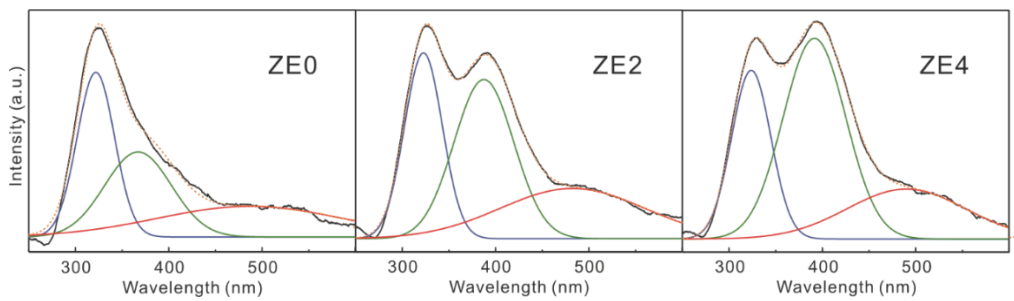

Figure 3-18 PL spectra of indicated ZE nanostructures (black). The samples were suspended in ethanol and excited with 266 nm laser pulses of 6 ns. Blue, green and red lines are deconvoluted Gaussian curves while dotted orange lines correspond to the sum of fitted Gaussian curves.

Figure 3-17b shows that whereas the UV emission at 325 nm and the visible emission at 487 nm hardly change in intensity, the central emission peak at 390 nm arising from sulfur vacancies and interstitial defects grows substantially with the hydrothermal treatment time for 4 h, signifying that the PL intensity at 390 nm of ZE nanostructures is related to the density of surface defects. Furthermore, we have already described that the hydrothermal time determines the extent of phase transformation from $ZnS(en)_{0.5}$ nanoplates into ZnS nanostructures; during the phase transformation, the amount of sulfur vacancies increases progressively.[23,27] Sulfur vacancies are richest in ZE4 nanostructures so that the photocatalytic efficiency of ZE4 nanostructures is significantly higher than that of any other nanocatalysts because photogenerated charge carriers can be readily separated

on surface defects.[3-5,21-23,30] Meanwhile, when the hydrolysis proceeds over 4 h, the PL intensity of ZE nanostructures rather decreases with the reaction time because the morphologies and structures of ZnS nanostructures collapse so that ZnS nanoparticles are heavily agglomerated. The rupture of ZnS nanoplates and the subsequent aggregation of ZnS nanoparticles reduce the surface energy, leading to the depletion of surface defects. Overall, considering Figure 3-17, we can suggest logically that the highest photocatalytic efficiency of ZE4 nanostructures is mainly attributed to the richest presence of sulfur vacancies because the recombination of photogenerated charge carriers can be drastically reduced on the defects.[21-23,30]

We have detected reactive species, such as ·OH, $\cdot O_2^-$, and h^+, involved in the photocatalytic process of RhB *via* ZE4 nanostructures to understand the photocatalytic mechanism; IPA, BQ, and AO were employed to serve as the scavengers of ·OH, $\cdot O_2^-$, and h^+, respectively, in the reaction process.[51,52]

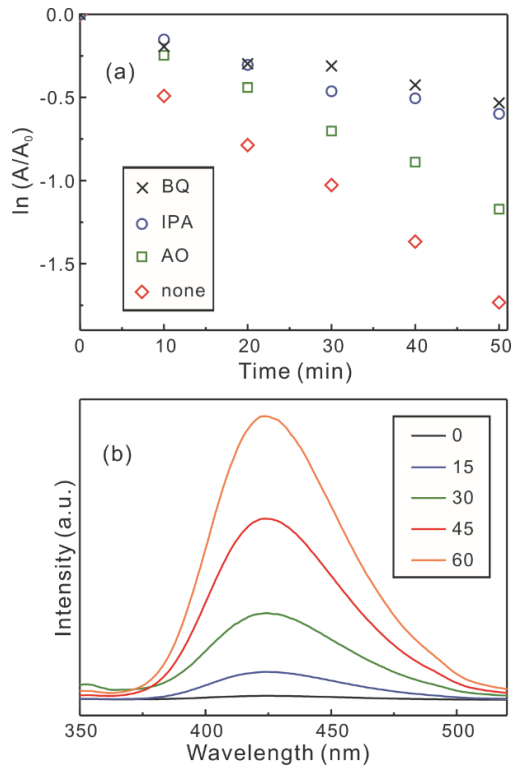

Figure 3-19 First-order decay profiles of RhB photocatalyzed *via* ZE4 nanostructures in the presence of indicated scavengers (a). PL spectra of TAOH generated by light irradiation in the presence of ZE4 nanostructures indicated in the units of min (b).

As shown in Figure 3-19, the photocatalytic efficiency of ZE4 nanostructures decreases substantially with the addition of 1.0 mL IPA (·OH scavenger) or 30 μmol BQ ($\cdot O_2^-$ scavenger) into a reaction mixture solution but slightly with the addition of 30 μmol AO (h^+ scavenger), manifesting that both $\cdot O_2^-$ and ·OH act as main reactive species for the photodegradation of RhB. To further investigate the production of ·OH species involved in the photocatalytic reaction, the time-dependent PL spectra of TAOH molecules have been measured; probe TA molecules react with photogenerated ·OH radicals to produce

TAOH molecules.[9,53] Figure 3-19b shows that the PL intensity of TAOH increases progressively with the increase of the irradiation time, revealing that ·OH radicals are generated during the photodegradation of RhB.

Considering the above presented results, the photocatalytic degradation mechanism of RhB over ZE nanostructures has been schematically illustrated in Figure 3-1. The photogeneration of electrons and holes takes place on the surfaces of ZnS nanostructures under light irradiation. Surface defects such as sulfur vacancies can trap photogenerated electrons to block the recombination of charges, providing more opportunities for electrons and holes to participate in the redox reaction occurring on the surfaces of ZE nanostructures. Electrons trapped in surface defects react with O_2 to produce superoxide radicals ($\cdot O_2^-$) while holes in the valence band of ZnS nanostructures react with OH^- to generate hydroxyl radicals (·OH). Thus, RhB molecules are mainly decomposed by $\cdot O_2^-$ and ·OH.[22,23,52] Meanwhile, holes can play a secondary role to assist the decomposition of RhB because they can also directly oxidize RhB molecules adsorbed to the surfaces of ZnS nanostructures.[9,52] Thus, we suggest that the presence of surface defects plays a key role in the photocatalytic efficiency of ZnS nanostructures.

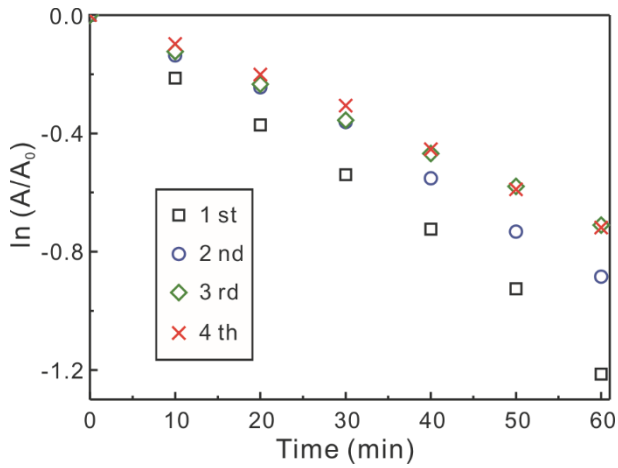

Figure 3-20 Stability test of ZE4 nanostructures *via* reported photocatalytic RhB-degradation experiments.

In order to investigate the photostability of ZE4 nanostructures, reusability tests have been conducted (Figure 3-20). As the recycling proceeds repeatedly, the photocatalytic efficiency diminishes somewhat, implying that side effects such as the photocorrosion of ZnS nanostructures take place during the photocatalytic reaction. Thus, we consider that problems such as ZnS photocorrosion should be resolved for ZE nanostructures to be applied for the treatment of industrial waste water.

3.5. Conclusion

Barbell-shaped porous and hollow ZnS nanoplates have been fabricated facilely *via* hydrothermally treating $ZnS(en)_{0.5}$ nanoplates as sacrificial templates. The amount of S vacancies as well as the morphologies of ZnS nanostructures has been controlled by adjusting the hydrothermal time because ethylenediamine molecules intercalated in ZnS layers are released during the hydrolysis reaction. The layered structure of $ZnS(en)_{0.5}$ nanoplates decomposes to reconstruct surfaces during the high-temperature treatment process, yielding discrete ZnS nanoparticles at two end facets of template nanoplates to produce barbell-shaped porous and hollow ZnS nanoplates finally. The photocatalytic efficiency of porous ZnS nanostructures prepared by hydrothermal treatment for 4 h has been found to be 8.2 times higher than that of commercial ZnS due to abundant sulfur vacancies, high surface areas, and large pore volumes. In particular, the tendency of emission intensity at 390 nm, arising from the sulfur vacancies of ZnS nanostructures, with the increase of the treatment time is in accordance with the trend of photocatalytic activity, suggesting that the high photocatalytic efficiency of ZnS nanostructures results mainly from the increased amount of sulfur vacancies.

3.6. Acknowledgements

This work was financially supported by the National Research Foundation of Korea (research grants: 2015-051798 and 2017-006153).

3.7. References

[1] H. Liang, L. Li, F. Meng, L. Dang, J. Zhuo, A. Forticaux, Z. Wang, S. Jin, *Chem. Mater.*, **2015**, 27, 5702.

[2] X. Li, B. Wei, J. Wang, X. Li, H. Zhai, J. Yang, *J. Alloys Compd.*, **2016**, 689, 287.

[3] D. Liu, Y. Lv, M. Zhang, Y. Liu, Y. Zhu, R. Zong, Y. Zhu, *J. Mater. Chem. A*, **2014**, 2, 15377.

[4] W. Feng, Z. Fang, B. Wang, L. Zhang, Y. Zhang, Y. Yang, M. Huang, S. Weng, P. Liu, *J. Mater. Chem. A*, **2017**, 5, 1387

[5] K. Kole, C. S. Tiwary, P. Kumbhakar, *CrystEngComm*, **2013**, 15, 5515.

[6] H. Ma, K. Teng, Y. Fu, Y. Weng, X. Dong, *Energy Environ. Sci.*, **2011**, 4, 3067.

[7] H. Ma, L. Yue, C. Yu, X. Dong, X. Zhang, M. Xue, X. Zhang, Y. Fu, *J. Mater. Chem.*, **2012**, 22, 23780.

[8] J. S. Jang, C.-J. Yu, S. H. Choi, S. M. Ji, E. S. Kim, J. S. Lee, *J. Catal.*, **2008**, 254, 144.

[9] J. Lee, Y. Kim, J. K. Kim, S. Kim, D.-H. Min, D.-J. Jang, *Appl. Catal. B: Environ.*, **2017**, 205, 433.

[10] Tiwari, S. J. Dhoble, *Cryst. Growth Des.*, **2017**, 17, 381.

[11] G. Zhu, J. Yang, C. Bao, X. Zhang, Z. Ji, S. Wu, X. Shen, *J. Colloid Interface Sci.*, **2016**, 468, 136.

[12] Y. Hong, C. Tian, B. Jiang, A. Wu, Q. Zhang, G. Tian, H. Fu, *J. Mater. Chem. A*, **2013**, 1, 5700.

[13] H.-B. Kim, D.-J. Jang, *Nanoscale*, **2016**, 8, 403.

[14] S. A. Acharya, N. Maheshwari, L. Tatikondewar, A. Kshirsagar, S. K. Kulkarni, *Cryst. Growth Des.*, **2013**, 13, 1369.

[15] L. Nasi, D. Calestani, T. Besagni, P. Ferro, F. Fabbri, F. Licci, R. Mosca, *J. Phys. Chem. C*, **2012**, 116, 6960.

[16] Hernández-Gordillo, E. Maya-Flores, V. Rodríguez-Gonzalez, *Mater. Lett.*, **2015**, 148, 9.

[17] S.-H. Yu, M. Yoshimura, *Adv. Mater.*, **2002**, 14, 296.

[18] S.-H. Yu, J. Yang, Y.-T. Qian, M. Yoshimura, *Chem. Phys. Lett.*, **2002**, 361, 362.

[19] W.-T. Yao, S.-H. Yu, Q.-S. Wu, *Adv. Funct. Mater.*, **2007**, 17, 623.

[20] D. Chen, Z. Wang, T. Ren, H. Ding, W. Yao, R. Zong, Y. Zhu, *J. Phys. Chem. C*, **2014**, 118,

15300.

[21] X. Zhang, J. Qin, Y. Xue, P. Yu, B. Zhang, L. Wang, R. Liu, *Sci. Rep.*, **2014**, 4, 4596.

[22] G. Wang, B. Huang, Z. Li, Z. Lou, Z. Wang, Y. Dai, M.-H. Whangbo, *Sci. Rep.*, **2015**, 5, 8544.

[23] Y.-P. Zhu, J. Li, T.-Y. Ma, Y.-P. Liu, G. Du, Z.-Y. Yuan, *J. Mater. Chem. A*, **2014**, 2, 1093.

[24] Y. Zhao, C. Li, X. Liu, F. Gu, H. L. Du, L. Shi, *Appl. Catal. B: Environ.*, **2008**, 79, 208.

[25] L. Jing, B. Xin, F. Yuan, L. Xue, B. Wang, H. Fu, *J. Phys. Chem. B*, **2006**, 110, 17860.

[26] M. Y. Guo, A. M. C. Ng, F. Liu, A. B. Djurišić, W. K. Chan, H. Su, K. S. Wong, *J. Phys. Chem. C*, **2011**, 115, 11095.

[27] Z. Fang, S. Weng, X. Ye, W. Feng, Z. Zheng, M. Lu, S. Lin, X. Fu, P. Liu, *ACS Appl. Mater. Interfaces*, **2015**, 7, 13915.

[28] N. M. Flores, U. Pal, R. Galeazzi, A. Sandoval, *RSC Adv.*, **2014**, 4, 41099.

[29] H. Yaghoubi, Z. Li, Y. Chen, H. T. Ngo, V. R. Bhethanabotla, B. Joseph, S. Ma, R. Schlaf, A. Takshi, *ACS Catal.*, **2015**, 5, 327.

[30] X. Pan, M.-Q. Yang, X. Fu, N. Zhang, Y.-J. Xu, *Nanoscale*, **2013**, 5, 3601.

[31] X. Xu, L. Hu, N. Gao, S. Liu, S. Wageh, A. Al-Ghamdi, A. Alshahrie, X. Fang, *Adv. Funct. Mater.*, **2015**, 25, 445.

[32] H. Wang, L. Liang, X. Cheng, Y. Luo, S. Sun, *Photochem. Photobiol.*, **2018**, 94, 17.

[33] Z. Ye, L. Kong, F. Chen, Z. Chen, Y. Lin, C. Liu, *Optik*, **2018**, 164, 345.

[34] H. Ma, J. Han, Y. Fu, Y. Song, C. Yu, X. Dong, *Appl. Catal. B: Environ.*, **2011**, 102, 417.

[35] X. Meng, H. Xiao, X. Wen, W. A. Goddard III, S. Li, G. Qin, *Phys. Chem. Chem. Phys.*, **2013**, 15, 9531.

[36] D. Chen, F. Huang, G. Ren, D. Li, M. Zheng, Y. Wang, Z. Lin, *Nanoscale*, **2010**, 2, 2062.

[37] J. Lee, S. Ham, D.-J. Jang, *J. Environ. Chem. Eng.*, **2017**, 5, 4431.

[38] M. Zhang, Y. Lu, J.-F. Chen, T.-K. Zhang, Y.-Y. Liu, Y. Yang, W.-T. Yao, S.-H. Yu, *Langmuir*, **2010**, 26, 12882.

[39] S. Han, W. Liu, K. Sun, X. Zu, *CrystEngComm*, **2016**, 18, 2626.

[40] P. Liu, S. Yu, W. Fan, W. Shi, *Dalton Trans.*, **2013**, 42, 2887.

[41] J.-Y. Dong, C. H. Lin, Y.-J. Hsu, S.-Y. Lu, D. S.-H. Wong, *CrystEngComm*, **2012**, 14, 4732.

[42] Z. Xingfu, H. Zhaolin, F. Yiqun, C. Su, D. Weiping, X. Nanping, *J. Phys. Chem. C*, **2008**,

112, 11722.

[43] L. Zhang, H. Yang, L. Li, R. Zhang, R. Liu, J. Ma, X. Xie, F. Gao, *Inorg. Chem.*, **2008**, 47, 11950.

[44] L. Sheng, T. Liao, L. Kou, Z. Sun, *Materials Today Energy*, **2017**, 3, 32.

[45] M. Xiao, M. Lyu, S. Wang, L. Wang, *Adv. Energy. Mater.*, **2018**, 8, 1701605.

[46] T. Butburee, Y. Bai, H. Wang, H. Chen, Z. Wang, G. Liu, J. Zou, P. Khemthong, G. Q. M. Lu, L. Wang, *Adv. Mater.*, **2018**, 30, 1705666.

[47] F. Huang, J. F. Banfield, *J. Am. Chem. Soc.*, **2005**, 127, 4523.

[48] D. M. Sim, M. Kim, S. Yim, M.-J. Choi, J. Choi, S. Yoo, Y. S. Jung, *ACS Nano*, **2015**, 9, 12115.

[49] K. Sooklal, B. S. Cullum, S. M. Angel, C. J. Murphy, *J. Phys. Chem.*, **1996**, 100, 4551.

[50] W.-H. Zhang, J.-L. Shi, H.-R. Chen, Z.-L. Hua, D.-S. Yan, *Chem. Mater.*, **2001**, 13, 648.

[51] M.-Q. Yang, C. Han, N. Zhang, Y.-J. Xu, *Nanoscale*, **2015**, 7, 18062.

[52] S. Ham, D.-J. Jang, *J. Environ. Chem. Eng.*, **2018**, 6, 228.

[53] H. Lee, T.-H. Park, D.-J. Jang, *New J. Chem.*, 2016, 40, 8737.

[54] K. Yu, S. Yang, H. He, C. Sun, C. Gu, Y. Ju, *J. Phys. Chem. A*, 2009, 113, 10024.

Chapter 4. Photodeposition of Gold Nanoparticles on ZnS Nanobelts for Enhanced Dye Decomposition†

† This is reproduced from Sooho Ham, Dayeon Choi, and Du-Jeon Jang, Mater. Res. Bull., **2019,** 116, 32-39. ⓒ 2019 Elsevier Inc.

4.1. Abstract

Gold nanoparticles have been produced on the surfaces of ZnS nanobelts via direct reduction during a photodeposition process. Because the gold nanoparticles have been fabricated in the absence of any reducing agents or surfactants, charge-separating junctions between gold and ZnS have been effectively produced. As the wt% of surface-decorating gold nanoparticles increases, the photoexcited charges of ZnS nanobelts can be separated efficiently. This has been demonstrated by monitoring photoluminescence spectra and kinetics. The long-lived excited charges promote the generation of reactive radical species, increasing the photocatalytic degradation of 4-nitrophenol. Compared with commercial ZnS, the optimized photocatalyst of Au-ZnS nanobelts exhibits 5.2 times higher photocatalytic activity. Overall, via a simple and facile photodeposition process, charge separating junctions between gold and ZnS have been formed effectively to increase the photocatalytic efficiency of ZnS greatly, suggesting that the photodeposition of gold is an effective method to enhnace photocatalytic dye deomposition activity.

4.2. Introduction

Catalysts are substances that accelerate chemical reactions like organic reactions.[1,2] Among them, photocatalysts are specific catalysts that accelerate reactions using energies from light.[3-5] Although other kinds of catalysts such as electrocatalysts display high catalytic activity, those catalysts essentially need energy sources like batteries.[6] Meanwhile, because photocatalysts are activated by light irradiation, additional energies except light are not necessary to accelerate reactions.[3,5] Also, with the usage of diverse semiconductors having various structures, the design of photocatalysts with optimized structures and energy levels is possible.[3-5] Furthermore, photocatalysts do not emit any byproducts that are harmful to the environment and health. Thus, photocatalysts have been widely studied by many research groups.[7-11] However, there are still problems such as heavy-metal leakage, low recyclability, low photocatalytic activity, and high fabrication cost.

Because organic pollutants in water have increased health and environmental problems, the photocatalytic decomposition of organic compounds has earned intensive attention.[12-16] Among harmful organic pollutants, 4-nitrophenol (4NP), one of phenol derivatives, is the most common organic pollutant in water. Although advanced oxidation processes including photo-Fenton reactions could degrade 4NP effectively, these reactions cause secondary byproducts by chemicals used additionally during oxidation processes.[17] Through photocatalytic reactions, organic compounds could be degraded by excited charges or reactive species produced by excited charges without generating secondary byproducts. Thus, the development of effective photocatalysts to eliminate 4NP through

eco-friendly manners has gained extensive interest.[18]

ZnS, consisted of Zn^{2+} and S^{2-} ions, has been widely applied to various fields.[19-25] Also, because of the low solubility product (K_{sp}) of ZnS (1.6×10^{-24}),[26] ZnS is more stable in aqueous solutions than other chalcogenides. Because ZnS is a direct band-gap semiconductor, the generation of excited electrons and holes is very effective.[27-29] These natures of ZnS are advantageous for ZnS to be used as a photocatalyst.[30-33] Thus, ZnS has been investigated extensively and our group has also synthesized 1D ZnS nanobelts with a facile hydrothermal method.[27] However, ZnS photocatalysts have suffered from the rapid recombination of excited charges, UV-only light absorption due to a large band gap (3.7 eV), and photocorrosion problems.

To solve these problems and enhance the photocatalytic activity of ZnS, many researchers have treated surfaces and formed heterojunctions.[10,11,34] Especially, forming heterojunctions and hybrid structures are widely studied methods to enhance the optoelectronic properties like photocatalytic activity by separating excited charges.[35-39] Usually, ZnS forms heterojunctions with other semiconductors such as CdS, SnO_2, and ZnO or noble metals such as Pt, Au, and Ag.[10,40-46] Particularly, gold forms junctions with ZnS, effectively separating excited charges and inducing visible-light response by the surface plasmon resonance (SPR) of gold nanoparticles. Thus, a variety of Au-ZnS junction structures have been applied to diverse fields such as photocatalysts and SERS supporters.[43-46] To enhance the activity of Au-ZnS junction structures, junction areas between gold and ZnS should be maximized. In general, junctions between gold and ZnS have been formed by using thermal reduction, reducing agents, and coprecipitation. These

methods can effectively reduce gold precursors and form gold nanoparticles. However, gold nanoparticles are not produced directly on the surfaces of ZnS. As a result, excess gold precursors, which are expensive, are needed to form Au-ZnS junctions sufficiently, leading to the low applicability of Au-ZnS junction structures.

Thus, we have introduced a photodeposition process to reduce gold precursor directly on ZnS nanobelts and to form junction structures between gold nanoparticles and ZnS nanobelts. Photodeposition is a reducing method of metal precursors.[47,48] When semiconductor nanoparticles absorb light, excited electron-hole pairs are generated. The excited electrons then reduce metal ions on the surfaces of semiconductor nanoparticles in the absence of any reducing agents or surfactants. For ZnS, the energy level of excited electrons is highly negative due to the high conduction-band energy. Therefore, gold precursors can be reduced directly on the surfaces of ZnS by a photodeposition process (Figure 4-1a). By using the photodeposition process, we have effectively deposited gold nanoparticles directly on the surfaces of ZnS nanobelts. Charges separated at Au-ZnS junctions have been demonstrated by monitoring photoluminescence spectra and kinetic profiles, and the separated charges promote the generation of reactive radicals, increasing photocatalytic activity (Figure 4-1b). Compared with pristine ZnS nanobelts and commercial ZnS, gold-decorated ZnS nanobelts exhibits 2.1 and 5.2 times higher photocatalytic activity, respectively. We consider that our study provides a new approach to the formation of junction structures with the minimum use of expensive metal precursors.

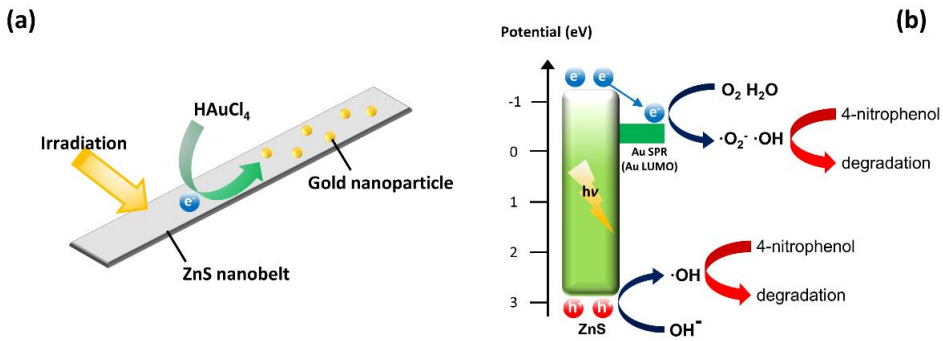

Figure 4-1 Schematics for the gold decoration of a ZnS nanobelts (a) and the photocatalytic decomposition.

4.3. Experimental

4.3.1. Materials

All the chemicals have been purchased from commercial sources and employed without further purification. $HAuCl_4 \cdot 3H_2O$ (≥99.9%), ethylenediamine (en, ≥99%), $ZnCl_2$ (>98%), and ZnS particles (10 μm, 99.99%) have been purchased from Sigma-Aldrich; isopropyl alcohol (IPA, >99.5%), sulfur (>99.0%), ethanol (>99.0%), and sodium sulfite anhydrous (98%) from Daejung Chemicals; $N_2H_4 \cdot H_2O$ (98%), p-benzoquinone (p-BQ, >98%), and 4NP (99%) from Alfa Aesar. Water (>15 MΩ cm) purified with an Elga PURELAB system was employed throughout the experiments.

4.3.2. Fabrication of ZnS nanobelts and Au(R)-ZnS nanobelts

Wurtzite ZnS nanobelts were fabricated through a reported hydrothermal synthetic

process.[10] In a typical process, 2.0 mmol of $ZnCl_2$ was dissolved in a solution containing 7.5 mL of water and 7.5 mL of ethylenediamine while 2.0 mmol of sulfur was dissolved in 15 mL of $N_2H_4 \cdot H_2O$. After 30 min of stirring, the solutions were mixed and transferred to an autoclave whose capacity was 50 mL. Then, the autoclave was maintained in a 180 °C oven for 9 h. As-prepared ZnS nanobelts were rinsed using water and ethanol several times and dried in a 40 °C vacuum oven for 6 h.

Gold nanoparticles-decorated ZnS nanobelts were fabricated via a photodeposition process. 50 mg of as-prepared ZnS nanobelts was suspended in 50 mL water via sonication. The solution was transferred to a quartz vessel. A designated volume of 2.0 mg/mL $HAuCl_4$ in ethanol was added to the solution, which was then maintained under 300 W Xe-lamp irradiation for 30 min. As-synthesized gold nanoparticles-decorated ZnS nanobelts were rinsed with water and ethanol several times immediately after the reaction to eliminate unreacted gold precursors, and dried in a 40 °C vacuum oven for 6 h. Note that when the weight percentage (wt%) of gold is x, gold nanoparticles-decorated ZnS nanobelts fabricated by photodeposition will be designated as Au(x%)-ZnS nanobelts; for example, 0.2 wt% gold nanoparticles-decorated ZnS nanobelts are designated as Au(0.2%)-ZnS nanobelts.

4.3.3. Characterization

Transmission electron microscopy (TEM) images were taken with a Hitachi H-7600 microscope while high resolution TEM (HRTEM) images and fast Fourier transformation

(FFT) patterns were obtained with a JEOL JEM-2100F microscope. X-ray diffraction (XRD) was carried out with a Bruker new D8 advance diffractometer. X-ray photoelectron spectroscopy (XPS) was conducted with a ThermoVG Scientific SIGMA PROBE spectrometer and were calibrated with the C 1s peak at 284.5 eV. Diffuse-reflectance spectroscopy (DRS) was carried out using a StellaNet US/EPP 2000C spectrometer whereas absorption spectra were measured using a Scinco S-3100 spectrophotometer. Photoluminescence (PL) was taken with an Ocean Optics USB2000+ detector after exciting samples with 266 nm laser pulses having a 6 ns duration time from a Q-switched Quantel Brilliant Nd:YAG laser. Photoluminescence decay kinetic profiles were taken by using a 25 ps Nd:YAG laser (Quantel, Pizzicato) and a 10 ps streak camera (Hamamatsu, C2830) connected with a CCD detector (Princeton Instruments, RTE128H).

4.3.4. Photocatalytic properties

Photocatalytic properties of as-formed Au(x%)-ZnS nanobelts were estimated by monitoring the photocatalytic 4NP decomposition. Typically, an 80 mL aqueous solution containing 50 μM 4NP, 3.0 g sodium sulfite, and a 10 mg Au-ZnS photocatalyst was prepared via sonication. The solution was set aside in the dark for 2 h under vigorous magnetic stirring to acheive the adsorption-desorption equilibrium on the surfaces of the photocatalyst. Then, the solution was transffered to a cylindrycal reaction quartz vessel, whose diameter was 8 cm and whose total volume was 150 mL. The solution was irradiated under stirring using a 300 W xenon lamp. A 2.0 mL aliquot was taken at every 10 min and centrifuged at 10000 rpm for 10 min to separate the supernatant from the photocatalyst.

The absorption spectrum of the supernatant was measured to estimate the concentration of remaining 4NP, which was then plotted along the photocatalytic reaction time to calculate the photocatalytic rate constant of the photocatalyst. To investigate reactive species that induces the photocatalytic degradation of 4NP, a widely known scavenger for hydroxyl radicals (IPA) or superoxide radicals (p-BQ) was additionally added into the photocatalytic reaction solution. The stability of a photocatalyst was tested through a recycling test. After the completion of the photocatalytic reaction, the photocatalytst was collected with centrifugation and re-used. The recycling test was conducted following the above mentioned photocatalytic procedure.

4.4. Results and discussion

4.4.1. Structural properties

The structures and morphologies of Au(x%)-ZnS nanobelts have been observed by measuring TEM images (Figure 4-2). During the hydrothermal synthesis of ZnS nanobelts, an ethylenediamine molecule binds with two Zn^{2+} ions to form $Zn{\cdot}(en)_{0.5}^{2+}$, which then binds with S^{2-} to produce $ZnS{\cdot}(en)_{0.5}$. The ethylenediamine molecules then escape from $ZnS{\cdot}(en)_{0.5}$ nanobelts by reacting with water at 180 °C to form solid ZnS nanobelts.[28] Pristine ZnS nanobelts maintain original morphologies and smooth surfaces as presented in Figure 4-2a. After the addition of gold precursors under xenon-lamp irradiation, small gold nanoparticles whose diameters are smaller than 4 nm have been formed on ZnS

nanobelts. As the x% of Au-ZnS composite nanobelts increases, the number, as well as the average diameter, of gold nanoparticles on ZnS nanobelts increases (Figure 4-2b-d), suggesting that the gold precursor of $HAuCl_4$ has been directly reduced by excited electrons on ZnS surfaces.[48] To reduce gold precursors and to form gold nanoparticles on ZnS nanobelts, the gold seeds should be formed on the surfaces of the nanobelts prior to the growth of gold nanoparticles.[55,56] Excited electrons produced from the photoexcitation of ZnS reduce gold ions to form tiny gold seeds on ZnS nanobelts; excited electrons on ZnS nanobelts are transported to surface states of ZnS nanobelts to reduce gold precursor species, forming gold seeds. Surface-decorating gold seeds newly generate energy levels, which are lower than the conduction band of ZnS. Thus, excited electrons at the conduction band of ZnS can be transferred to the energy states of gold, leading to charge separation.[47,49] Thus, excited electrons are collected on the surfaces of gold seeds, causing gold precursor ions to be reduced on the surfaces of the gold seeds and increasing the sizes of gold nanoparticles further.

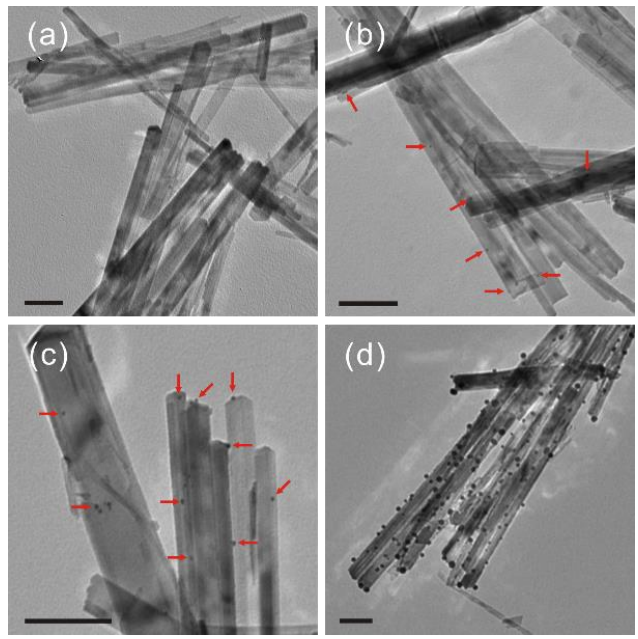

Figure 4-2 TEM images of Au(x%)-ZnS nanobelts whose x values are 0.0 (a), 0.1 (b), 0.2 (c), and 2.0 (d). Red arrows indicate gold nanoparticles, while each scale bar indicates 100 nm.

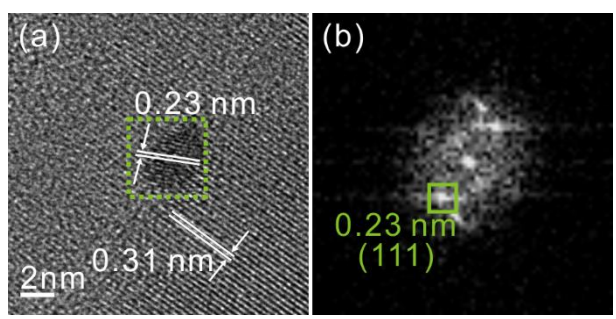

Figure 4-3 HRTEM image of a Au(0.2%)-ZnS nanobelt (a) and FFT pattern of a gold nanoparticles obtained from the green region of the HRTEM image (b).

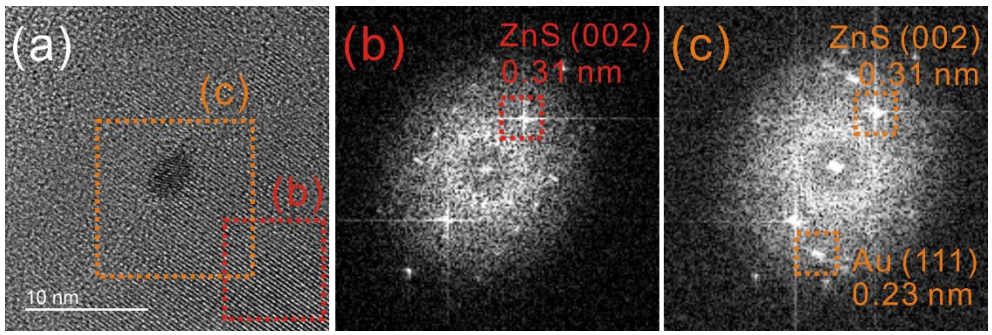

Figure 4-4 HRTEM image of a Au(0.2%)-ZnS nanobelt (a) and FFT patterns of a ZnS nanobelt (b) and a Au-ZnS nanobelt (c) obtained from the red orange regions of the HRTEM image, respectively.

More detailed morphologies and structures of gold nanoparticles-decorated ZnS nanobelts have been investigated by measuring the HRTEM image and the FFT pattern of Figure 4-3. The outer part of the green square in Figure 4-3a represents the HRTEM image of a ZnS nanobelt and displays the lattice spacing of 0.31 nm, which matches very well with the reference lattice spacing of 0.31 nm between the (002) planes of wurtzite ZnS.[10,11] This result reveals that the crystal structure of ZnS nanobelts remains invariant during the photodeposition procedure. The inner part of the green square of Figure 4-3a represents the HRTEM image of a gold nanoparticle formed during photodeposition on the surface of a ZnS nanobelt. Because the atomic number of gold is larger than that of Zn or S, the HRTEM image of a gold nanoparticle is darker than that of ZnS. Furthermore, the lattice spacing value of 0.23 nm agrees well with the standard lattice spacing value of 0.23 nm between the (111) planes of gold.[50] However, the gold nanoparticle is not a single crystal, revealing that our surfactant-free low-temperature photodeposition method is not suitable

for the synthesis of single crystalline nanoparticles. The FFT pattern of the gold nanoparticle described with Figure 4-3a (Figure 4-3b) displays the (111) planes of the gold nanoparticle, matching well with the HRTEM image of the gold nanoparticle. The FFT patterns of a ZnS nanobelt and a Au-ZnS nanobelt are also presented in Figure 4-4. The FFT pattern of a ZnS region exhibits the intense signal from the (002) planes of wurtzite ZnS, while the FFT pattern obtained from a Au-ZnS region represents the signals from both the (002) planes of wurtzite ZnS and the (111) planes of gold. Because a gold nanoparticle is not a single crystal, FFT signals originating from different crystalline regions are also shown.

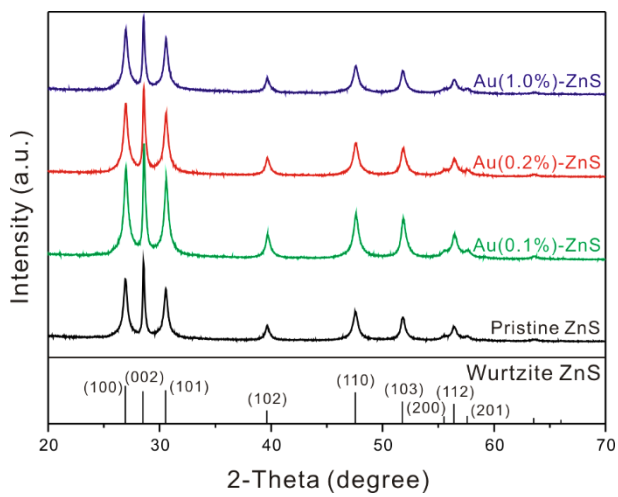

Figure 4-5 XRD patterns of pristine ZnS and Au(x%)-ZnS nanobelts. The standard diffraction pattern of wurtzite ZnS is also presented at the bottom.

The crystallinity of gold nanoparticles-decorated ZnS nanobelts was estimated via XRD analysis (Figure 4-5). The XRD pattern of pristine ZnS nanobelts matches well with the standard diffraction pattern of wurtzite ZnS (JCPDS card no. 36-1450). During the

photodeposition process, ZnS nanobelts have maintained the crystalline structure of wurtzite; diffraction peaks originating from other crystalline structures of ZnS have not been monitored. Furthermore, diffraction peaks from gold nanoparticles have not been monitored, because, as mentioned above, the crystallinity of gold nanoparticles is low and the wt% of gold is very small.

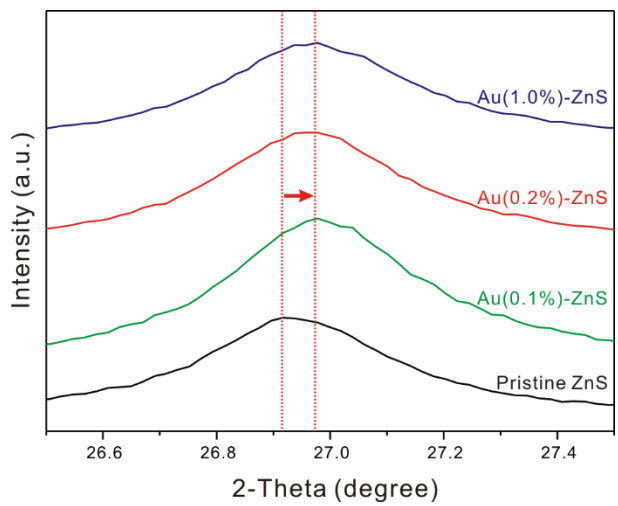

Figure 4-6 Enlarged XRD diffraction patterns of pristine ZnS and Au(x%)-ZnS nanobelts around 2θ of 27 °.

Table 4-1

Average crystallite sizes of pristine ZnS and Au(x%)-ZnS nanobelts calculated by using the Scherrer's equation.

Sample	Crystallite size (nm)
Pristine ZnS	24.7
Au(0.1%)-ZnS	24.2
Au(0.2%)-ZnS	24.1
Au(1.0%)-ZnS	24.0

Enlarged XRD patterns around 2θ of 27° presented in Figure 4-6 indicate that the diffraction peak from the (100) planes of ZnS shifts to a higher value when the surfaces of ZnS are decorated with 0.1% gold nanoparticles, revealing the shrinkage of the lattice spacings of ZnS due to surface decoration by gold nanoparticles.[51] However, as the wt% of gold increases ($x > 0.1$), there is no obvious shift of the XRD peak, suggesting that gold precursors are reduced on gold seeds without being deposited on ZnS. Furthermore, the XRD patterns from other 2θ values have exhibited the same tendency as that from 2θ of 27°, revealing that the gold nanoparticles are formed on the surfaces of ZnS nanobelts regardless of the crystal facets of ZnS nanobelts. The mean crystallite sizes of Au-ZnS nanocomposites in Table 4-1 were calculated applying the Scherrer's equation.[10] Average crystallite sizes have been decreased slightly after photodeposition. The decrement of mean crystallite sizes suggests that the crystalline degree of ZnS nanobelts decreases slightly during photodeposition.

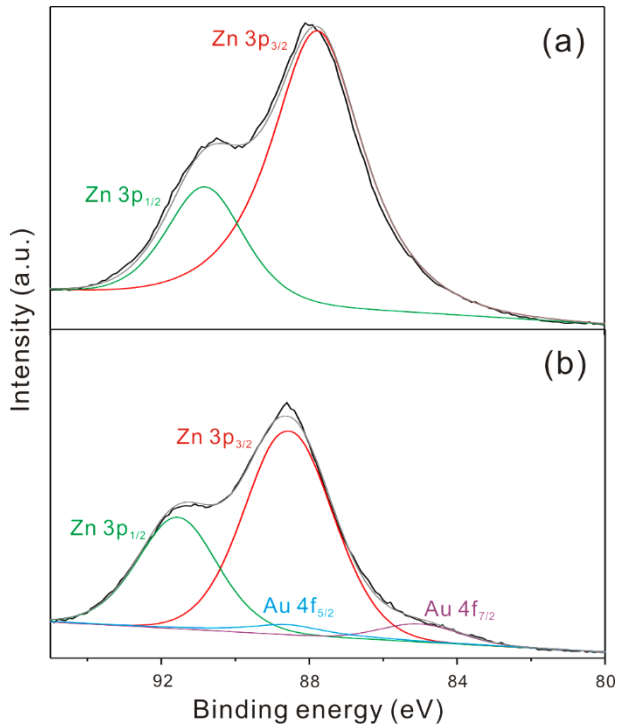

Figure 4-7 XPS spectra of pristine ZnS (a) and Au(0.2%)-ZnS nanobelts (b).

The Au 4f and Zn 3p XPS spectra of pristine ZnS and Au(0.2%)-ZnS nanobelts are displayed in Figure 4-7. The spectrum of pristine ZnS nanobelts in Figure 4-7a has been deconvoluted into two Gaussian bands designated as Zn $3p_{1/2}$ and Zn $3p_{3/2}$, whose binding energies are 90.82 and 87.75 eV, respectively, with no peaks from gold nanoparticles. The XPS spectrum of Au(0.2%)-ZnS nanobelts in Figure 4-7b has been deconvoluted into four Gaussian bands with binding energies of 91.58, 88.59, 88.51, and 84.95 eV, which have been attributed to Zn $3p_{1/2}$, Zn $3p_{3/2}$, Au $4f_{5/2}$, and Au $4f_{7/2}$, respectively. The electron binding energies of Au $4f_{5/2}$ and Au $4f_{7/2}$ agree well with the electron binding energies of small gold nanoparticles,[52,53] demonstrating that ZnS nanobelts have been decorated with

metallic gold nanoparticles through the photodeposition process. However, the estimation of the exact content of gold on ZnS nanobelts was challenging, because the wt% of gold was too low.

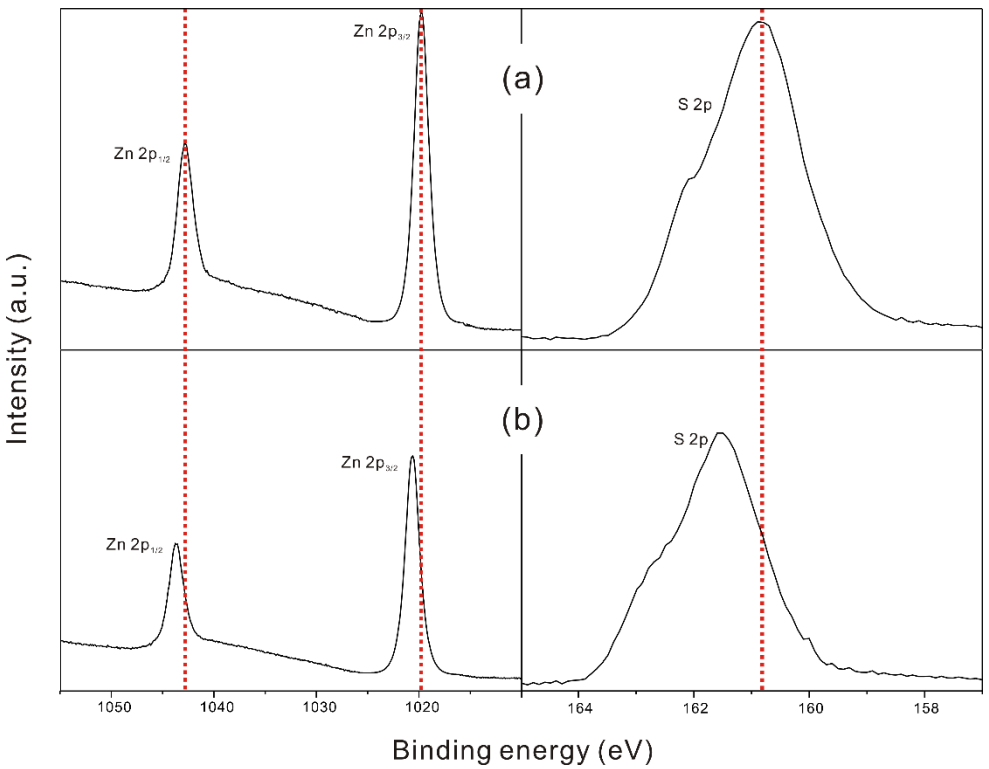

Figure 4-8 Zn 2p (left) and S 2p (right) XPS spectra of pristine ZnS (a) and Au(0.2%)-ZnS nanobelts (b).

The formation of a junction between gold and ZnS has been proved via monitoring the XPS spectra of Zn 2p and S 2p (Figure 4-8). The XPS spectrum of Zn 2p from pristine ZnS nanobelts displays two peaks from Zn $2p_{1/2}$ and Zn $2p_{3/2}$, whose binding energies match well with the respective ones of Zn^{2+}. Also, the S 2p XPS spectrum of pristine ZnS

displays a peak with a shoulder, whose binding energy corresponds to that of S^{2-} ions, revealing that Zn and S form the ionic compound of ZnS (Figure 4-8a).[11] The XPS spectra of Zn 2p and S 2p from Au(0.2%)-ZnS nanobelts presented in Figure 4-8b indicate that the photodeposition of gold has induced the electron binding energy of Zn $2p_{3/2}$ to shift from 1019.7 eV to 1020.7 eV. Because the electronegativity of Zn (1.7) is smaller than that of Au (2.4), the electron densities of both Zn and S have been decreased with the photodeposition of gold nanoparticles. The decreased electron densities have alleviated electron repulsion, leading to the increase of electron binding energies.[10,11] The increase of electron binding energies reveals direct interactions between ZnS and gold, thus proving that gold nanoparticles directly decorate ZnS nanobelts to form junctions between gold and ZnS, which can effectively separate excited charges.

4.4.2. Optical properties

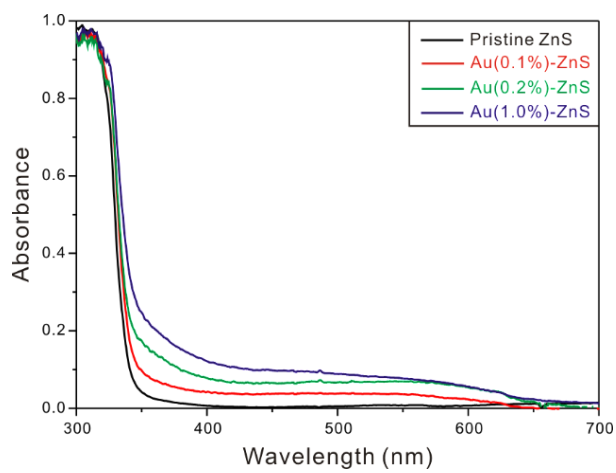

Figure 4-9 DRS spectra of pristine ZnS and Au(x%)-ZnS nanobelts.

UV-vis absorption properties of pristine and Au(x%)-ZnS nanobelts have been estimated by measuring DRS spectra (Figure 4-9). The DRS spectrum of pristine ZnS nanobelts exhibits the characteristic absorption band of ZnS under 340 nm. After the photodeposition of gold, the absorption band below 340 nm is almost the same as that of pristine ZnS nanobelts, implying that ZnS nanobelts maintain typical optical properties during the photodeposition. However, a new visible-light absorption band between 400 and 600 nm increases with the photodeposition of gold nanoparticles. Because gold nanoparticles typically display visible-light absorption around 500 nm, the visible-light response between 400 and 600 nm has been attributed to the SPR of deposited gold nanoparticles. Furthermore, UV absorption between 340 and 400 nm has been increased with the photodeposition, due to absorption from interface junctions between gold and ZnS.

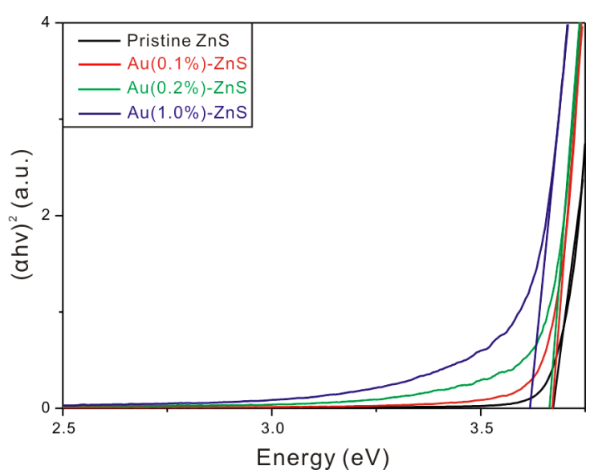

Figure 4-10 Kubelka-Munk plots of pristine ZnS and Au(x%)-ZnS nanobelts. The solid lines show the best linear fits to estimate band-gap energies.

For further investigation, the band gaps of ZnS nanobelts have been calculated by drawing the Kubelka-Munk plots (Figure 4-10).[10] The band-gap energies of Au(x%)-ZnS nanobelts have been estimated as 3.70, 3.69, 3.68, and 3.62 eV for x values of 0.0, 0.1, 0.2, and 1.0, respectively. Absorption increase in the visible-light region regardless of the invariant band-gap energies of ZnS indicates the formation of junctions between gold and ZnS.

The recombination of excited electrons and holes in ZnS has been monitored by measuring photoluminescence spectra (Figure 4-11). Typically, because ZnS is a direct band-gap semiconductor, ZnS exhibits intense photoluminescence in the UV region. Along with the increment of gold wt%, the PL of ZnS nanobelts decreases rapidly; Au(0.1%)-ZnS nanobelts display diminished PL, whose intensity is only a quarter of PL intensity from pristine ZnS nanobelts. As the gold wt% increases, the PL intensity of ZnS nanobelts decreases steadily; when the x value reaches 1.0, the PL intensity is only one sixth of that from pristine ZnS nanobelts. Despite the PL decrease, other peaks from surface defects have not been observed, proving that surface defects have hardly been generated through the photodeposition process. The maximum-normalized band-edge emission spectra of pristine ZnS and Au(x%)-ZnS nanobelts are shown in Figure 4-12. The peak position of PL for Au(x%)-ZnS nanobelts is around 330 nm regardless of gold wt%. However, as gold is decorated on the surfaces of ZnS nanobelts, PL around 340 nm gradually increases. The generation of a new PL band indicates that a new energy level has been formed by the decoration of gold nanoparticles, suggesting that the energy level of gold nanoparticles is slightly lower than the conduction band of ZnS and that excited charges can be separated

by gold nanoparticles. The decrease of PL with the wt% of gold reveals that excited charges can be separated efficiently by gold decoration.[10,11] Because ZnS is a direct band-gap semiconductor, the recombination of excited charges is rapid. Thus, the separation of charges is essential to enhance photocatalytic activity, which is facilitated by excited electrons and holes. Photodeposition has reduced the ionic precursor of gold via photoexcited electrons directly on the surfaces of ZnS to decorate ZnS surfaces with gold nanoparticles. Then, the gold nanoparticles make excited charges be separated effectively at low gold wt%, enhancing the photocatalytic activity of ZnS in the decomposition of 4NP in aqueous solutions (See section 4.3.3).

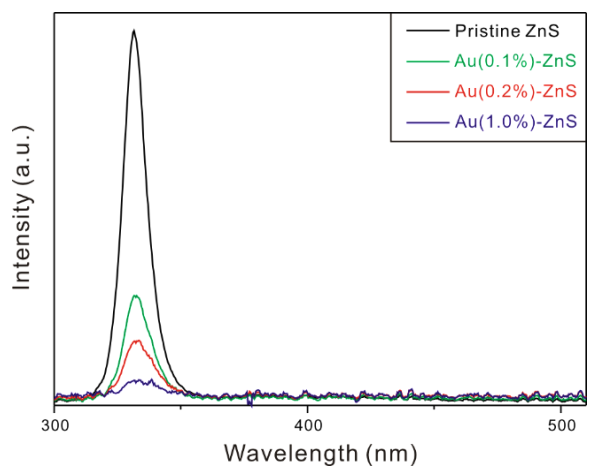

Figure 4-11 PL spectra of pristine ZnS and Au(x%)-ZnS nanobelts. Samples were suspended in ethanol and excited by 266 nm laser pulses.

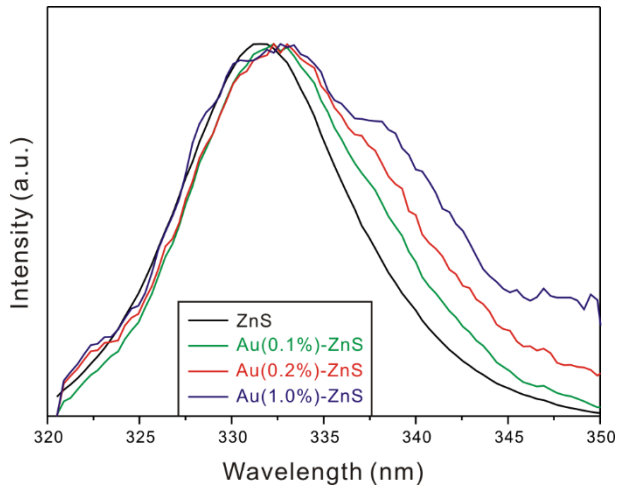

Figure 4-12 Maximum-normalized band-edge emission spectra of pristine ZnS and Au(x%)-ZnS nanobelts.

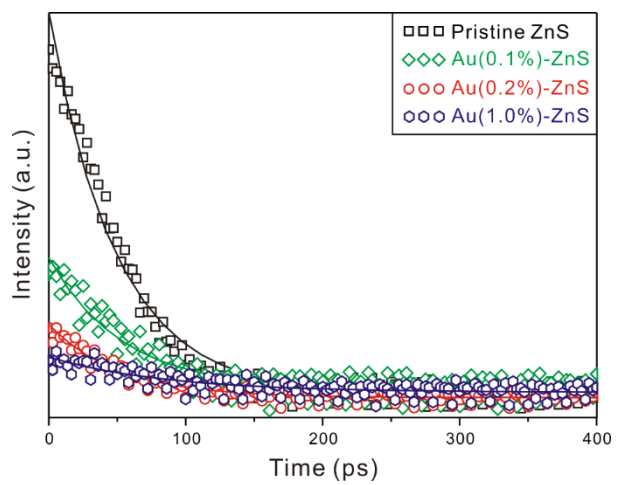

Figure 4-13 PL decay kinetic curves of pristine ZnS nanobelts and Au(x%)-ZnS nanobelts. Solid lines are best-fitted kinetic decay plots. Samples were dispersed in ethanol, excited using 266 nm laser pulses, and monitored at 325 ± 25 nm.

Table 4-2
PL decay kinetic constants of Au(x%)-ZnS nanobelts, extracted from Figure 4-13.

Sample	A_0[a]	Decay time	k_{ET} (10^9 s^{-1})
Pristine ZnS	1.00	35.0 (0.97) + 750.6 (0.03)[b]	-
Au(0.1%)-ZnS	0.41	33.2 (0.93) + 750.6 (0.07)	1.5
Au(0.2%)-ZnS	0.32	31.8 (0.88) + 750.6 (0.12)	2.9
Au(1.0%)-ZnS	0.18	23.8 (0.69) + 750.6 (0.31)	13.4

[a] Relative initial total amplitude.

[b] Initial amplitude fraction of each component.

The more detailed dynamics of excited charges has been studied by monitoring PL decay kinetic profiles (Figure 4-13), and obtained decay kinetic constants have been presented in Table 4-2. The decay profiles of Figure 4-13 reveal that the initial total amplitude of band-edge emission diminishes with the extent of the photodeposition, also supporting that excited charges can be separated efficiently by gold decoration,[10,11,54,57] as discussed with Figure 4-11. Each decay profile has been fitted to a bi-exponential curve. For pristine ZnS nanobelts, the fast decay time of 35.0 ps and the slow decay time of 750.6 ps have been assigned as the intrinsic recombination time of excited charges and the decay time of trapped electrons at the surface states of ZnS nanobelts, respectively.[10] To analyze the recombination dynamics of excited charges in Au(x%)-ZnS nanobelts, only the fast decay component has been considered because the slow decay component is derived from the surface states of ZnS and the fraction of the slow component is small. Because the excited electrons of the conduction band are transferred into surface-decorating gold nanoparticles,

the emission decay time of composite nanobelts becomes shorter than that of pristine nanobelts. Furthermore, the rate constant of electron transfer from the conduction band of ZnS to gold nanoparticles (k_{ET}) has been calculated by using Eq. (1).

$$k_{ET} = [\tau_1(\text{Au(x\%)-ZnS})]^{-1} - [\tau_1(\text{ZnS})]^{-1} \qquad (1)$$

Table 4-2 indicates that the charge transfer rate increases with the wt% of decorating gold nanoparticles, revealing that excited electrons in ZnS nanobelts can be efficiently transferred from ZnS nanobelts to surface-decorating gold nanoparticles. Because the conduction band of ZnS nanobelts is more negative than the energy levels of gold nanoparticles, excited electrons at the conduction band of ZnS can be readily transferred to the energy levels of gold nanoparticles. The formation of interfacial junctions between gold and ZnS has been optimized by reducing gold ions directly on ZnS nanobelts. These optimized junction structures induce charges to be separated effectively at very low wt% of gold, enhancing photocatalytic efficiency (See section 4.4.3).

4.4.3. Photocatalytic properties

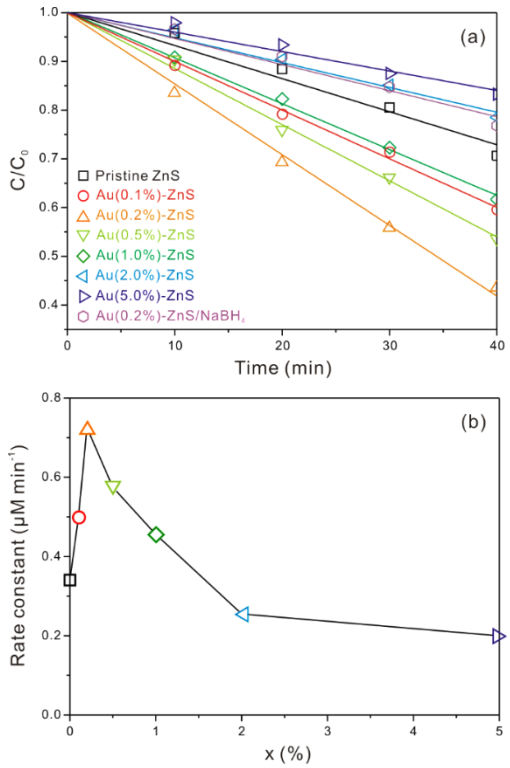

Figure 4-14 Kinetic plots (a) and rate constants (b) for the photocatalytic decomposition of 4NP *via* indicated photocatalysts under xenon-lamp irradiation.

Table 4-3

Photocatalytic degradation rate constants of 4-nitrophenol via indicated nanocatalysts.

Sample	Rate constant ($\mu M\ min^{-1}$)
No catalyst	0.02
Commercial ZnS	0.14
Pristine ZnS	0.34
Au(0.0%)-ZnS	0.36
Au(0.1%)-ZnS	0.50
Au(0.2%)-ZnS[a]	0.73
Au(0.2%)-ZnS/$NaBH_4$	0.27
Au(0.5%)-ZnS	0.58
Au(1.0%)-ZnS	0.46
Au(2.0%)-ZnS	0.26
Au(5.0%)-ZnS	0.20

[a] The degradation rate constant of 4-nitrophenol via Au(0.2%)-ZnS nanobelts under no light is 0.01 $\mu M\ min^{-1}$.

The photocatalytic performances of pristine ZnS and Au(x%)-ZnS nanobelts have been estimated by monitoring the decomposition of 4NP (Figure 4-14), and observed photocatalytic degradation rate constants are presented in Table 4-3. All the degradation profiles follow zero-order kinetics, in which decomposition rates are maintained regardless of the concentration of remaining 4NP. From the zero-order kinetics of photocatalytic degradation, it can be deduced that the rate determining step of photocatalytic degradation is not the direct reduction or oxidation of 4-nitrophenol but the generation of reactive radical species by excited charges. Because the recombination of excited charges is

blocked by gold nanoparticles, long-lived excited electrons and holes can be formed to participate in the photocatalytic reaction, leading to the enhancement of photocatalytic efficiencies. The optimized photocatalyst of Au(0.2%)-ZnS nanobelts has displayed the highest photocatalytic activity of decomposing 4NP. With gold deposition on the surfaces of ZnS nanobelts, excited charges have been effectively separated, leading to the increase of photocatalytic degradation activity. Compared with commercial ZnS and pristine ZnS nanobelts, the optimized photocatalyst has represented 5.2 and 2.1 times higher photocatalytic activity, respectively, proving that photodeposition is an effective method to enhance photocatalytic activity. However, it has been found that the photocatalytic activity decreases as the wt% of gold is higher than the optimum value of 0.2%. Due to the low crystallinity of surface-decorated gold nanoparticles, large gold nanoparticles act as recombination sites of excited charges. Thus, excess surface decoration with gold nanoparticles reduces photocatalytic efficiencies. The optimized photocatalyst has been compared with Au(0.2%)-ZnS/$NaBH_4$ nanobelts, which were prepared by reducing gold precursors with a reducing agent of $NaBH_4$ instead of irradiation. The photocatalytic rate constant of Au(0.2%)-ZnS/$NaBH_4$ (0.27 $\mu M\ min^{-1}$) has been found to be much smaller than that of Au(0.2%)-ZnS nanobelts (0.73 $\mu M\ min^{-1}$). The photodeposition process deposits gold on the surfaces of ZnS nanobelts, effectively forming charge-separating junctions. However, the deposition of gold nanoparticles by using a reducing agent produces gold nanoparticles in the solution as well as on ZnS nanobelts. Thus, although the employed amount of gold precursors was the same for Au(0.2%)-ZnS and Au(0.2%)-ZnS/$NaBH_4$, Au-ZnS junctions which can separate electrons and holes effectively have

been produced more richly in Au(0.2%)-ZnS nanobelts, suggesting that the photodeposition is a good approach to enhance the photocatalytic activity. Furthermore, the reusability of pristine ZnS and Au(0.2%)-ZnS nanobelts has been monitored by conducting recycling tests of photocatalysts (Figure 4-15). The optimized photocatalysts maintained 75% of the original photocatalytic efficiency after three cycles, while 22% of the original photocatalytic activity remained after 10 cycles. Compared with pristine ZnS nanobelts, Au-ZnS nanobelts showed slightly lower stability during photocatalytic reactions, revealing that the photodeposition process has not increased the photocatalytic stability of ZnS nanobelts.

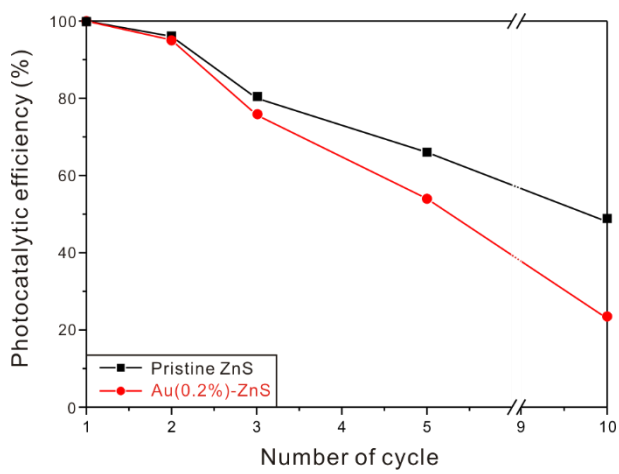

Figure 4-15 Photocatalytic recycling tests of pristine ZnS (black) and Au(0.2%)-ZnS nanobelts (red).

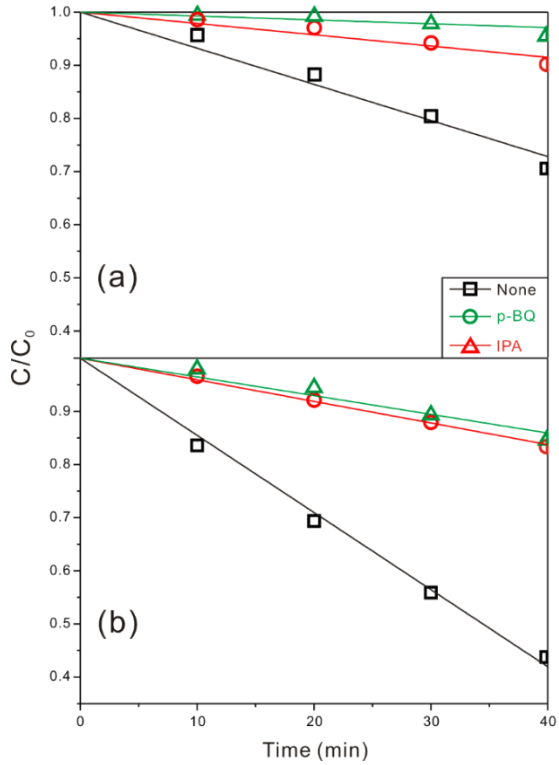

Figure 4-16 Photocatalytic decomposition profiles of 4NP *via* pristine ZnS (a) and Au(0.2%)-ZnS nanobelts under designated scavengers.

The reaction mechanism of photocatalytic 4-nitrophenol degradation has been studied by adding a specific radical scavenger (p-BQ for $\cdot O_2^-$ or IPA for $\cdot OH$) into the photocatalytic reaction vessel (Figure 4-16). Because the degradation kinetics of 4NP follows zero-order kinetics, neither direct reduction nor direct oxidation of 4NP is the rate determining step of the photocatalytic reaction. Thus, the photocatalytic decomposition rate of 4NP mainly depends on the formation rate of reactive radical species, which are generated by excited electrons and holes. Excited electrons reduce oxygen molecules to

generate superoxide radicals and excited holes oxidize hydroxyl ions to produce hydroxyl radicals. For pristine ZnS nanobelts, the photocatalytic activity decreased by 85.1% and 66.6% when p-BQ and IPA, respectively, were added, revealing that the formation of a superoxide or hydroxyl radical is the rate-determining step during the photocatalytic reaction. Meanwhile, for Au(0.2%)-ZnS nanobelts, the photocatalytic activity decreased by 72.8% and 70.5% when p-BQ and IPA, respectively, were added, suggesting that the main radical species facilitating the photocatalytic activity is also the superoxide radical or the hydroxyl radical. Thus, in spite of the enhancement of charge separation and the photocatalytic efficiency, the main radical species has not been changed by the photodeposition. In summary, the deposition of gold nanoparticles on ZnS nanobelts promotes the photocatalytic efficiency of ZnS nanobelts significantly owing to the enhanced generation of reactive radicals, which are facilitated by gold-induced charge separation.

4.5. Conclusion

The surfaces of ZnS nanobelts have been decorated with gold nanoparticles *via* a direct photodeposition process for enhanced photocatalytic dye decomposition. Under xenon-lamp irradiation, photoexcited electrons on the conduction band of ZnS directly reduce gold precursors to produce gold nanoparticles on ZnS nanobelts. Because the gold nanoparticles are formed directly by excited electrons in the absence of any reducing agents or surfactants, junctions between gold nanoparticles and ZnS nanobelts are formed

effectively to separate excited charges in ZnS nanobelts. The charge separation of ZnS nanobelts has been demonstrated by monitoring PL spectra and decay kinetic profiles. With wt% increase of decorating gold nanoparticles, not only the intensity but also the lifetime of band-edge emission decrease steadily, suggesting that the excited charges of ZnS can be separated effectively by surface-decorating gold nanoparticles. The facilitated separation of excited charges increases the photocatalytic efficiency of ZnS nanobelts for the degradation of 4NP. The separated charges promote the generation of superoxide radicals or hydroxyl radicals, increasing photocatalytic activity. Compared with pristine ZnS nanobelts and commercial ZnS, the optimized photocatalyst of Au(0.2%)-ZnS nanobelts exhibits 2.1 and 5.2 times, respectively, higher photocatalytic activity. Overall, via a simple and facile photodeposition process, charge separating junctions between gold and ZnS have been formed effectively to increase the photocatalytic activity of ZnS nanobelts significantly.

4.6. Acknowledgement

This work has been supported by the National Research Foundation of Korea (grant number: 2017-006153).

4.7. References

[1] M. M. Khin, A. S. Nair, V. J. Babu, R. Murugan, S. Ramakrishna, *Energy Environ. Sci.*, **2012**, 5, 8075.

[2] N. Sharma, H. Ojha, A. Bharadwaj, D. P. Pathak, R. K. Sharma, *RSC Adv.*, **2015**, 5, 53381.

[3] Y. Qu, X. Duan, *Chem. Soc. Rev.*, **2013**, 42, 2568.

[4] M. D. Hernández-Alonso, F. Fresno, S. Suárez, J. M. Coronado, *Energy Environ. Sci.*, **2009**, 2, 1231.

[5] A. Kudo, Y. Miseki, *Chem. Soc. Rev.*, **2009**, 38, 253.

[6] Y. Jiao, Y. Zheng, M. Jaroniec, S. Z. Qiao, *Chem. Soc. Rev.*, **2015**, 44, 2060.

[7] X. Zhou, J. Wu, Q. Li, Y. Qi, Z. Ji, P. He, X. Qi, P. Sheng, Q. Li, J. Ren, *Chem. Eng. J.*, **2017**, 330, 294.

[8] M. R. Gholipour, F. Béland, T.-O. Do, *ACS Sustainable Chem. Eng.*, **2017**, 5, 213.

[9] J. Lee, S. Ham, D. Choi, D.-J. Jang, *Nanoscale*, **2018**, 10, 14254.

[10] J. Lee, Y. Kim, J. K. Kim, S. Kim, D.-H. Min, D.-J. Jang, *Appl. Catal. B: Environ.*, **2017**, 205, 433.

[11] S. Ham, D.-J. Jang, *J. Environ. Chem. Eng.*, **2018**, 6, 228.

[12] C.-C. Wang, J.-R. Li, X.-L. Lv, Y.-Q. Zhang, G. Guo, *Energy Environ. Sci.*, **2014**, 7, 2831.

[13] M. S. El-Shahawi, A. Hamza, A. S. Bashammakh, W. T. Al-Saggaf, *Talanta*, **2010**, 80, 1587.

[14] Y. Li, Y. Xue, J. Tian, X. Song, X. Zhang, X. Wang, H. Cui, *Sol. Energy Mater. Sol. Cells*, **2017**, 168, 100.

[15] X. Zhang, Y. Guo, J. Tian, B. Sun, Z. Liang, X. Xu, H. Cui, *Appl. Catal. B: Environ.*, **2018**, 232, 355.

[16] X. Hu, H. Zhao, J. Tian, J. Gao, Y. Li, H. Cui, *Sol. Energy Mater. Sol. Cells*, **2017**, 172, 108.

[17] B. Zhao, G. Mele, I. Pio, J. Li, L. Palmisano, G. Vasapollo, *J. Hazard. Mater.*, **2010**, 176, 569.

[18] S. Ahmed, M. G. Rasul, W. N. Martens, R. Brown, M. A. Hashib, *Desalination*, **2010**, 261, 3.

[19] X. Fang, L. Wu, L. Hu, *Adv. Mater.*, **2011**, 23, 585.

[20] X.-S. Fang, C.-H. Ye, L.-D. Zhang, Y.-H. Wang, Y.-C. Wu, *Adv. Funct. Mater.*, **2005**, 15, 63.

[21] X. Yu, P. Wei, Y. Li, *Mater. Lett.*, **2019**, 240, 284.

[22] Y.-S. Sue, K.-Y. Pan, D.-H. Wei, *Appl. Surf. Sci.*, **2019**, 471, 435.

[23] H. Liu, L. Hu, K. Watanabe, X. Hu, B. Dierre, B. Kim, T. Sekiguchi, X. Fang, *Adv. Funct. Mater.*, **2013**, 23, 3701.

[24] X. Fang, Y. Bando, C. Ye, D. Golberg, *Chem. Commun.*, **2007**, 3048.

[25] G. D. C. Pizarro, O. G. Marambio, M. Jeria-Orell, D. P. Oyarzun, *Mater. Res. Bull.*, **2018**, 98, 15.

[26] J. Yu, J. Zhang, S. Liu, *J. Phys. Chem. C*, **2010**, 114, 13642.

[27] Y. Kim, S. J. Kim, S.-P. Cho, B. H. Hong, D.-J. Jang, *Sci. Rep.*, **2015**, 5, 12345.

[28] Y. Kim, D.-J. Jang, *CrystEngComm*, **2014**, 16, 6989.

[29] X. Fang, T. Zhai, U. K. Gautam, L. Li, L. Wu, Y. Bando, D. Golberg, *Prog. Mater. Sci.*, **2011**, 56, 175.

[30] D. Samanta, T. I. Chanu, S. Chatterjee, *Mater. Res. Bull.*, **2017**, 88, 85.

[31] X. Xu, L. Hu, S. Liu, S. Wageh, A. A. Al-ghamdi, A. Alshahrie, X. Fang, *Adv. Funct. Mater.*, **2015**, 25, 445.

[32] X. Xu, S. Li, J. Chen, S. Cai, Z. Long, X. Fang, *Adv. Funct. Mater.*, **2018**, 28, 1902029.

[33] X. Fang, Y. Bando, M. Liao, U. K. Gautam, C. Zhi, B. Dierre, B. Liu, T. Zhai, T. Sekiguchi, Y. Koide, D. Golberg, *Adv. Mater.*, **2009**, 21, 2034.

[34] X. Hu, S. Lu, J. Tian, N. Wei, X. Song, X. Wang, H. Cui, *Appl. Catal. B: Environ.*, **2019**, 241, 329.

[35] Q. Zhang, M. M. Tavakoli, L. Gu, D. Zhang, L. Tang, Y. Gao, J. Guo, Y. Lin, S.-F. Leung, S. Poddar, Y. Fu, Z. Fan, *Nat. Commun.*, **2019**, 10, 727.

[36] A. Alarawi, V. Ramalingam, H.-C. Fu, P. Varadhan, R. Yang, J.-H. He, *Opt. Express*, **2019**, 27, A352.

[37] M. M. Tavakoli, S. M. Zakeeruddin, M. Gratzel, Z. Fan, *Adv. Mater.*, **2018**, 30, 1705998.

[38] W. Ouyang, F. Teng, M. Jiang, X. Fang, *Small*, **2017**, 13, 1702177.

[39] S. Han, L. Hu, N. Gao, A. A. Al-Ghamdi, X. Fang, *Adv. Funct. Mater.*, **2014**, 24, 3725.

[40] M.-Y. Lu, J. Song, M.-P. Lu, C.-Y. Lee, L.-J. Chen, Z. L. Wang, ACS Nano, *2009*, **3**, 357.

[41] J. Zhang, M. Xiao, Z. Liu, B. Han, T. Jiang, J. He, G. Yang, *J. Colloid Interface Sci.*, **2004**, 273, 160.

[42] B. Li, J. Chu, Y. Li, M. Meng, Y. Cui, Q. Li, Y. Feng, *Phys. Status Solidi A*, **2018**, 215, 170161.

[43] J. Zhang, Y. Wang, J. Zhang, Z. Lin. F. Huang, J. Yu, *ACS Appl. Mater. Interfaces*, **2013**, 5, 1031.

[44] W.-T. Chen, Y.-K. Lin, T.-T. Yang, Y.-C. Pu, Y.-J. Hsu, *Chem. Commun.*, **2013**, 49, 8486.

[45] Y. I. Choi, S. Lee, S. K. Kim, Y.-I. Kim, D. W. Cho, M. M. Khan, Y. Sohn, *J. Alloys Compd.*, **2016**, 675, 46.

[46] J. Liu, L. Chen, B. Duan, Z. Gu, Q. Luo, C. Duan, *RSC Adv.*, **2016**, 6, 38690.

[47] M. Fujii, K. Nagasuna, M. Fujishima, T. Akita, H. Tada, *J. Phys. Chem. C*, **2009**, 113, 16711.

[48] M. C. Hidalgo, J. J. Murcia, J. A. Navío, G. Colón, *Appl. Catal. A: Gen.*, **2011**, 397, 112.

[49] A. Kogo, N. Sakai, T. Tatsuma, *Nanoscale*, **2012**, 4, 4217.

[50] S. Singh, R. Pasricha, U. M. Bhatta, P. V. Satyam, M. Sastry, B. L. V. Prasad, *J. Mater. Chem.*, **2007**, 17, 1614.

[51] J. Liu, A. Wei, Y. Zhao, *J. Alloys Compd.*, **2014**, 588, 228.

[52] C. Xu, T. Sritharan, S. G. Mhaisalkar, M. Srinivasan, S. Zhang, *Appl. Surf. Sci.*, **2007**, 253, 6217.

[53] C. Pannu, M. Bala, S. A. Khan, S. K. Srivastava, D. Kabiraj, D. K. Avasthi, *RSC Adv.*, **2015**, 5, 92080.

[54] B. R. Fisher, H.-J. Eisler, N. E. Stott, M. G. Bawendi, *J. Phys. Chem. B*, **2004**, 108, 143.

[55] A. Peled, M. Naddaka, J.-P. Lellouche, *J. Mater. Chem.*, **2012**, 22, 7580.

[56] J. Ma, X. Guo, H. Ge, G. Tian, Q. Zhang, Appl. Surf. Sci. 434 (2018) 1007-1014.

[57] N. López-Ruiz, D. Hernández-Bélanger, M. A. Carvajal, L. F. Capitán-Vallvey, A. J. Palma, A. Martínez-Olmos, *Sens. Actuators B Chem.*, **2015**, 216, 595.

Chapter 5. Facile Fabrication of Reusable FeOOH-Polycarbonate Membranes for Effective Separation of Organic Molecules†

† This is submitted to *Separation and Purification Technology* by Sooho Ham, Dong-Won Jeong, and Du-Jeon Jang

5.1. Abstract

FeOOH-polycarbonate (PC) membranes have been facilely fabricated via interfacial synthesis; FeOOH rods of 200 nm in diameters are synthesized inside the pores of PC membranes. The as-synthesized FeOOH-PC membranes can effectively separate organic dyes under ambient conditions without consuming energies. The FeOOH particles exhibit high porosity having large surface areas and pore volumes. Although relatively smaller 4-nitrophenol (4NP) molecules can diffuse through a FeOOH-PC membrane, larger methyl blue (MB) molecules cannot diffuse through the membrane, leading to the separation of 4NP and MB molecules. After the separation, MB molecules are remained in the FeOOH membranes, leading to the color change of membranes from brown to grey. To reuse a FeOOH-PC membrane, remaining MB molecules inside the membrane can be degraded in 5 min via photo-Fenton reactions. FeOOH-PC membranes fabricated at room temperature have showed higher stability than those fabricated by hydrothermal synthesis, because FeOOH particles were partially transformed into other materials such as Fe_2O_3 during the hydrothermal synthetic procedure. Overall, FeOOH-PC membranes, synthesized facilely at room temperature, can be employed readily as separation membranes of organic molecules.

5.2. Introduction

Nowadays, organic pollutants such as pesticides, antibiotics, and organic dyes have caused numerous environmental and health problems.[1,2] In particular, organic pollutants in water are hard to be degraded by traditional degradation methods. Thus, various adsorption methods[3,4] and advanced oxidation processes (AOPs) like photocatalytic, Fenton, and photo-Fenton reactions[5-13] using reactive oxygen species (ROS) generated by nanocatalysts have been employed to eliminate the organic pollutants in water. In spite of the high efficiency for the degradation of organic molecules, severe disadvantages exist, limiting the applications of AOPs as water remediation processes. For example, after the water remediation processes, nanocatalysts have to be separated from the solution via centrifugation,[5,7-9] magnetic separation,[14,15] or nanofiltration.[16] ROS react with the surfaces of nanocatalysts during AOPs, leading to the leakage of heavy metal ions. It is hard to degrade organic pollutants completely into final products like CO_2 and H_2O. Instead, byproducts might be formed during the degradation processes.[17,18] Crucially, due to the high reactivity of ROS, the selective degradation of organic molecules is almost impossible.

Separation membranes, which selectively separate specific molecules from mixed solutions or gases, have been studied extensively.[19-21] Separation membranes can effectively eliminate organic or inorganic pollutants without requiring energies like irradiation and do not generate any byproducts during separation processes. Separation membranes have been fabricated based on polymers,[22-24] metal-organic frameworks (MOFs),[25-27] zeolites,[28,29] and metal oxide nanoparticles.[30,31] Among them, metal-oxide

based separation membranes have higher stability and reusability than those based on polymers or MOFs. Compared to nanoadsorbents and nanocatalysts, separation membranes do not need any complex retrieving processes like magnetic separation or centrifugation. Thus, separation membranes based on metal oxides have a great potential in the fields of water remediation. While membranes for gas separation have been studied widely,[22,26-28] the fabrication of separation membranes for water-dissolved organic molecules is still challenging. To separate organic molecules dissolved in water, membranes have to be formed densely. Otherwise, organic pollutants would leak through separation membranes. To fabricate dense membranes, track-etched membranes have been applied in this work. By filling the pores of the membranes with adsorbents, separation membranes can be easily fabricated.

To reuse the separation membranes, the membranes should be cleansed after the separation of organic molecules. Among various AOPs, the photo-Fenton reaction is suitable for the membrane cleaning reaction. Photo-Fenton reactions degrade organic molecules by using hydroxyl radicals (·OH) formed by reactions between iron ions and H_2O_2.[10-13,32-37] Fe^{3+} complexes or nanoparticles absorb light and react with H_2O_2 to form ·OH and Fe^{2+}. Then, Fe^{2+} reacts with H_2O_2 to form ·OH and Fe^{3+}, and ·OH radicals formed during the reaction degrade organic molecules. Conventional photo-Fenton reactions, which use Fe^{2+} and Fe^{3+} ions, form iron sludge after the reactions.[10-13] However, particles containing Fe^{2+}/Fe^{3+} proceed photo-Fenton reactions without forming iron sludge. Thus, iron-containing separation membranes would be reusable via the photo-Fenton cleaning.

For the facile fabrication of separation membranes, we have introduced interfacial

synthesis based on track-etched polycarbonate (PC) membranes. Interfacial synthesis using the PC membranes have been reported previously.[38,39] To be cleaned via the photo-Fenton reaction, membranes having iron ions have to be fabricated. FeOOH particles have been investigated widely as photo-Fenton catalysts, adsorbents, and separating membranes.[32,40,41] Moreover, FeOOH particles can be easily fabricated by mixing Fe^{2+} or Fe^{3+} ions with OH^- ions.[42-45] First, Fe^{2+} ions adsorb on the pores of track-etched PC membranes. Then, 2-methylimidazole dissolved in 1-octanol is dropped on the membranes; 2-methylimidazole generates OH^- ions when contacted with H_2O at the pores. The adsorbed Fe^{2+} ions react with OH^- ions and are subsequently oxidized into Fe^{3+} ions by dissolved oxygen molecules, leading to the formation of FeOOH particles.[44] Through the interfacial synthetic procedure, we have fabricated recyclable FeOOH-PC membranes, which can separate organic molecules well.

5.3. Experimental

5.3.1. Materials

N,N-Dimethylformamide (DMF, l, 99.8%), iron sulfate ($FeSO_4$, s, 99.0%), methylene blue (MnB, s, 82.0%), methyl blue (MB, s), 2-methylimidazole (2MIM, s, 99%), 4-nitrophenol (4NP, s, 99%), 1-octanol (l, 99%), and isopore track-etched polycarbonate (PC) membranes (25 μm thickness, 25 mm diameter, 0.2 μm pore diameter) were purchased from Sigma-Aldrich. Hydrochloric acid (aq, 35.0%), hydrogen peroxide (aq, 30.0%),

methyl orange (MO, s, 85%) and sodium hydroxide (s, 97.0%) were purchased from Daejung Chemicals. Ultrapure deionized water (>15 MΩ cm) from an ELGA PURELAB Option-S system was used throughout the experiments.

5.3.2. Fabrication of FeOOH-polycarbonate membranes

FeOOH-PC membranes were prepared via interfacial synthesis using isopore track-etched PC membranes.[38,39] First, a PC membrane was floated on 10 mL of a freshly prepared 50 mM $FeSO_4$ aqueous solution for 20 min. Then, 40 μL of 0.40 M 2MIM in 1-octanol was slowly added on the PC membrane with a micropipette. The reaction system was set aside in open air at room temperature for 1 h and the membrane was transferred to a Buchner funnel and washed with ethanol thoroughly. For the hydrothermal synthesis of FeOOH-PC membranes, the same procedure was proceeded in a 50 mL Teflon-lined autoclave at 120 °C for 1 h. While the FeOOH-PC membranes synthesized at room temperature will be called as FeOOH/RT, the membranes synthesized via the hydrothermal process will be named as FeOOH/HT. To obtain FeOOH particles, an as-prepared FeOOH-PC membrane was dissolved in 1.5 mL DMF, which dissolved the PC membrane selectively. Produced FeOOH particles were washed 3 times with DMF and ethanol with centrifugation at 4000 rpm for 10 min. All the membranes and particles were dried in a vacuum oven at 40 °C for 6 h.

5.3.3. Characterization

X-ray diffraction (XRD) patterns were attained using a New D8 advance diffractometer

with radiation from Cu Kα (0.1542 nm) while X-ray photoelectron spectroscopy (XPS) spectra were measured by a KRATOS AXIS-HSi spectrometer with a 150 W Mg anode. FTIR spectra were obtained with a Nicolet 6700 FTIR spectrophotometer. While the transmission electron microscopy (TEM) images of FeOOH particles were obtained by a Hitachi H-7600 microscope, high-resolution TEM (HRTEM) images, selected area electron diffraction (SAED) patterns, and energy-dispersive x-ray (EDX) line scanning profiles were monitored using a JEOL JEM-2100F microscope. Field-emission scanning electron microscopy (FESEM) images and energy-dispersive x-ray (EDX) profiles were obtained with a ZEISS MERLIN Compact microscope. UV-vis absorption spectra were monitored by using a Scinco S3100 spectrophotometer, and diffuse-reflectance (DR) spectra were taken employing an Ocean Optics USB2000+ spectrometer. Brunauer-Emmett-Teller (BET) surface areas, pore sizes, and total pore volumes were analyzed using a Micromeritics ASAP 2020 surface area analyzer.

5.3.4. Organic-dye separation and photo-Fenton cleaning

The aqueous stock solutions of 4NP (50 mM), MO (10 mM), MnB (50 mM), and MB (10 mM) were prepared, and the organic dyes were separated via a selective diffusion method [51]. To separate the organic dyes, an as-synthesized FeOOH membrane was floated on 50 mL of water. For the evaluation of single-dye diffusion, 100 μL of 4NP (25 mM), MO (5 mM), MnB (5 mM), or MB (5 mM) was slowly added onto the floating FeOOH membrane. With mild magnetic stirring, aliquots of 1.0 mL were taken at designated times from the solution below the membrane. To monitor the penetration rate

of each dye, the absorption spectrum of each aliquot was measured with a UV-vis spectrophotometer. Note that 10 μL of 1.0 M NaOH(aq) and 10 μL of 1.0 M HCl(aq) were added to the aliquots of 4NP and MB, respectively, because 4NP and MB showed pH-dependent UV-vis absorption spectra. For the separation of mixed 4NP and MB, the same procedure of single-dye separation was carried out and UV-vis absorption spectra were taken in both acidic and basic conditions. After the separation, the FeOOH-PC membrane was retrieved easily with a tweezer and transferred to a plastic plate. 50 μL of 9.8 M H_2O_2(aq) was added onto the FeOOH membrane, which was then irradiated with a 300 W xenon-lamp. DR spectra were measured to estimate the remaining amount of MB molecules in the FeOOH-PC membrane before and after photo-Fenton cleaning reactions.

5.3.5. Catalytic and adsorption properties of FeOOH particles

For the evaluation of the adsorption and photo-Fenton properties of as-prepared FeOOH particles, 1.5 mg of FeOOH particles was dispersed in 30 mL of H_2O via sonication. 50 μL of a 4NP or MB stock solution was added into the colloid, whose total volume was then adjusted to 50 mL by adding H_2O. For the adsorption experiments, 1.0 mL aliquots were taken at designated intervals and the particles were separated with centrifugation at 10000 rpm for 10 min. Then, their UV-vis absorption spectra were measured to estimate the remaining concentrations of 4NP or MB. For photo-Fenton experiments, 50 mL of a 50 μM 4NP or 10 μM MB aqueous solution containing 1.5 mg of FeOOH particles was kept in dark with vigorous stirring for 1 h to attain the adsorption-desorption equilibrium. After the equilibrium, 100 μL of 9.8 M H_2O_2(aq) was added to the solution, which was then

transferred to a 200 mL quartz vessel. The solution was irradiated with a 300 W xenon lamp, and 1.0 mL aliquots were taken from the solution at designated intervals. Their absorption spectra were measured to monitor the degradation efficiency of 4NP or MB by FeOOH particles.

5.4. Results and discussion

5.4.1. Structural analysis

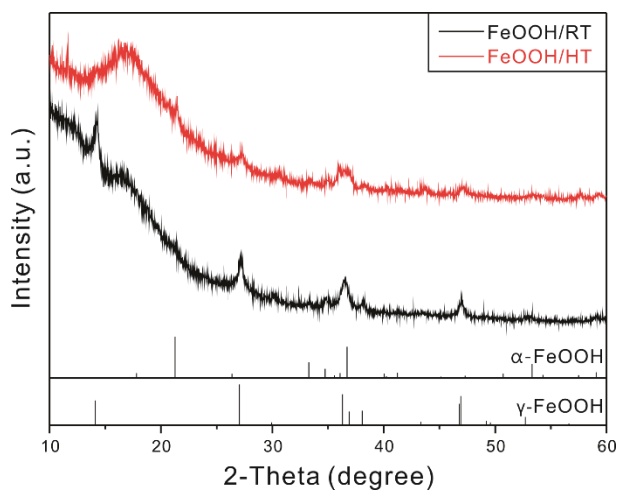

Figure 5-1 XRD patterns of indicated FeOOH-PC membranes. The standard diffraction patterns of γ-FeOOH and α-FeOOH are also presented.

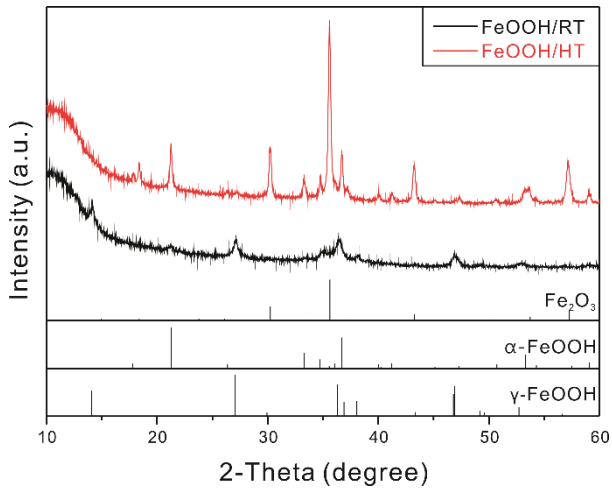

Figure 5-2 XRD patterns of indicated bare FeOOH particles after dissolving PC membranes with DMF. The standard diffraction patterns of α-FeOOH, γ-FeOOH, and Fe_2O_3 are also indicated.

The crystal structures of FeOOH/RT and FeOOH/HT particles embedded in PC membranes were investigated by conducting XRD analysis (Figure 5-1). For both FeOOH/RT and FeOOH/HT membranes, a broad peak from a pristine PC membrane appears around 17°. The diffraction peaks of FeOOH/RT and FeOOH/HT appear at different 2θ values. The XRD pattern of FeOOH/RT matches well with the standard reference pattern of γ-FeOOH (pdf# 00-044-1415). Meanwhile, the XRD peaks of FeOOH/HT agree well with the standard diffraction peaks of α-FeOOH (pdf# 01-075-5065) . To compare the crystal structures of FeOOH/RT and FeOOH/HT in detail, the XRD patterns of bare FeOOH/RT and FeOOH/HT particles were also investigated (Figure 5-2). The XRD patterns of bare FeOOH/RT and FeOOH/HT particles are similar to the respective ones of FeOOH/RT and FeOOH/HT membranes. It can be confirmed that the

diffraction peak around 17° from a pristine PC membrane disappears after the dissolution of FeOOH-PC membranes in DMF. However, some other peaks also appear around 2θ of 30°, 35°, and 43° for bare FeOOH/HT particles. These peaks match well with the standard diffraction peaks of Fe_2O_3 (pdf# 00-039-1346), revealing that FeOOH particles were partially transformed into Fe_2O_3 crystals during the hydrothermal synthesis of FeOOH/HT. By measuring FTIR spectra of bare FeOOH/RT and FeOOH/HT particles, vibrational functional groups were monitored (Figure 5-3). For both FeOOH/RT and FeOOH/HT particles, a strong peak derived from hydroxyl groups appears around 3400 cm^{-1}. For FeOOH/HT particles, an intense peak arising from Fe-O vibrations appears around 600 cm^{-1}, indicating that Fe_2O_3 particles were produced during the hydrothermal synthesis of FeOOH/HT.[49,50]

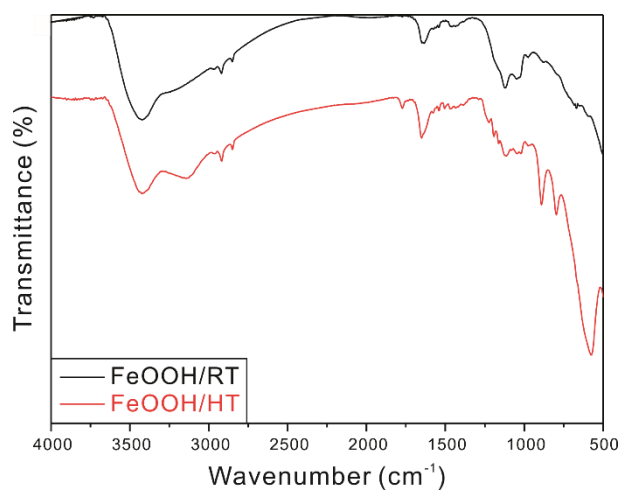

Figure 5-3 FTIR spectra of bare FeOOH/RT and FeOOH/HT particles after dissolving PC membranes with DMF.

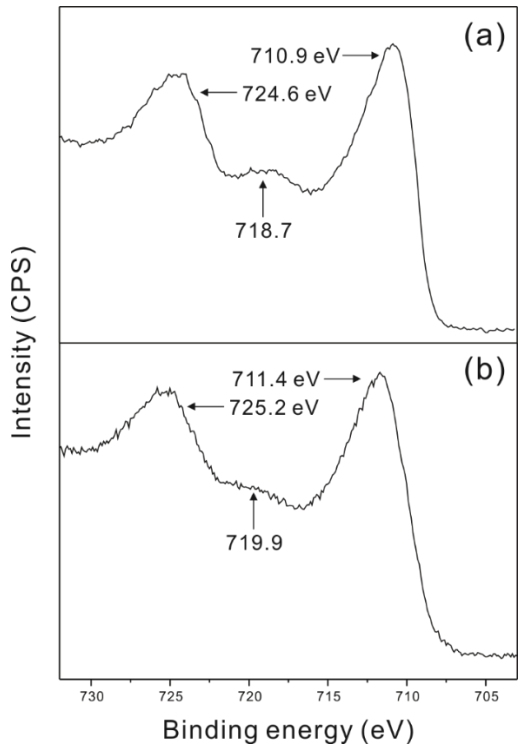

Figure 5-4 XPS spectra of Fe 2p from bare FeOOH/RT (a) and FeOOH/HT (b) particles.

To investigate the chemical states of Fe from FeOOH, Fe 2p XPS spectra of bare FeOOH/RT and FeOOH/HT particles have been monitored (Figure 5-4). The XPS spectra of Fe 2p show two distinctive peaks and one shoulder peak. While the Fe $2p_{3/2}$ and Fe $2p_{1/2}$ peaks of FeOOH/RT are located at 710.9 and 724.6 eV, respectively, those of FeOOH/HT are located at 711.4 and 725.2 eV, respectively. Each Fe $2p_{3/2}$ peak is associated with a satellite peak at approximately 8 eV higher binding energy, revealing that Fe^{2+} ions have been oxidized to Fe^{3+}.[46-48] Figure 5-5 shows that the XPS spectrum of O 1s can be deconvoluted into 3 Gaussian peaks. The peaks around 529 and 531 eV correspond respectively with Fe-O and Fe-O-H from FeOOH, while the peak around 533 eV is derived

from adsorbed H_2O molecules. While FeOOH/RT particles presented 14 at% of Fe and 85 at% of O, FeOOH/HT represented 15 at% of Fe and 84 at% of O. Only 1% of N was detected for both FeOOH/RT and FeOOH/HT particles, and S was not detected at all in XPS analysis. From the results of XRD and XPS, it can be deduced that FeOOH particles have been formed during the interfacial synthesis.

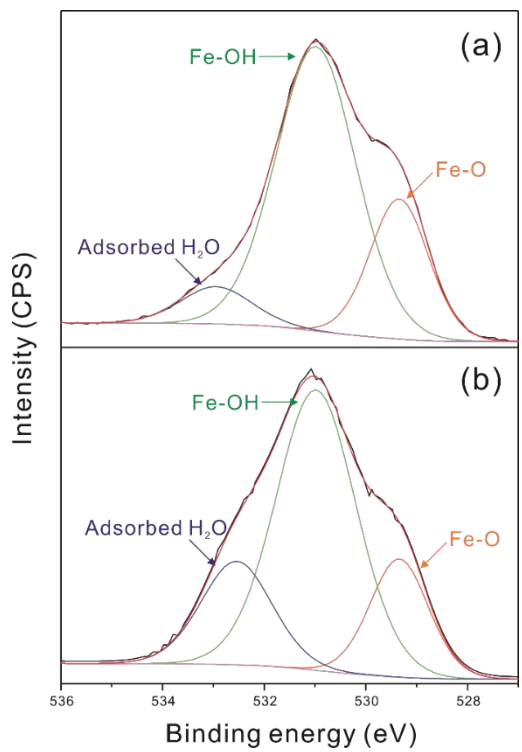

Figure 5-5 XPS spectra of O 1s from bare FeOOH/RT (a) and FeOOH/HT (b) particles.

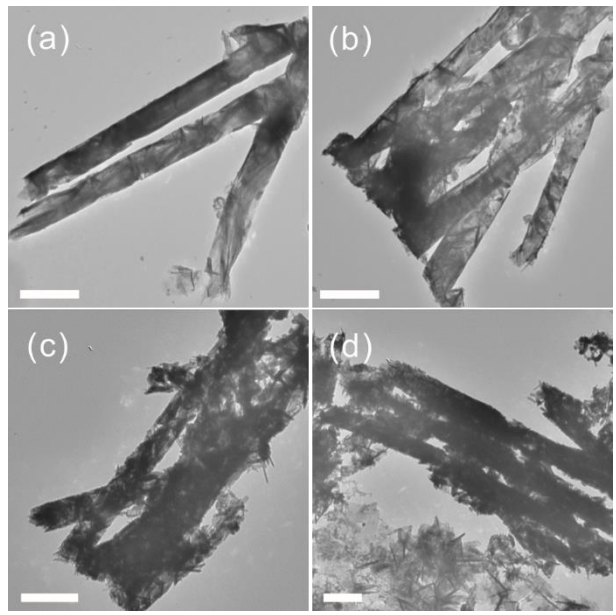

Figure 5-6 TEM images of FeOOH/RT (a,b) and FeOOH/HT (c,d) particles. Each scale bar indicates 500 nm.

The morphologies of FeOOH/RT and FeOOH/HT particles were monitored by measuring their TEM images (Figure 5-6), revealing that the particles were synthesized in rod shapes. The surfaces of FeOOH/RT rods were smoother than those of FeOOH/HT rods. Each average length of FeOOH/RT and FeOOH/HT particles is longer than 1 μm and the typical thickness is shorter than 200 nm. Because the FeOOH particles have been synthesized inside the 200 nm pore channels of PC membranes, the average diameter of FeOOH particles is shorter than 200 nm. Furthermore, the average length of FeOOH rods (5 μm) is much shorter than the thickness of a PC membrane (25 μm), as OH^- and Fe^{2+} ions had to diffuse through the pores of the PC membrane to form FeOOH. After the formation of FeOOH rods at the initial synthetic procedure, the diffusion of OH^- and Fe^{2+} into the

pores was slowed down. For bare FeOOH/HT particles, smaller nanoparticles have also been observed (Figure 5-7). Due to the transformation of FeOOH particles into Fe_2O_3 nanoparticles, smaller particles with 100 nm thickness and 350 nm length were found as well, revealing that the surfaces were roughened and that smaller nanoparticles were generated during the FeOOH/HT synthesis.

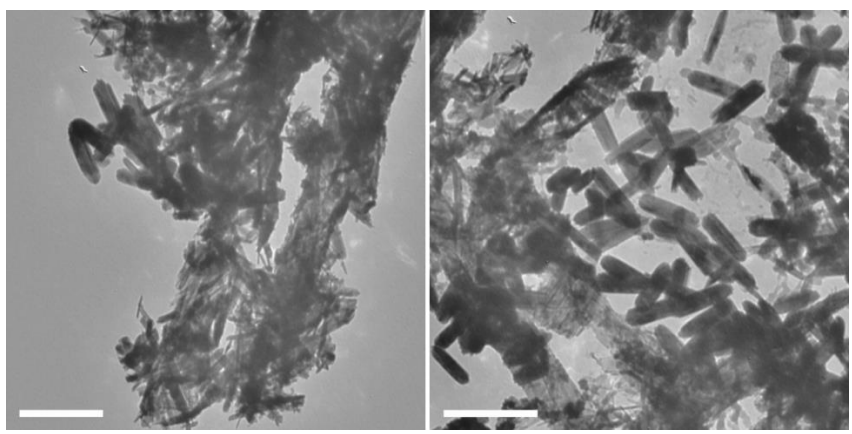

Figure 5-7 TEM images of FeOOH/HT (c,d) particles. Each scale bar indicates 500 nm.

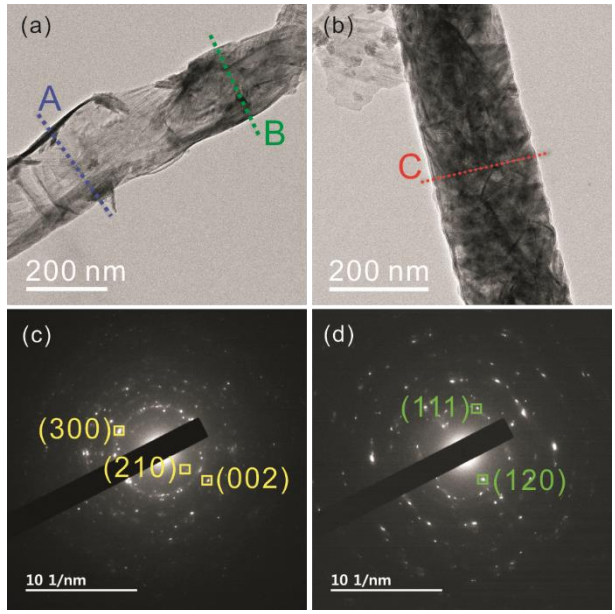

Figure 5-8 HRTEM images (top) and SAED patterns (bottom) of a FeOOH/RT rod (a,c) and a FeOOH/HT rod (b,d).

Information on more detailed morphologies and crystallinities has been monitored by measuring HRTEM images and SAED patterns (Figure 5-8). As seen in Figure 5-8a, a FeOOH/RT rod consists of two parts having different contrasts. The Fe EDX profiles scanned along the lines of A, B, and C are presented in Figure 5-9; the profile along the line A reveals the hollow property of a FeOOH/RT rod and the profiles along the line B shows the relatively filled structure of a FeOOH/RT rod.

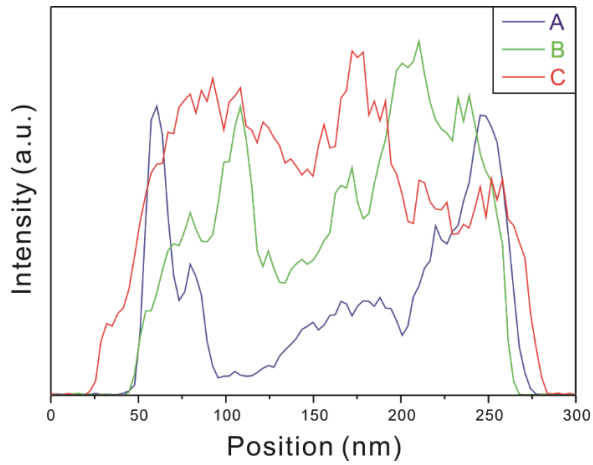

Figure 5-9 Fe EDX elemental profiles of FeOOH/RT (A,B) and FeOOH/HT (C), obtained from the lines of A, B, and C in Figure 5-8.

However, the HRTEM image of a FeOOH/HT rod (Figure 5-8b) shows uniform contrast compared to that of a FeOOH/RT rod. Also, the elemental profile obtained along the line C reveals the less vacant structure of a FeOOH/HT rod. More detailed crystal structures were monitored by measuring SAED patterns from the rods of Figure 5-8a,b. Due to the low synthetic temperature, the SAED pattern of a FeOOH/RT rod (Figure 5-8c) exhibits the ring pattern, revealing the low crystallinity of a FeOOH/RT rod. The dots inside the yellow squares of Figure 5-8c match well with the (002), (300), and (210) crystal facets of γ-FeOOH, agreeing with the results of XRD. The SAED pattern of a FeOOH/HT rod (Figure 5-8d) presents bright dots, designating that the FeOOH/HT rod shows higher crystallinity than the FeOOH/RT rod does. Also, the dots inside the green squares in Figure 5-8d agree well with the (111) and (120) facets of α-FeOOH and correspond with the results described with the XRD patterns of Figure 5-1. The atomic compositions of

FeOOH/RT and FeOOH/HT were also monitored via measuring low-magnification SEM images and EDX elemental profiles (Figure 5-10). The EDX elemental profiles of Figure 5-10a,c show that bare FeOOH/RT and FeOOH/HT particles are composed of Fe and O atoms. Note that S and N atoms from the precursors ($FeSO_4$ and 2MIM) have been observed hardly. The elemental profiles of FeOOH/RT and FeOOH/HT rods on PC membranes (Figure 5-10b,d) reveal that the FeOOH-PC membranes are composed of C, O, and Fe. The content of carbon increases for FeOOH-PC membranes because a PC membrane mainly consists of C. However, obvious differences in elemental contents have not been observed between FeOOH/RT and FeOOH/HT.

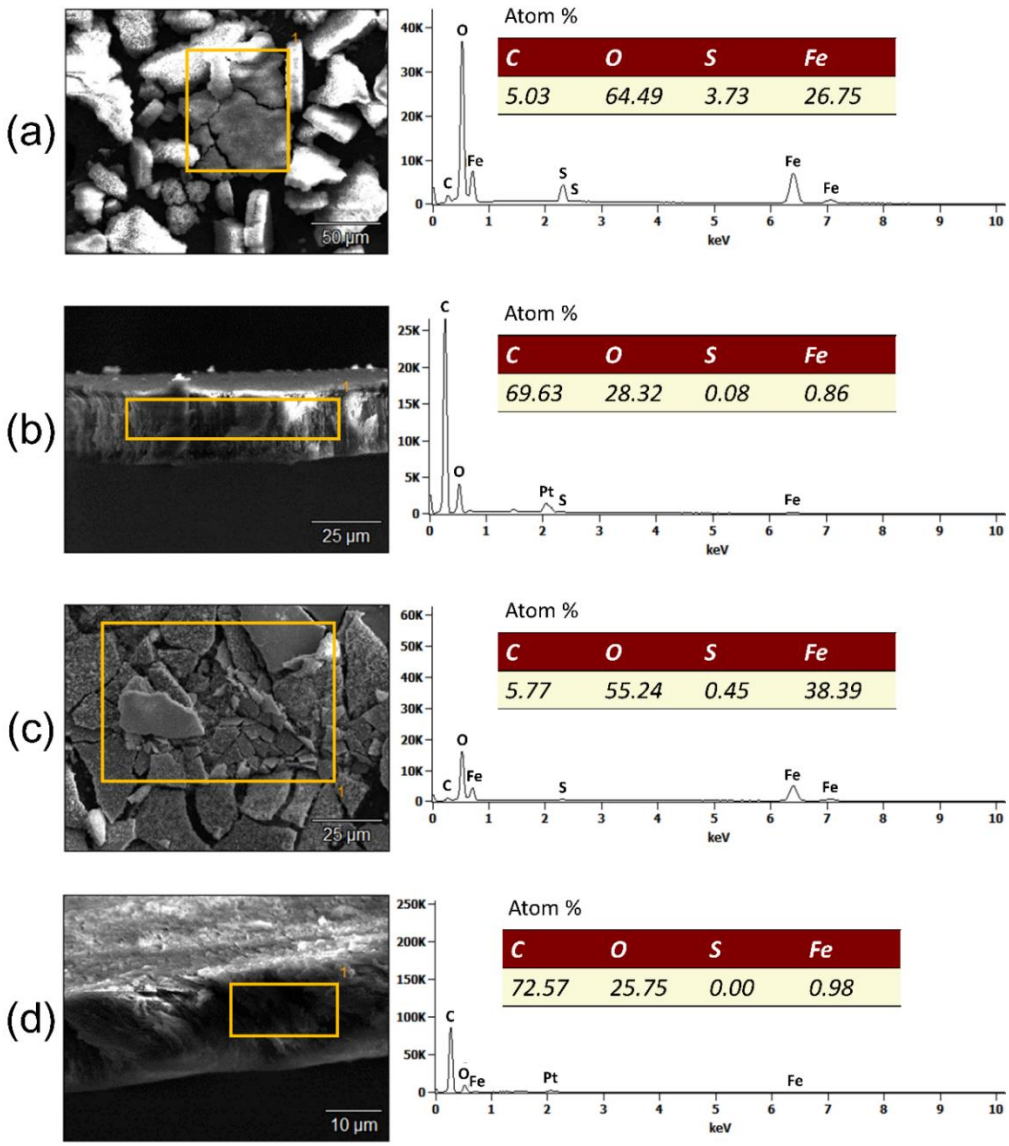

Figure 5-10 Low-magnification SEM images (left) and EDX elemental profiles (right) scanned inside the squares of the SEM images of bare FeOOH/RT particles (a), a FeOOH/RT-PC membrane (b), bare FeOOH/HT particles (c), and a FeOOH/HT-PC membrane (d).

5.4.2. Organic molecules separation properties

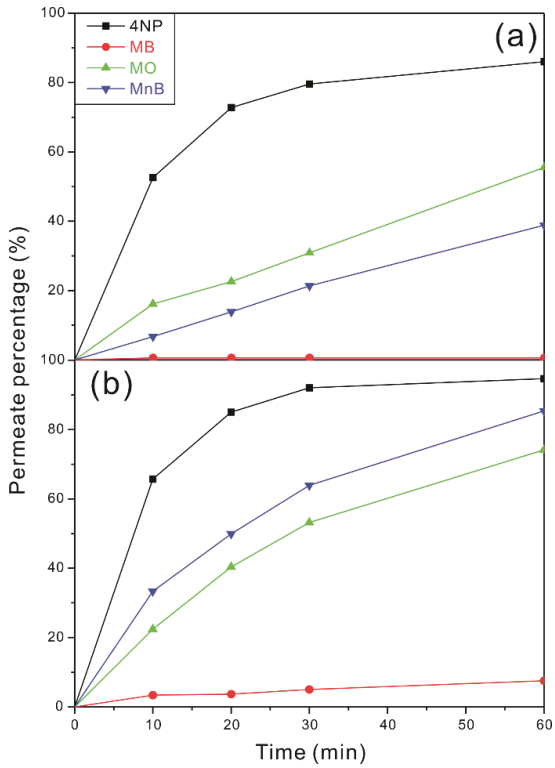

Figure 5-11 Organic dyes penetration tests for 4NP, MB, MO, and MnB by FeOOH/RT (a) and FeOOH/HT (b) membranes.

Before the separation of organic dyes, the diffusion properties of a single dye through FeOOH-PC membranes were monitored (Figure 5-11). Whereas 4NP molecules passed both the FeOOH/RT and FeOOH/HT membranes most rapidly, MB molecules hardly penetrated the membranes. Although MO and MnB also passed through the membranes, their diffusion is slower than the diffusion of 4NP. The 4NP (MW: 139.1 g mol^{-1}) has the shortest diameter among the employed organic dyes and anionic MB (MW: 799.8 g mol^{-1})

has the longest diameter.[51] When dissolved in water, 4NP molecules exist in two forms: the neutral form of 4NP and the anionic form of 4-nitrophenolate. MnB is a cationic dye with MW of 319.8 g mol^{-1} and MO is an anionic dye with MW of 327.33 g mol^{-1}. For MnB and MO with similar MW and diameter (~1 nm),[51] their diffusion rates through the FeOOH membranes are similar to each other, suggesting that MW, rather than the charge of an organic molecule, is the mainly determining factor of the diffusion rate. Thus, we have carried out especially the separation of 4NP and MB, which show the highest and the lowest diffusion rates, respectively, through the membranes.

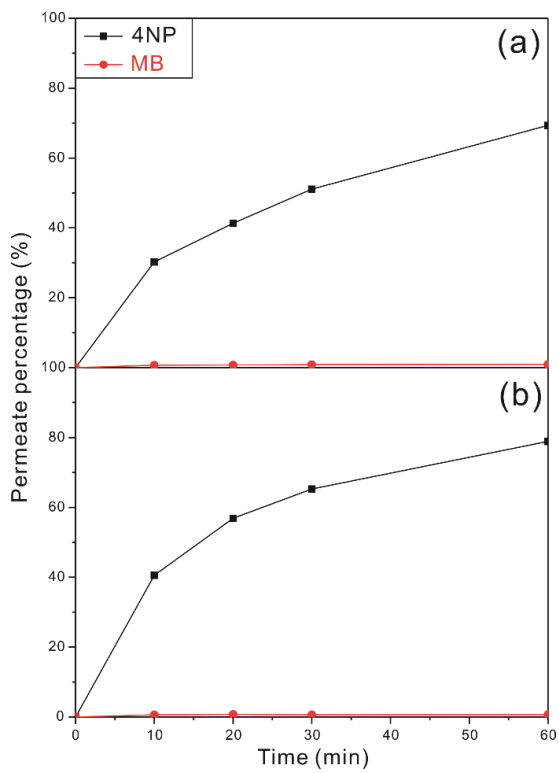

Figure 5-12 Separation of 4NP/MB by FeOOH/RT (a) and FeOOH/HT (b) membranes.

An aqueous solution containing 4NP and MB was dropped on a water-floating FeOOH/RT or FeOOH/HT membrane, and the UV-vis absorption spectra of the solution below the membrane were monitored (Figure 5-12). Whereas 4NP molecules passed through the membrane fast, MB molecules hardly passed through the membrane. After 1 h separation, about 70% and 80% of 4NP diffused through the FeOOH/RT and FeOOH/HT membranes, respectively. Also, the dye concentration of the remaining solution above the membrane was monitored (Figure 5-13). As 4NP molecules passed through the membranes well, the concentration of 4NP decreased by 80% after separation via both FeOOH/RT and FeOOH/HT membranes. However, MB molecules decreased by 25% and 15% after separation via FeOOH/RT and FeOOH/HT membranes, respectively. Thus, 4NP and MB could be successfully separated by FeOOH/RT and FeOOH/HT membranes through the simple diffusion-mediated separation method. As MB molecules were adsorbed to the FeOOH membranes, the concentration of MB in the remaining solution became smaller and the color of the membranes were changed from brown to grey. Thus, in order to reuse the membranes, the adsorbed MB molecules had to be degraded.

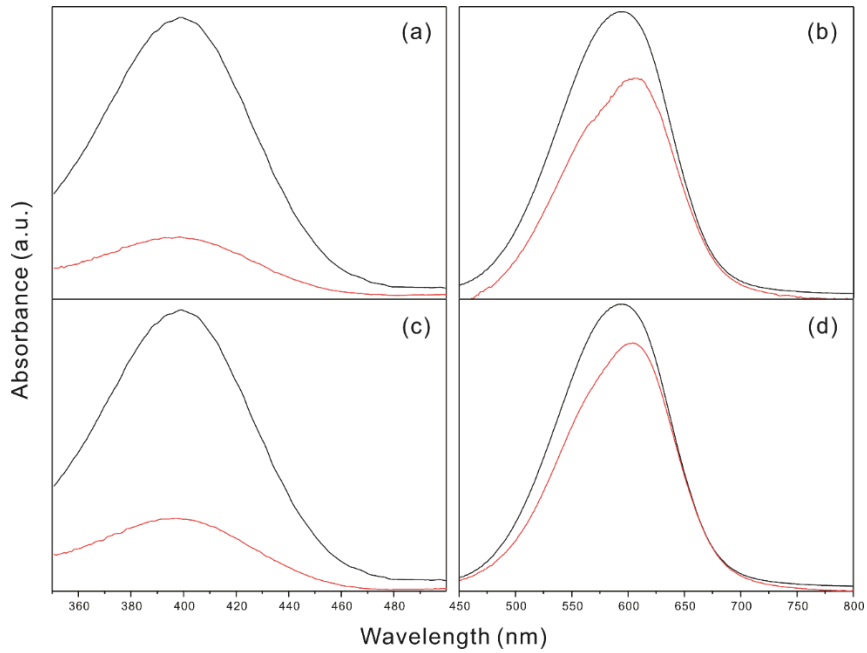

Figure 5-13 Absorption spectra of the 4NP (a,c) and MB (b,d) before (black) and after (red) 1 h separation by FeOOH/RT (top) and FeOOH/HT (bottom) membranes.

5.4.3. Photo-Fenton cleaning

The absorption spectra of FeOOH/RT and FeOOH/HT particles dispersed in ethanol have been monitored (Figure 5-14). Both FeOOH/RT and FeOOH/HT particles revealed an absorption band around 400 nm. Thus, a xenon lamp has been applied to conduct the photo-Fenton reaction. Bare FeOOH/RT and FeOOH/HT particles were applied first to the degradation of 4NP and MB via the photo-Fenton reaction (Figure 5-15). 4NP molecules were degraded well in the absence of catalysts; the FeOOH/RT particles slightly enhanced photocatalytic degradation efficiency while FeOOH/HT particles hardly enhanced the degradation efficiency. For MB, both FeOOH/RT and FeOOH/HT particles showed high

degradation efficiencies. Via the photo-Fenton reaction, adsorbed MB molecules to a FeOOH-PC membrane were also degraded. The degradation of MB molecules adsorbed to the membrane was monitored by measuring the DR spectral changes of a FeOOH/RT membrane (Figure 5-16). Prior to 4NP/MB separation, a FeOOH/RT membrane showed a DR absorption band below 600 nm. After 4NP/MB separation, a new absorption band around 600 nm appeared, revealing that MB molecules were adsorbed on the FeOOH/RT membrane. After conducting 5 min photo-Fenton cleaning, the new absorption band from MB was decreased and the DR spectrum of the FeOOH/RT membrane was recovered to show that of a pristine FeOOH/RT membrane.

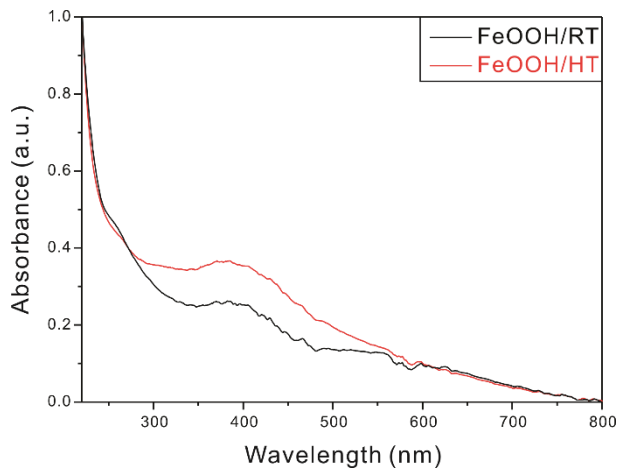

Figure 5-14 UV-vis absorption spectra of bare FeOOH/RT and FeOOH/HT particles, dispersed in ethanol at a concentration of 0.1 mg/mL.

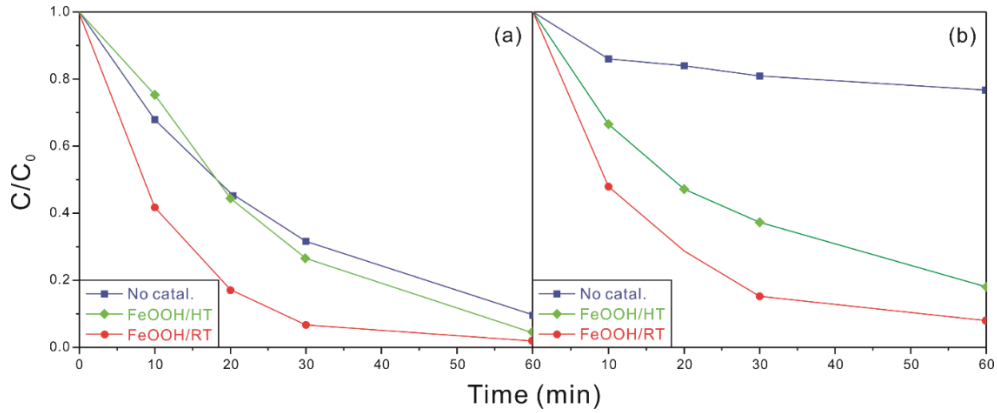

Figure 5-15 Photocatalytic degradation of 4NP (a) and MB (b) by no catalysts (blue), bare FeOOH/HT particles (green), and bare FeOOH/RT particles (red) dispersed in H_2O_2 under xenon-lamp irradiation.

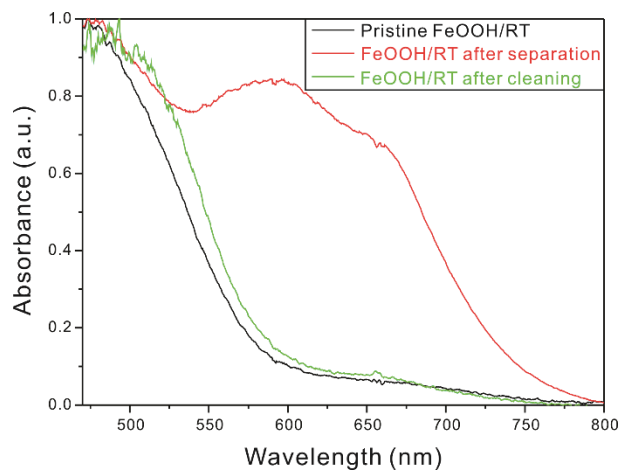

Figure 5-16 DR spectra of a pristine FeOOH/RT membrane (black), a FeOOH/RT membrane after 4NP/MB separation (red), and a FeOOH/RT membrane after photo-Fenton cleaning (green).

After each cleaning procedure of the membrane via the photo-Fenton reaction, 4NP and

MB molecules were separated repeatedly and the UV-vis absorption spectra of permeated solutions were monitored (Figure 5-17), suggesting that FeOOH/RT membranes have higher stability than FeOOH/HT membranes. The diffusion rate of 4NP for the FeOOH/RT membrane was hardly reduced during the recycle processes. However, the diffusion rate of 4NP for the FeOOH/HT membrane decreased rapidly; 65% of 4NP molecules passed through the membrane in the first cycle, but only 37% of 4NP passed through the membrane in the second cycle. Both FeOOH/RT and FeOOH/HT membranes blocked the diffusion of MB molecules well for a few cycles. However, as the photo-Fenton cleaning processes were conducted repeatedly, MB molecules started to diffuse through the membranes. Due to the high reactivity of ROS, generated during the photo-Fenton cleaning, FeOOH/RT and FeOOH/HT membranes were also degraded.

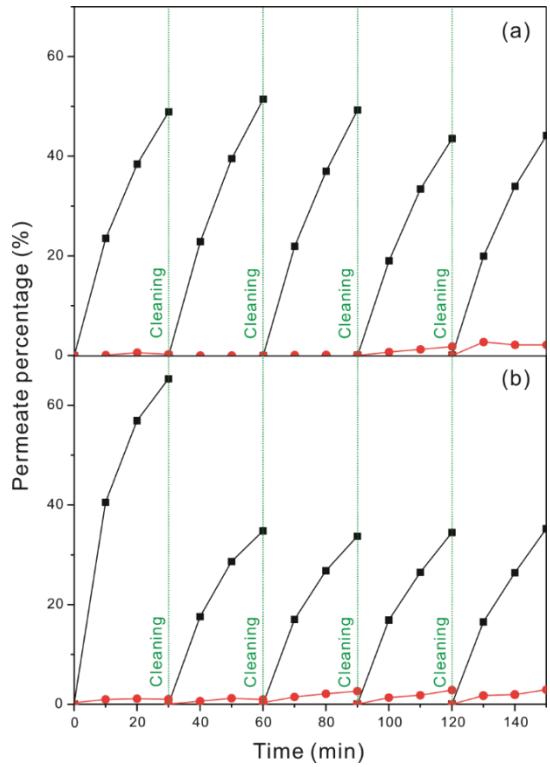

Figure 5-17 Recycling tests for the separation of 4NP (black) and MB (red) by FeOOH/RT (a) and FeOOH/HT (b) membranes.

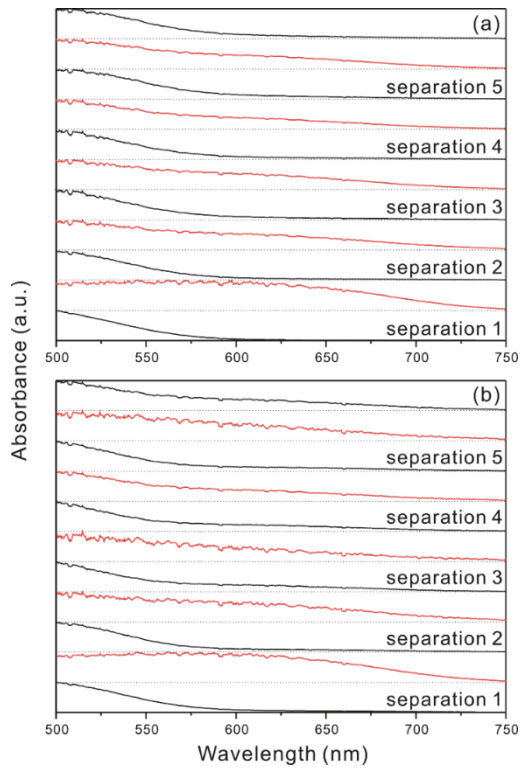

Figure 5-18 DR spectra of a FeOOH/RT membrane (a) and a FeOOH/HT membrane (b) after 4NP/MB separation (red) and photo-Fenton cleaning (black).

Furthermore, the DR spectra of the membranes after individual cycles were also monitored (Figure 5-18). The absorption band around 600 nm, arising from adsorbed MB molecules, disappeared after the photo-Fenton cleaning. The adsorbed MB molecules were degraded well via the photo-Fenton reaction during the first 5 cycles of separation and cleaning. The morphologies of FeOOH/RT and FeOOH/HT particles after 5 cycles of the photo-Fenton cleaning were also monitored by measuring TEM images (Figure 5-19); no obvious changes were observed in the TEM images. The surface functional groups were

monitored as well by measuring FTIR spectra after 5 cycles of the photo-Fenton cleaning (Figure 5-20). Compared to the FTIR spectrum before the photo-Fenton cleaning (Figure 5-3), the intensity of the peak around 3400 cm^{-1} arising from –OH functional groups has been increased largely, revealing that the surfaces of FeOOH particles have been hydroxylated by ·OH radicals.

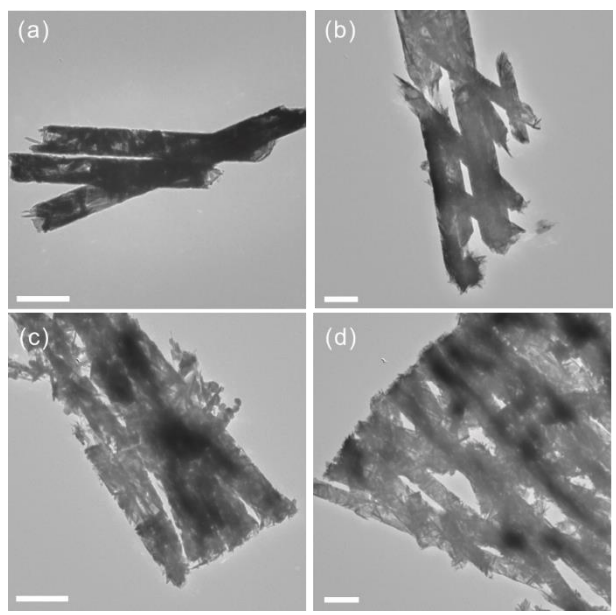

Figure 5-19 TEM images of FeOOH/RT (a,b) and FeOOH/HT (c,d) particles after 5 cycles of photo-Fenton cleaning.

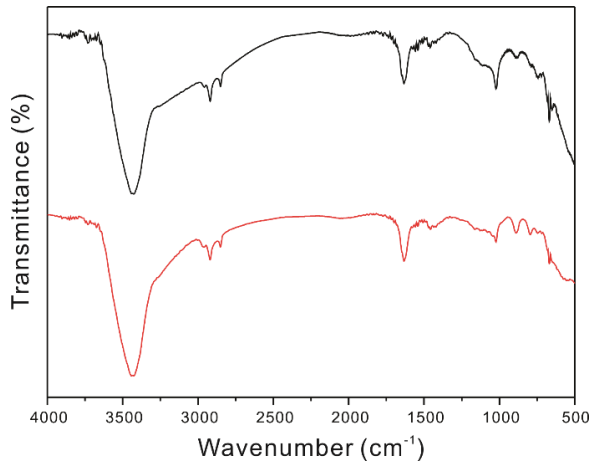

Figure 5-20 FTIR spectra of FeOOH/RT (black) and FeOOH/HT (red) particles after 5 cycles of photo-Fenton cleaning.

5.4.4. Mechanism analysis

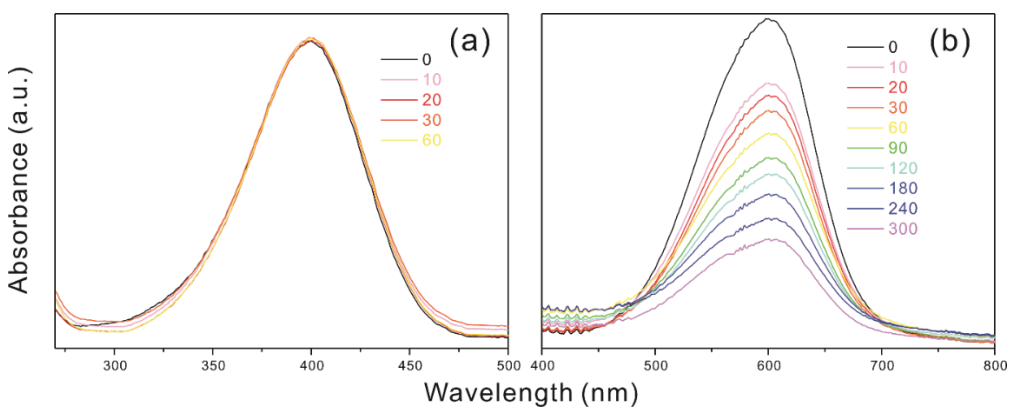

Figure 5-21 The absorption spectra of 4NP (a) and MB (b) during adsorption to FeOOH/RT particles. Times for adsorption are presented inside in the unit of min.

The detailed mechanisms of 4NP/MB separation by FeOOH/RT membranes were

studied by conducting adsorption tests and BET surface area analysis for FeOOH/RT particles. The adsorption of 4NP and MB molecules by FeOOH/RT particles was monitored (Figure 5-21); although 4NP molecules adsorbed hardly to FeOOH/RT particles, MB molecules adsorbed well to FeOOH/RT particles.

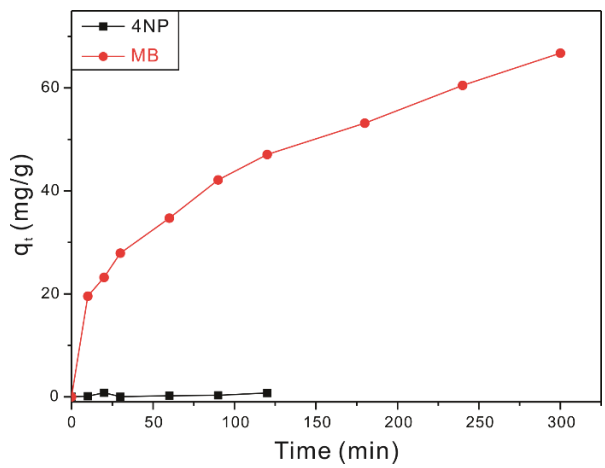

Figure 5-22 Time-dependent q_t of 4NP and MB in the presence of FeOOH/RT particles.

The calculated adsorption capacity (q_t) curves for 4NP and MB are presented in Figure 5-22; although the adsorption capacity of 4NP by FeOOH/RT particles increased hardly, that of MB increased significantly with adsorption time to reach 66 mg/g at 300 min. The adsorption kinetics of adsorbents is an important characteristics, revealing an adsorption efficiency and a possible rate-determining step. The adsorption kinetic curve was analyzed by fitting it with the intra-particle diffusion model, the pseudo-first order kinetics, and the pseudo-second order kinetics by using the respective following equations:[8]

$$q_t = k_i t^{1/2} + C$$

$$\ln (q_e - q_t) = \ln q_e - k_1 t$$

$$t / q_t = 1 /(k_2 q_e^2) + t / q_e$$

where, k_i, k_1, and k_2 are the respective rate constants of the intra-particle diffusion (mg g^{-1} $min^{-1/2}$), the pseudo-first-order kinetics (min^{-1}), and the pseudo-second-order kinetics (g mg^{-1} min^{-1}).

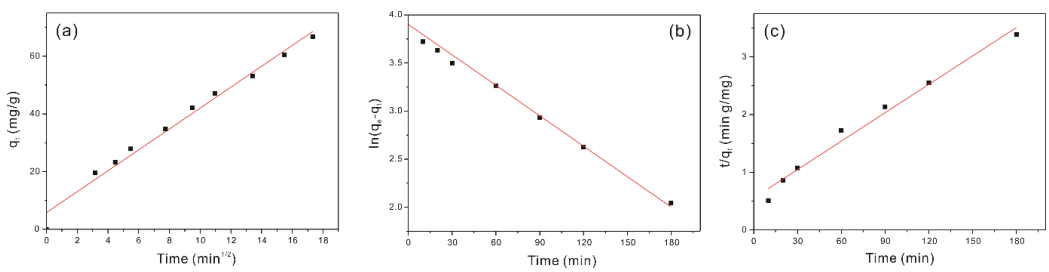

Figure 5-23 Intraparticle diffusion model (a), pseudo-first-order (b), and pseudo-second-order adsorption kinetics of MB by FeOOH/RT particles.

Table 5-1

Kinetic and intra-particle diffusion parameters for the adsorption of MB by FeOOH/RT particles.

Intraparticle diffusion			**Pseudo-first-order kinetics**			**Pseudo-second-order kinetics**		
k_i (mg/(g $min^{1/2}$))	C (mg/g)	R^2	k_1 (1/min)	$q_{e,clac}$ (mg/g)	R^2	k_2 (10^{-4}/min)	$q_{e,clac}$ (mg/g)	R^2
3.620	5.816	0.9824	0.0105	49.31	0.9766	4.873	60.90	0.9567

The best-fitted adsorption kinetic plots are presented in Figure 5-23, and the calculated parameters are also presented in Table 5-1. The R^2 value of the intra-particle diffusion model is larger than either one of the R^2 values of the pseudo-first-order model and the pseudo-second-order model, demonstrating that MB molecules adsorb to FeOOH/RT particles via the intra-particle diffusion. Furthermore, each of the theoretically calculated q_e values of the pseudo-first-order model and the pseudo-second-order model is smaller than the experimentally calculated q_t value after 300 min (66 mg/g), revealing that the both models could not explain the adsorption kinetics of MB to FeOOH/RT particles well.

To demonstrate the adsorption of MB molecules via intra-particle diffusion, the surface areas and the pore volumes were monitored by BET analysis (Figure 5-24, Table 5-2). FeOOH/RT particles exhibited the BET surface area of 135.9 m^2/g while FeOOH/HT particles presented the surface area of 27.7 m^2/g. Furthermore, the total pore volumes of FeOOH/RT and FeOOH/HT particles are 0.19 and 0.02 cm^3/g, respectively. The average pore sizes of FeOOH/RT and FeOOH/HT have been found to be large enough to adsorb MB molecules. The formation of Fe_2O_3 during hydrothermal synthesis has decreased the surface areas of FeOOH particles. Compared with FeOOH/HT particles, the larger surface

area and the higher pore volume of FeOOH/RT particles make MB molecules adsorb more effectively.

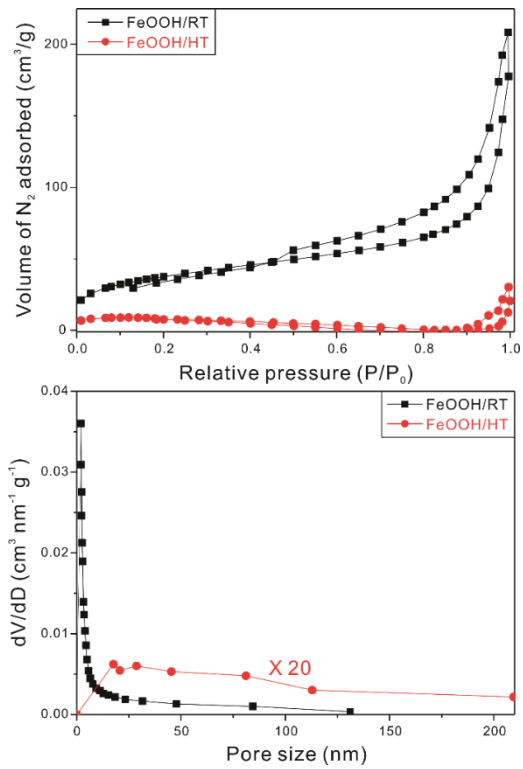

Figure 5-24 N_2 adsorption-desorption isotherms (a) and pore-size distribution profiles (b) of FeOOH/RT (black) and FeOOH/HT (red) particles.

Table 5-2

BET surfaces areas, average pore sizes, and total pore volumes of FeOOH/RT and FeOOH/HT particles.

Sample	BET surface area (m^2/g)	Average pore size (nm)	Total pore volume (cm^3/g)
FeOOH/RT	135.9	12.56	0.19
FeOOH/HT	27.7	67.34	0.02

Based on the above described results, the facile synthesis of a FeOOH-PC membrane, which can separate organic dyes well, is schematically illustrated in Figure 5-25. The reaction between OH^- ions and Fe^{2+} ions forms FeOOH particles in the pores of a PC membrane and the color of the membrane changes from white to brown. All the Fe^{2+} ions are oxidized to Fe^{3+} ions by water-dissolved oxygen molecules. The reaction occurs inside the pores of a PC membrane, leading to the formation of rod shaped FeOOH particles and filling the pores of the membrane (Figure 5-25A). The as-synthesized FeOOH-PC membrane is floated on water and an aqueous solution containing 4NP and MB is dropped slowly on the membrane. While the smaller 4NP molecules diffuse through the FeOOH membrane, the larger MB molecules hardly diffuse through the membrane, leading to the separation of 4NP and MB. After the separation, the membrane is retrieved from the solution simply by using a tweezer. The color of the membrane has been changed from brown to grey due to the color of adsorbed MB molecules. An aqueous H_2O_2 solution is dropped on the membrane and irradiated with a xenon lamp for 5 min. Then, the color of the membrane is recovered to brown as the adsorbed MB molecules are degraded through photo-Fenton reactions. The cleaned membrane can be reused to separate 4NP and MB molecules (Figure 5-25B).

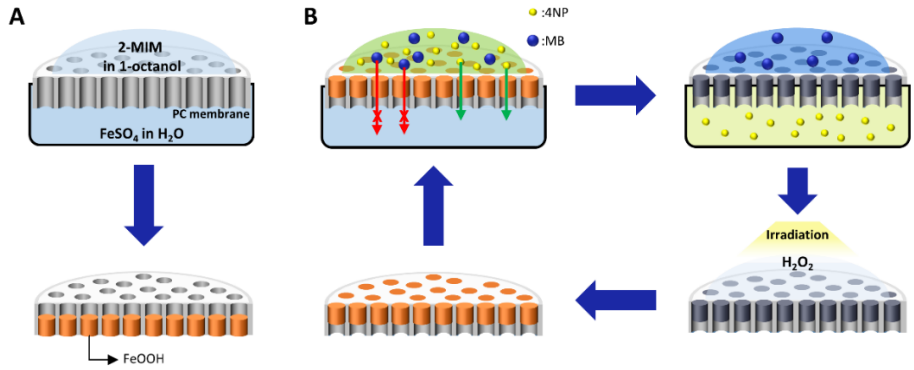

Figure 5-25 Schematics for the interfacial synthesis (A) and the separation and photo-Fenton cleaning (B) of a FeOOH-PC membrane.

5.5. Conclusion

FeOOH-PC membranes have been successfully fabricated via facile interfacial synthesis. FeOOH rods having 200 nm diameters were synthesized within the pores of track-etched PC membranes. The as-synthesized FeOOH-PC membranes could separate organic dyes effectively under ambient conditions via selective diffusion. With bare FeOOH particles obtained by dissolving PC membranes with DMF, the separation mechanism of 4NP/MB has been studied. Although relatively smaller 4NP molecules can diffuse through FeOOH-PC membranes, larger MB molecules, which adsorb to FeOOH particles, cannot diffuse through the membranes, leading to the separation of 4NP and MB molecules. After the separation of 4NP and MB, MB molecules are remained in the FeOOH membranes, leading to the color change of membranes from brown to grey. To reuse a FeOOH-PC

membrane, remaining MB molecules inside the membrane can be degraded via photo-Fenton reactions; the membrane employed for the separation of 4NP/MB was cleaned within 5 min of irradiation. During this cleaning procedure, the FeOOH membrane was also degraded to some extent. Thus, MB molecules can also diffuse slightly through the membrane after some recycling processes. The FeOOH-PC membranes fabricated at room temperature showed higher stability than those fabricated by hydrothermal synthesis, because FeOOH particles were partially transformed into Fe_2O_3 during the hydrothermal synthesis. Overall, the FeOOH-PC membranes, synthesized facilely at room temperature, can be readily employed and reused for the separation of organic molecules.

5.6. Acknowledgement

This work has been financially supported by a research grant of 2020-003228 through the National Research Foundation of Korea.

5.7. References

[1] D. W. Kolpin, D. T. Furlong, M. T. Meyer, E. M. Thurman, S. D. Zaugg, L. B. Barber, H. T. Buxton, *Environ. Sci. Technol.*, **2002**, 36, 1202.

[2] Y. Luo, W. Guo, H. H. Ngo, L. D. Nghiem, F. I. Hai, J. Zhang, S. Liang, X. C. Wang, *Sci. Total Environ.*, **2014**, 473-474, 619.

[3] M. Oveisi, M. A. Asli, N. M. Mahmoodi, *J. Hazard. Mater.*, **2018**, 347, 123.

[4] Z. Zhang, J. Kong, *J. Hazard. Mater.*, **2011**, 193, 325.

[5] F. Han, V. S. R. Kambala, M. Srinivasan, D. Rajarathnam, R. Naidu, *Appl. Catal. A: Gen.*,

2009, 359, 25.

[6] H. Wang, X. Yuan, Y. Wu, G. Zeng, X. Chen, L. Leng, H. Li, *Appl. Catal. B: Environ.*, **2015**, 174-175, 445.

[7] J. Lee, Y. Kim, J. K. Kim, S. Kim, D.-H. Min, D.-J. Jang, *Appl. Catal. B: Environ.*, **2017**, 205, 433-442.

[8] J. Lee, S. Ham, D. Choi, D.-J. Jang, *Nanoscale*, **2018**, 10, 14254.

[9] S. Ham, D. Choi, D.-J. Jang, *Mater. Res. Bull.*, **2019**, 116, 32.

[10] J. Ma, W. Song, C. Chen, W. Ma, J. Zhao, Y. Tang, *Environ. Sci. Technol.*, **2005**, 39, 5810.

[11] X. Shi, A. Tian, J. You, H. Yang, Y. Wang, X. Xue, *J. Hazard. Mater.*, **2018**, 353, 182.

[12] T. T. N. Phan, A. N. Nikoloski, P. A. Bahri, D. Li, *RSC Adv.*, **2018**, 8, 36181.

[13] F. F. Dias, A. A. S. Oliveira, A. P. Arcanjo, F. C. C. Moura, *Appl. Catal. B: Environ.*, **2016**, 186, 136.

[14] L. Zhang, W. Wang, L. Zhou, M. Shang, S. Sun, *Appl. Catal. B: Environ.*, **2009**, 90, 458.

[15] X. Cao, Y. Chen, S. Jiao, Z. Fang, M. Xu, X. Liu, L. Li, G. Pang, S. Feng, *Nanoscale*, **2014**, 6, 12366.

[16] Z. Zhong, W. Li, W. Xing, N. Xu, *Sep. Purif. Technol.*, **2011**, 76, 223.

[17] S. Mondal, M. E. D. A. Reyes, U. Pal, *RSC Adv.*, **2017**, 7, 8633.

[18] T. Liu, L. Wang, X. Lu, J. Fan, X. Cai, B. Gao, R. Miao, J. Wang, Y. Lv, *RSC Adv.*, **2017**, 7, 12292.

[19] J.-R. Li, J. Sculley, H.-C. Zhou, *Chem. Rev.*, **2012**, 112, 869.

[20] R. K. Joshi, P. Carbone, F. C. Wang, V. G. Kravets, Y. Su, I. V. Grigorieva, H. A. Wu, A. K. Geim, R. R. Nair, *Science*, **2014**, 343, 752.

[21] J. R. Werber, C. O. Osuji, M. Elimelech, *Nat. Rev. Mater.*, **2016**, 1, 16018.

[22] H. B. Park, S. H. Han, C. H. Jung, Y. M. Lee, A. J. Hill, *J. Membrane Sci.*, **2010**, 359, 11.

[23] S. Wang, X. Li, H. Wu, Z. Tian, Q. Xin, G. He, D. Peng, S. Chen, Y. Yin, Z. Jiang, M. D. Guiver, *Energy Environ. Sci.*, **2016**, 9, 1863.

[24] J. J. Keating IV, J. Imbrogno, G. Belfort, *ACS Appl. Mater. Interfaces*, **2016**, 8, 28383.

[25] J. Cao, Y. Su, Y. Liu, J. Guan, M. He, R. Zhang, Z. Jiang, *J. Membrane Sci.*, **2018**, 566, 268.

[26] C. Altintas, S. Keskin, *ACS Sustainable Chem. Eng.*, **2019**, 7, 2739.

[27] S. Shahid, K. Nijmerijer, *J. Membrane Sci.*, **2014**, 470, 166.

[28] W. An, P. Swendon, L. Wu, T. Waller, A. Ku, S. M. Kuznicki, *J. Membrane Sci.*, **2011**, 269, 414.

[29] R. Zhou, Q. Zhang, J. Shao, Z. Wang, X. Chen, H. Kita, *Desalination*, **2012**, 291, 41.

[30] E. K. McGuinness, F. Zhang, Y. Ma, R. P. Lively, M. D. Losego, *Chem. Mater.*, **2019**, 21, 5509.

[31] X. B. Ke, H. Y. Zhu, X. P. Gao, J. W. Liu, Z. F. Zheng, *Adv. Mater.*, **2007**, 19, 785.

[32] X. Qian, W. Wu, M. Fang, D. Yue, J. Zeng, Y. Zhao, *Appl. Catal. B: Environ.*, **2018**, 237, 513.

[33] A. Xie, J. Cui, J. Yang, Y. Chen, J. Lang, C. Li, Y. Yan, J. Dai, *Appl. Catal. B: Environ.*, **2020**, 264, 118548.

[34] Q. Wu, H. Yang, L. Kang, Z. Gao, F. Ren, *Appl. Catal. B: Environ.*, **2020**, 263, 118282.

[35] T. Guo, K. Wang, G. Zhang, X. Wu, *Appl. Surf. Sci.*, **2019**, 469, 331.

[36] Q. Sun, M. Liu, K. Li, Y. Zuo, Y. Han, J. Wang, C. Song, G. Zhang, X. Guo, *CrystEngComm*, **2015**, 17, 7160.

[37] A. Xie, J. Cui, J. Yang, Y. Chen, J. Lang, C. Li, Y. Yan, J. Dai, *J. Membrane Sci.*, **2020**, 595, 117499.

[38] R. C. Arbulu, Y.-B. Jiang, E. J. Peterson, Y. Qin, *Angew. Chem. Int. Ed.*, **2018**, 57, 5813.

[39] B. Yu, G. Ye, Z. Zeng, L. Zhang, J. Chen, S. Ma, *J. Mater. Chem. A*, **2018**, 6, 21567.

[40] L. Hao, T. Zheng, J. Jiang, Q. Hu, X. Li, P. Wang, *RSC Adv.*, **2015**, 5, 10723.

[41] H. Fan, X. Huang, K. Kähler, J. Folke, F. Girgsdies, D. Teschner, Y. Ding, K. Hermann, R. Schlögl, E. Frei, *ACS Sustainable Chem. Eng.*, **2017**, 5, 10900.

[42] Z. Li, X. Lai, H. Wang, D. Mao, C. Xing, D. Wang, *Nanotechnology*, **2009**, 20, 245603.

[43] G. Kasparis, A. S. Erdocio, J. M. Tuffnell, N. T. K. Thanh, *CrystEngComm*, **2019**, 21, 1293.

[44] E. R. Encina, M. Distaso, R. N. K. Taylor, W. Peukert, *Cryst. Growth Des.*, **2015**, 15, 194.

[45] X. Liu, G. Qiu, A. Yan, Z. Wang, X. Li, *J. Alloys Compd.*, **2007**, 433, 216.

[46] S. Wu, J. Lu, Z. Ding, N. Li, F. Fu, B. Tang, *RSC Adv.*, **2016**, 6, 82118.

[47] L. Zeng, W. Ren, J. Zheng, A. Wu, P. Cui, *Appl. Surf. Sci.*, **2012**, 258, 2570.

[48] Y. Jia, T. Luo, X.-Y. Yu, Z. Jin, B. Sun, J.-H. Liu, X.-J. Huang, *New J. Chem.*, **2013**, 37, 2551.

[49] S. Majumder, S. Dey, K. Bagani, S. K. Dey, S. Banerjee, S. Kumar, *Dalton Trans.*, **2015**, 44, 7190.

[50] N. Zhou, Q. An, Z. Xiao, S. Zhai, Z. Shi, *RSC Adv.*, **2017**, 7, 45156.

[51] F. Yang, F. Tao, C. Li, L. Gao, P. Yang, *Nat. Commun.*, **2018**, 9, 5443.

Appendices

A.1. List of publications

[1] **Sooho Ham**, Yeonho Kim, Myung Jin Park, Byung Hee Hong, Du-Jeon Jang, Graphene quantum dots-decorated ZnS nanobelts with highly efficient photocatalytic performances, *RSC Advances*, **2016**, 6, 24115-24120.

[2] Jaewon Lee, **Sooho Ham**, Du-Jeon Jang, Facile fabrication of Cu-exchanged ZnS nanoadsorbents for highly efficient removal of contaminants, *Journal of Environmental Chemical Engineering*, **2017**, 5, 4431-4440.

[3] Dayeon Choi, **Sooho Ham**, Du-Jeon Jang, Visible-light photocatalytic reduction of Cr(VI) *via* carbon quantum dots-decorated TiO_2 nanocomposites, *Journal of Environmental Chemical Engineering*, **2018**, 6, 1-8.

[4] **Sooho Ham**, Du-Jeon Jang, Facile photohydroxylation of ZnS nanobelts for enhanced photocatalytic activity, *Journal of Environmental Chemical Engineering*, **2018**, 6, 228-235.

[5] Jaewon Lee, **Sooho Ham**, Dayeon Choi, Du-Jeon Jang, Facile Fabrication of porous ZnS nanostructures with controlled amount of S vacancies for enhanced photocatalytic performances, *Nanoscale*, **2018**, 10, 14254-14263.

[6] **Sooho Ham**, Dayeon Choi, Du-Jeon Jang, Photodeposition of gold nanoparticles on ZnS nanobelts for enhanced dye decomposition, *Materials Research Bulletin*, **2019**, 116, 32-39.

[7] Dayeon Choi, **Sooho Ham**, Du-Jeon Jang, Au-C/SiO_2 nanocomposites with

enhanced peroxidase-like activity for colorimetric and fluorometric detection of hydrogen peroxide, *Materials Research Bulletin*, **2019**, 120, 110578.

[8] Sooho Ham, Dong-Won Jeong, Du-Jeon Jang, Facile fabrication of FeOOH-polycarbonate membranes for effective separation of organic molecules, Submitted to *Separation and Purification Technology*

A.2. List of presentations

A.2.1. International presentations

[1] **Sooho Ham**, Yeonho Kim, Myung Jin Park, Byung Hee Hong, Du-Jeon Jang "Graphene Quantum Dots-Embedded ZnS Nanobelts Having High Photocatalytic Activity" 2016 Materials Research Society Spring Meeting, Phoenix, Arizona, USA (**2016**).

[2] **Sooho Ham**, Du-Jeon Jang "Photohydroxylated ZnS Nanobelts with High Photocatalytic Activity" 17th Asian Chemical Congress & 19th General Assembly of FACS, Melbourne, Victoria, Australia (**2017**).

[3] **Sooho Ham**, Jaewon Lee, Dayeon Choi, Du-Jeon Jang "Photocatalytically Active Porous ZnS Nanostructures with a Controlled Amount of S Vacancies" IUPAC 2019, Paris, France (**2019**).

A.2.2. Domestic presentations

[1] **Sooho Ham**, Yeonho Kim, Du-Jeon Jang "Photo-Deposition of Noble Metals (Au, Pt) on Wurtzite ZnS nanobelts" The 115th National Meeting of the Korean Chemical Society, Goyang, Korea (**2015**).

[2] **Sooho Ham**, Yeonho Kim, Du-Jeon Jang "Fabrication and Photocatalytic Activity of ZnS Nanobelts with Graphene Quantum Dots" The 116th National Meeting of the Korean Chemical Society, Daegu, Korea (**2015**).

[3] **Sooho Ham**, Du-Jeon Jang "Phototreatment of ZnS Nanobelts for Enhanced Photocatalytic Performances" The 117th National Meeting of the Korean Chemical Society, Goyang, Korea (**2016**).

[4] **Sooho Ham**, Du-Jeon Jang "Photohydroxylation of ZnS Nanobelts for Enhanced Photocatalytic Performances" The 119th National Meeting of the Korean Chemical Society, Goyang, Korea (**2017**).

[5] **Sooho Ham**, Du-Jeon Jang "Hydrothermal Fabrication of Porous ZnS Photocatalysts with a Controlled Amount of S Vacancies" The 123rd National Meeting of the Korean Chemical Society, Suwon, Korea (**2019**).

Abstract (Korean)

ZnS 나노구조체의 광촉매 효율을 높이는 연구와 FeOOH 기반의 유기물질 분리막을 합성하는 연구를 진행하였다. ZnS 나노구조체는 광조사에 의해 빠르게 전자와 정공을 들뜨게 할 수 있으며, 들뜬 전자의 에너지 준위가 매우 높기 때문에 광촉매 물질로서 많은 연구가 진행되어왔다. 이러한 장점에도 불구하고, 들뜬 전자와 정공이 빠르게 재결합하며, 자외선 영역의 빛에 대해서만 감응한다는 단점이 존재하였다. 이러한 단점을 해결하여 광촉매 효율을 높이기 위해서 과산화수소를 이용해 황화아연 나노구조체의 표면에 수산화기와 결함을 유도하였다. 또한, 유기물질을 포함하고 있는 ZnS 나노구조체에 추가적으로 수열반응을 진행하여 유기물을 제거함으로써 결함을 유도하였다. 나노 구조체의 표면에 존재하는 결함과 작용기들은 빛에 의해 들뜬 전자와 정공을 분리할 수 있었으며, 이를 통해 광촉매 반응의 효율을 높일 수 있었다. 또한, 광조사에 의해 들뜬 전자를 직접 이용하여 황화아연 나노구조체의 표면에 금 나노입자를 합성하는 연구를 진행하였다. 광조사를 통해 금 나노입자를 합성함으로써, 황화아연과 금 나노입자 사이의 접합계면을 최대화 할 수 있었으며, 이를 통해 들뜬 전자와 정공이 효율적으로 분리되는 것을 밝혔다. 또한 촉매 반응을 통해 재사용이 가능한 FeOOH 기반의 유기 분자 분리막을 합성하는 연구에 대해 기술하였다.

1 장에서는 나노 물질의 기본적인 특성에 대해 설명하였다. 나노 물질은

같은 조성의 벌크 물질과 다른 특성을 나타내고 물질의 크기에 따라 특성이 달라지기 때문에, 그 특성과 특성이 나타나는 원인에 관하여 설명하였다. 또한 나노 물질을 합성하는 다양한 방법과 응용분야에 대해서 기술하였다. 특히, 수처리와 관련된 응용분야에 관해서 자세하게 기술하였다.

2 장에서는 ZnS 나노구조체의 표면에 수산화기를 도입하고 결함을 유도함으로써 광촉매 효율을 증가시키는 연구에 관해 기술하였다. 과산화수소가 빛에 의해 분해될 때 생기는 수산화 라디칼 (·OH)을 이용해 황화아연 나노구조체 표면에 수산화기와 결함을 유도하였다. 황화아연 표면에 존재하는 수산화기와 결함은 빛에 의해 들뜬 전자와 정공의 재결합을 방지하였으며 그 결과 더 효율적으로 라디칼들을 생성할 수 있게 되었다. 최종적으로 4-나이트로페놀의 광촉매 분해 반응에 응용하여 기존의 황화아연 나노구조체보다 높은 분해 효율을 갖는 것을 확인하였다.

3 장에서는 추가적인 수열 반응을 통해 결함을 갖는 ZnS 나노구조체를 합성하고 이를 통해 광촉매 효율을 증가시키는 연구에 대해 기술하였다. Ethylenediamine이 포함된 $ZnS(en)_{0.5}$ 나노구조체를 solvothermal 반응을 통해 합성한 뒤, 추가적인 수열 반응을 통해 ethylenediamine 분자를 제거하였다. 이 과정에서 S vacancy가 유도되었으며 이를 통해 전자와 정공을 분리할 수 있음을 확인하였다. 광학적인 방법을 통해 S vacancy의 함량에 대해 분석하였으며, 전하 분리에 있어 가장 효율적인 구조를

찾음으로써 광촉매 반응의 효율을 증가시킬 수 있었다.

4 장에서는 광증착을 통해 금 나노 입자를 ZnS 나노구조체의 표면에 도입함으로써 광촉매 효율을 증가시키는 연구에 대해 기술하였다. ZnS에 빛에 의해 들뜨는 전자를 이용하여 금 전구체 ($HAuCl_4$)를 직접 환원함으로써 금-ZnS 접합 계면을 최대화 할 수 있었다. ZnS 표면에 합성된 금 나노입자는 넓은 접합 계면으로 인해 낮은 금 함량에서도 효율적으로 ZnS의 전자와 정공을 분리하였으며, 그 결과 황화아연 나노구조체에 비해 높은 광촉매 효율을 나타내는 것을 확인하였다.

5 장에서는 재사용 가능한 FeOOH-폴리카보네이트 분리막을 합성하는 연구에 대해 기술하였다. 계면합성법을 이용하여 폴리카보네이트 막의 기공에 FeOOH를 합성하였으며, 이를 통해 크기가 다른 유기 염료의 분리가 가능함을 밝혔다. 유기 물질의 분리 이후 분리막의 재사용을 위해 photo-Fenton 반응을 이용하여 흡착되어있는 유기 물질을 제거하였으며, 이후 분리막의 재사용이 가능함을 확인하였다.

주요어: 전하 분리, 하이브리드 나노구조체, 광촉매, 반도체 나노물질, 분리막

학번: 2014-22417